

**Some Applications of S-Transform and its Modifications in Signal
and Image Processing**

Thesis

Submitted in partial fulfilment of the requirements for the degree of

DOCTOR OF PHILOSOPHY

by

PRIYA R. KAMATH



DEPARTMENT OF MATHEMATICAL AND COMPUTATIONAL SCIENCES

NATIONAL INSTITUTE OF TECHNOLOGY KARNATAKA,

SURATHKAL, MANGALORE - 575 025

JUNE 2021

Dedicated to

My family

DECLARATION

By the Ph.D. Research Scholar

I hereby declare that the Research Thesis entitled **Some Applications of S-Transform and its Modifications in Signal and Image Processing** which is being submitted to the **National Institute of Technology Karnataka, Surathkal** in partial fulfillment of the requirements for the award of the Degree of **Doctor of Philosophy in Mathematical and Computational Sciences** is a *bonafide report of the research work carried out by me*. The material contained in this Research Thesis has not been submitted to any University or Institution for the award of any degree.

Place: NITK, Surathkal.

Date: 28-06-2021

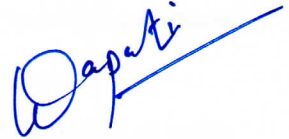

(PRIYA R. KAMATH)

165040 MA16F04

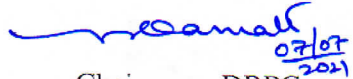
Department of Mathematical and Computational Sciences

CERTIFICATE

This is to *certify* that the Research Thesis entitled **Some Applications of S-Transform and its Modifications in Signal and Image Processing** submitted by Ms. **Priya R. Kamath**, (Register Number: 165040-MA16F04) as the record of the research work carried out by her is *accepted as the Research Thesis submission* in partial fulfillment of the requirements for the award of degree of **Doctor of Philosophy**.



Dr. Kedarnath Senapati
Research Supervisor



Chairman - DRPC

(Signature with Date and Seal)

Chairman
DUGC / DPGC / DRPC
Dept. of Mathematical and Computational Sciences
National Institute of Technology Karnataka, Surathkal
MANGALORE - 575 025

ACKNOWLEDGEMENTS

I am greatly indebted to my guide, Dr. Kedarnath Senapati. He has been my mentor and has encouraged me throughout. He has always kept me motivated, and provided guidance all the time.

I also thank Dr. P. Jidesh, RPAC member, Department of MACS. He has offered his valuable support and guidance and help through discussions while working on SAR images. I would also thank my RPAC member Dr. Debashisha Jena, Department of Electrical and Electronics Engineering, National Institute of Technology Karnataka, Mangalore for his inputs during the progress assessments.

The professors of MACS department have always inspired me. I would like to thank them for offering their guidance and helping me during the entire time.

I would like to also thank my co-scholars and friends who have helped me this entire time for the support and help they have provided while dealing with various aspects of PhD.

I would like to thank my husband Sunil Shenoy and our daughter Diya for providing constant encouragement and support. My parents, brother and in-laws have also been a great help while I was pursuing my PhD.

Place: NITK, Surathkal

Priya R. Kamath

Date: 28-06-2021

ABSTRACT OF THE THESIS

Signal analysis generally involves the usage of time-frequency analysis tools. Fourier transform was able to decompose a periodic signal into multiple sine/cosine signals. This led to the development of many transforms which decomposed the signal using various basis functions. Disadvantages associated with Fourier transform paved the way to introduction of other transforms like short-term Fourier transform. S-transform is a time-frequency analysis tool which has close association with Fourier transform. Unlike the short-term Fourier transform (where the window width was kept constant), the S-transform provided a Gaussian window whose standard deviation was frequency dependent. Thus, the S-transform offered improved frequency resolution at high frequencies and good time resolution at lower frequencies.

The focus of this thesis is on the suitable modification as well as different applications of S-transform. We have applied S-transform and its variations on varieties of one and two-dimensional signals. In addition to proposing a modification of S-transform (which uses a kernel having compact support), we have:

1. Analysed the changes in the phase of an EEG signal, using the conventional S-transform, to identify the eye-blink artifacts. EEG electrodes are used to record signals on the scalp. Due to propagation delay, a phase difference exists between the signal captured by different electrodes. This phase information is used to determine the eye-blink artifacts in the EEG signal .
2. Performed wind speed prediction, using artificial neural network and a modified form of the S-transform (CBST). Experimental results show that this method lowers the prediction errors. To achieve this, we have used CBST to decompose the wind-speed into sub-series. We have performed “one-step-ahead” prediction on the subseries using artificial neural network with backpropagation algorithm. The sub-series predictions are recombined to obtain the wind-speed prediction.
3. Despeckled SAR images using discrete orthonormal S-transform (DOST). We have made use of shock filter, in addition to two-dimensional DOST to remove the speckles in the image. An edge enhancement algorithm is used to enhance the details at the edges. This ensures that the homogenous regions of the SAR image are smooth while retaining the details in the heterogenous regions.

Keywords: S-transforms, time frequency analysis, discrete orthonormal S-transform.

Table of Contents

Abstract of the Thesis	i
List of Figures	vii
List of Tables	xi
Acronyms	xiii
Notations	xv
1 INTRODUCTION	1
1.1 FOURIER TRANSFORM	1
1.2 HARTLEY TRANSFORM	4
1.3 SHORT-TIME FOURIER TRANSFORM AND GABOR TRANSFORM	6
1.4 WAVELET TRANSFORM	6
1.5 S-TRANSFORM	8
1.5.1 The relationship between S-transform and Fourier transform . .	11
1.5.2 The relationship between S-transform and wavelet transform .	11
1.5.3 Properties of S-transform	12
1.6 DISCRETE S-TRANSFORM	12
1.7 RESEARCH GAP	13
1.8 RESEARCH MOTIVATION AND OBJECTIVES	13
1.9 THESIS ORGANIZATION AND CONTRIBUTION	14
2 MODIFICATIONS OF S-TRANSFORM	15
2.1 Modified S-Transforms	15
2.1.1 Variation 1 : Asymmetric window for hyperbolic ST	16
2.1.2 Modified <i>ST</i> based on standard deviation of the Gaussian window	21

2.2	MODIFIED <i>ST</i> BASED ON COMPACT SUPPORT KERNEL	28
2.2.1	Variation 5: Modified <i>ST</i> with compactly supported kernel (CSKST)	28
2.2.2	Proposed <i>ST</i> using a modified kernel	31
2.2.3	Numerical comparison of proposed CBST with conventional ST and CSKST	33
2.3	DISCRETE ORTHONORMAL STOCKWELL TRANSFORM	35
2.4	TWO DIMENSIONAL DOST	36
2.4.1	2D-DOST patterns for some binary images	36
2.5	CONCLUSION	37
3	DETECTION OF OCULAR ARTEFACT IN EEG SIGNAL USING S- TRANSFORM	39
3.1	ANALYSIS OF EEG SIGNAL USING CROSS-ST	41
3.2	RESULTS AND DISCUSSION	43
3.3	CONCLUSION	43
4	SHORT-TERM WIND SPEED FORECASTING USING S-TRANSFORM WITH COMPACTLY SUPPORTED KERNEL AND ARTIFICIAL NEU- RAL NETWORK	47
4.1	PADDING AND SIGNAL DECOMPOSITION USING CBST	49
4.2	FORECASTING USING ANN	52
4.3	EXPERIMENTAL RESULTS	54
4.3.1	Parameters for evaluation	55
4.3.2	Case 1: Prediction using simulation data	55
4.3.3	Case 2: Wind speed recorded at 100m height	57
4.3.4	Case 3: Coastal wind speed forecasting	58
4.4	CONCLUSION	61
5	DESPECKLING OF SAR IMAGES USING SHOCK FILTERS AND TWO DIMENSIONAL DISCRETE ORTHOGONAL S-TRANSFORM	63
5.1	INTRODUCTION TO SAR IMAGE DESPECKLING	63
5.1.1	Shock Filter	66

5.2	SAR IMAGE DESPECKLING USING 2D-DOST	66
5.3	EDGE ENHANCEMENT USING RATIO BASED EDGE DETECTION	70
5.4	EXPERIMENTS AND RESULTS	73
5.4.1	CPU Execution Time	85
5.5	CONCLUSION	85
6	CONCLUSION	87
	BIBLIOGRAPHY	89
	PUBLICATIONS	98

List of Figures

1.1	A signal with increasing frequency	2
1.2	Amplitude spectra of signals shown in Figures 1.1	3
1.3	Phase spectra of signals shown in Figures 1.1	4
1.4	Hartley transform of signals shown in Figures 1.1	5
1.5	STFT of signals shown in Figure 1.1	7
1.6	Gabor Transform of signals shown in Figure 1.1	8
1.7	Variation of the Gaussian window with frequency	9
1.8	S-transform of signals shown in Figure 1.1	10
2.1	Signals used to evaluate the different versions of ST	17
2.2	The time-frequency plot of signals using conventional ST	18
2.3	Variation of the asymmetric window with frequency	19
2.4	The time-frequency plot of the signals using hyperbolic ST	20
2.5	The time-frequency plot, using WWOST of the signals	22
2.6	The time-frequency plot of the signals transformed using MST	24
2.7	The time-frequency plot of the signals transformed using (Moukadem et al., 2015)	27
2.8	The time-frequency plot of signals transformed using (Zidelmal et al., 2017)	30
2.9	Variation of CB kernel	31
2.10	Variation of the proposed window with frequency	32
2.11	The time-frequency plot of the signals transformed using CBST	34
2.12	2D - DOST of the image with a white dot with black background	37
2.13	Some simple images and their DOST	38

3.1	The 10-20 electrode placement system to record EEG (Rojas et al., 2018)	40
3.2	EEG signal at electrodes (a) FP1 (b) F3 (c) F7 using average montage	44
3.3	S-transform of EEG signal at electrodes	45
3.4	Phase synchrony between the signals at electrodes	46
3.5	Signal at FP1 and the detected ocular artefact zone	46
4.1	Wind speed decomposed into sub-series	49
4.2	Effect of padding	51
4.3	ANN structure	52
4.4	Block diagram depicting short-term wind speed forecasting	54
4.5	Case 1: Hourly wind speed data forecasting	56
4.6	Case 2: Hourly wind speed data forecasting	57
4.7	Effect of increasing frequency bands on prediction error	59
4.8	Case 3: Hourly wind speed data forecasting	60
4.9	Case 3: Hourly wind speed LiDAR data forecasting	62
5.1	Edge directions used for edge detection. Each cell in the 3×3 direction mask consists of a binary value represented here as white (0) and black (1)	71
5.2	(a) Zoomed-in view of SAR Image shown in Figure 5.4(a), (b) Ratio based image R' obtained by applying the method specified in Section 5.3 on image shown in (a).	72
5.3	(a) A "noise-free" image of airport (b) image corrupted by multiplicative gamma distributed noise and (c) despeckled image using the proposed scheme. Image courtesy: USC-SIPI Image Database	75
5.4	Despeckled images of SAR image using various algorithms (Sentinel-1)	78
5.5	Zoomed-in view of Figure 5.4	79
5.6	Despeckled images of SAR image using various algorithms (NASA/JPL-Caltech)	80
5.7	Zoomed-in view of Figure 5.6	81

5.8	Despeckled images of SAR image using various algorithms (TerraSAR-X)	83
5.9	Zoomed-in view of Figure 5.8	84

List of Tables

1.1	Thesis contribution	14
2.1	Renyi entropy of variations of ST having compact support using the test signals	35
4.1	CASE 1: Short-term wind-speed prediction	56
4.2	CASE 2: Short-term wind-speed prediction	58
4.3	CASE 3: Short-term wind-speed prediction	61
4.4	CASE 3: Short-term wind-speed prediction of LiDAR data	61
5.1	PSNR and SSIM obtained after using various despeckling methods on SAR image shown in Figure 5.3(b)	74
5.2	Quantitative Measures for the evaluation of SAR images shown in Figures (5.4,5.6 and 5.8)	77
5.3	Execution time of SAR images shown in Figure (5.4,5.6 and 5.8) respectively	85

ACRONYMS

Some of the important acronyms are used in this thesis are mentioned here.

ST :	S-Transform
FT :	Fourier transform
STFT :	Short-term Fourier Transform
WT :	Wavelet transform
DST :	Discrete S-Transform
DOST :	Discrete Orthonormal S-Transform
CB:	Cheriet-Belouchrani
EEG:	electroencephalogram
ARMA:	Autoregressive moving average
ANN:	Artificial neural networks
SSA:	Singular spectrum analysis
MODWT:	Maximal overlap discrete wavelet transform
EMD :	Empirical mode decomposition
EEMD :	Ensemble EMD
CEEMDAN:	Complete EEMD with adaptive noise
IMF:	Intrinsic mode functions
SVM:	Support Vector Machine
SAR:	Synthetic aperture radar
IDOST:	Inverse DOST
ENL:	Equivalent number of looks
EPI:	Edge preservation index
TCR:	Target to clutter reatio
ERI:	Expectation of ratio image

NOTATIONS

Some of the important nomenclature that have been used throughout the thesis is listed below.

t :	time
f :	frequency
$x(t)$:	signal
$X(f)$:	FT of $x(t)$
$w(t)$:	window function
X_{STFT} :	STFT of $x(t)$
$W(\tau, \lambda)$:	WT of $x(t)$ at τ time sample and scale λ
ψ :	Mother wavelet function
$X_S(\tau, f)$:	S-transform of $x(t)$ with at τ
v :	voice in DOST
β :	frequency bandwidth
σ :	standard deviation of a Gaussian kernel
R_X^α :	Renyi entropy of the transformed signal X
$CrossST(t, f)$:	Cross-ST of two signals
$w[n]$:	wind-speed time series
\tilde{w} :	wind-speed after padding $w[n]$
\tilde{w}_s :	s^{th} subseries of \tilde{w}
\hat{w}_s :	predicted s^{th} wind-speed subseries
\hat{w}_s :	predicted wind-speed subseries
x, y :	pixel location (in Chapter 5)
M, N :	size of the SAR image
v_x, v_y :	voice image pair
I :	SAR image
T :	Threshold

CHAPTER 1

INTRODUCTION

Many real world signals are non stationary and vary in frequency with time. Time-frequency analysis is required to understand how the frequency and thereby the energy is distributed in time (Boashash, 2015). Fourier transform gives the information on the distribution of energy with frequency. However, this information may be insufficient due to lack of time stamps, where the energy is concentrated. In many cases, these time stamps are important as they indicate the occurrence of an event. This led to the introduction of a two-dimensional (time-frequency) space for analysis of the signal.

1.1 FOURIER TRANSFORM

Fourier transform (FT) gives the phase and amplitude spectral information of a signal in frequency domain. As the FT is unitary, one can reconstruct the original signal by defining an inverse FT if both the frequency and phase information are known.

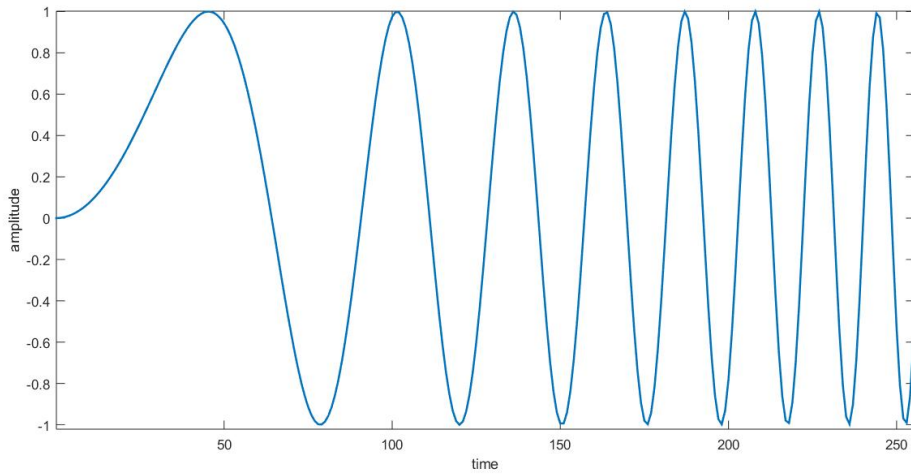
The FT of a signal $x(t)$ for a frequency f and time t is defined by

$$X(f) = \int_{-\infty}^{\infty} x(t)e^{-i2\pi ft} dt \quad (1.1.1)$$

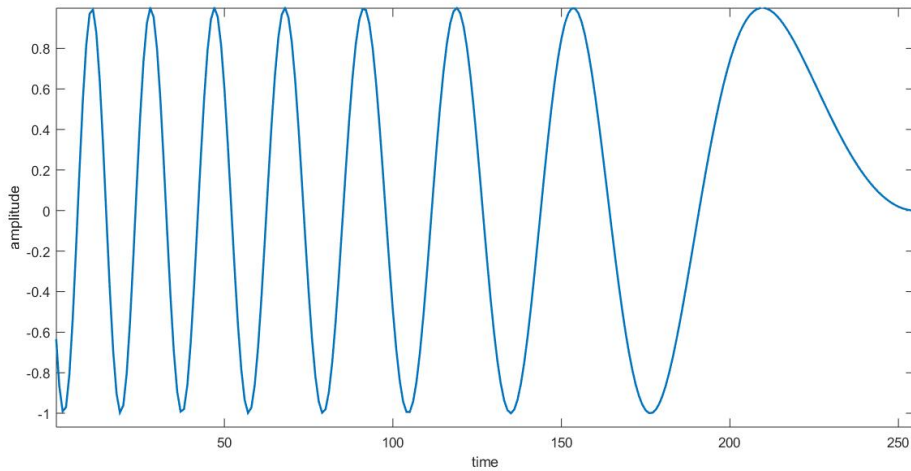
and the inverse Fourier transform of $x(t)$ is defined by

$$x(t) = \int_{-\infty}^{\infty} X(f)e^{i2\pi ft} df \quad (1.1.2)$$

While the FT provides information about the frequency content of the signal, its use is limited to stationary signal only. In case of real-world signals, which are normally non-stationary in nature, the FT is not a good tool for analysis. This can be demonstrated by considering the following two signals with different underlying physics. Both the signals have sinusoidal waveforms; for one, the instantaneous frequency increases linearly, as defined in Eq. 1.1, whereas for the other, it decreases over time. Both the



(a)



(b)

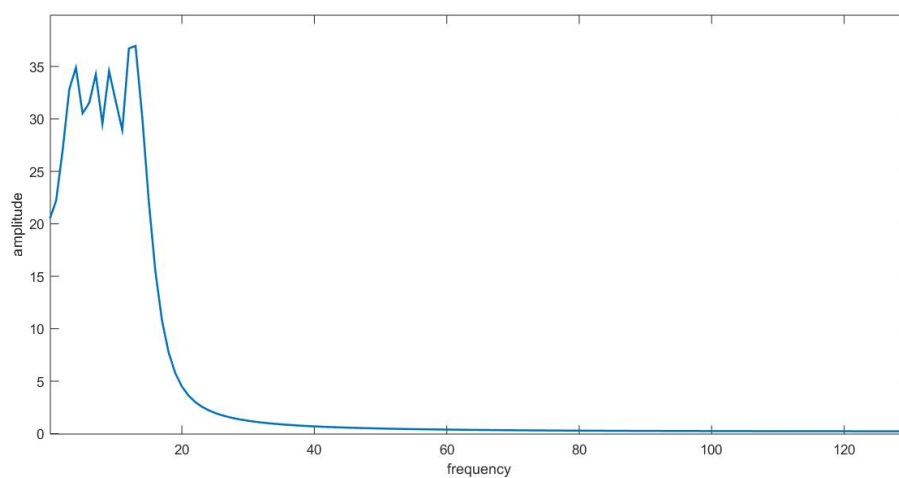
Figure 1.1 (a) A 256 point time series with increasing frequency defined by $\sin(\frac{2\pi t^2}{256})$ (b) signal similar to (a) but with decreasing frequency.

signals are plotted in Figure 1.1.

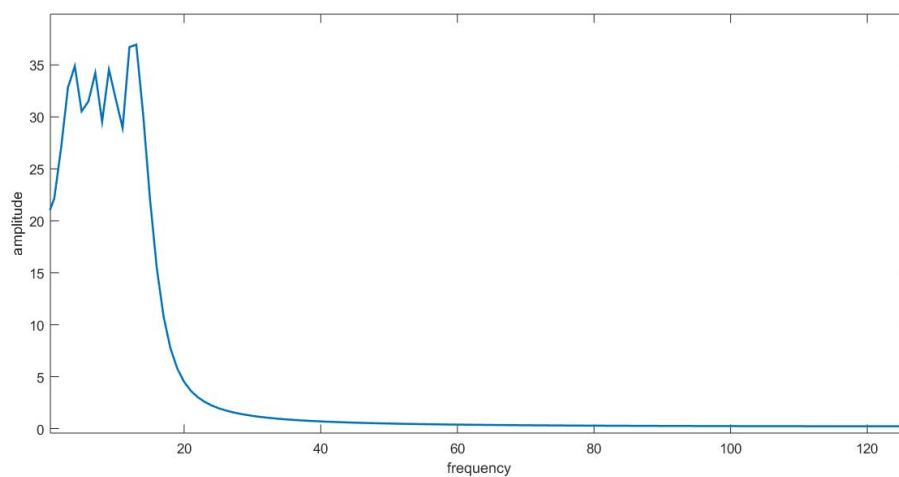
$$x(t) = \sin\left(\frac{2\pi t^2}{256}\right) \quad (1.1.3)$$

The amplitude and phase spectra of these two different signals are shown in Figures 1.2 and 1.3 respectively. We observe that the two very different signals have same amplitude spectra, but different phase-spectra. Therefore, the phase is one of the important factors which is capable of exhibiting hidden information about the signal. The problem of having similar amplitude spectra for two different signals can be solved using the

Hartley transform which is discussed briefly below. In addition to this, the information about time of occurrence of various frequencies is not available in the Fourier spectra. The Short-time Fourier transform manages to address these issues up to certain extent.

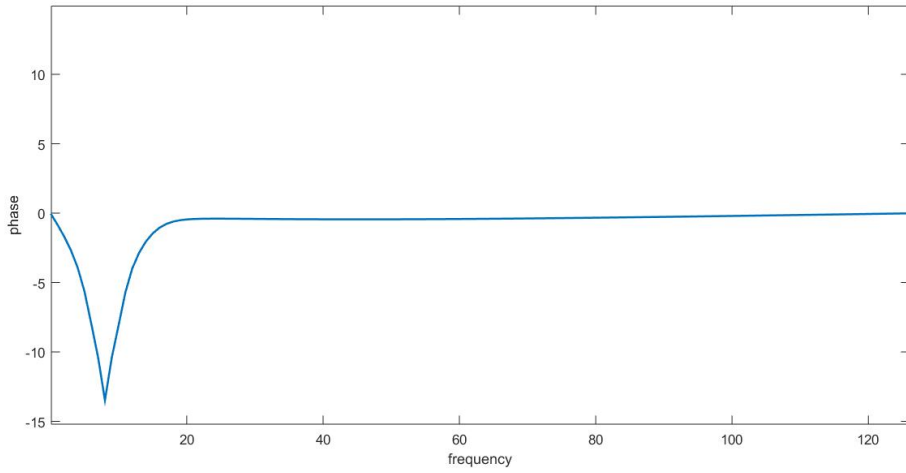


(a)

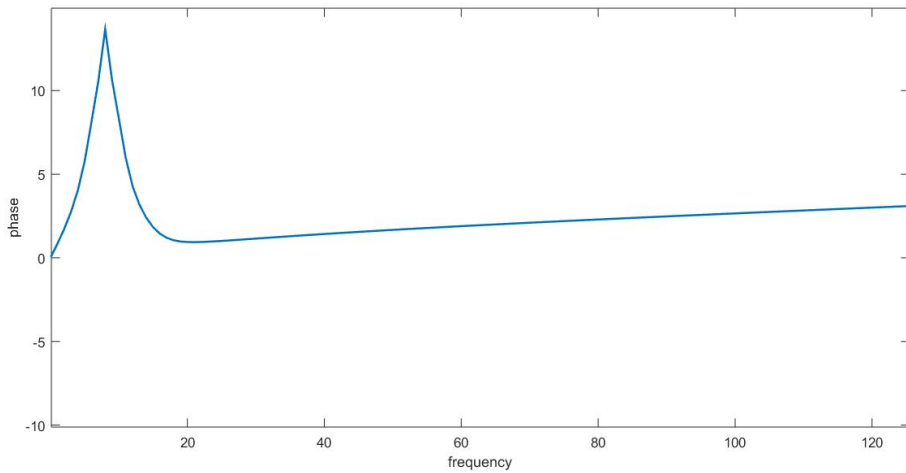


(b)

Figure 1.2 Amplitude spectra of signals shown in Figures 1.1(a) and (b) respectively



(a)



(b)

Figure 1.3 Phase spectra of signals shown in Figure 1.1 (a), and Figure 1.1 (b) [top to bottom]

1.2 HARTLEY TRANSFORM

Hartley transform is very closely associated with the Fourier transform which is defined as follows:

$$H(f) = \int_{-\infty}^{\infty} x(t) \text{cas}(2\pi ft) dt \quad (1.2.1)$$

where,

$$\text{cas}(2\pi ft) = \cos(2\pi ft) + \sin(2\pi ft) \quad (1.2.2)$$

Unlike the Fourier transform where the transformed coefficients are complex valued, the Hartley transform has only real-valued coefficients. Thus, the signals shown in the Figure 1.1 can be distinguished easily without referring to its phase.

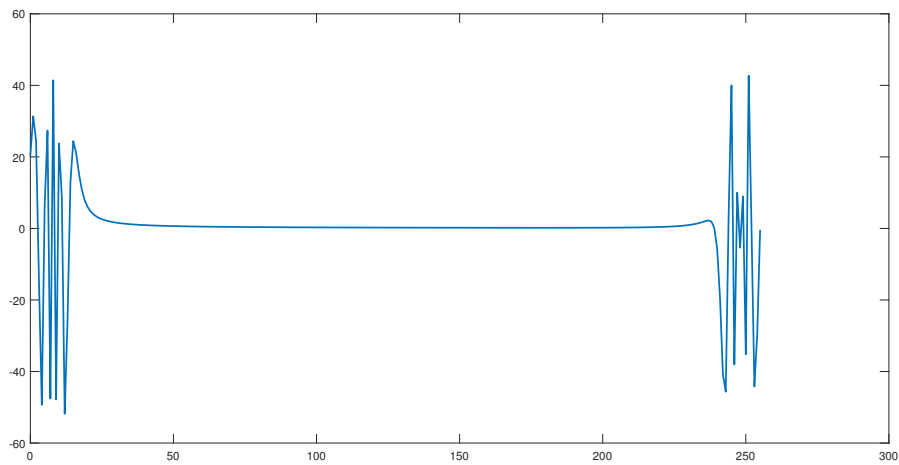
The inverse Hartley transform is given by :

$$x(t) = \int_{-\infty}^{\infty} H(f) \text{cas}(2\pi ft) dt \quad (1.2.3)$$

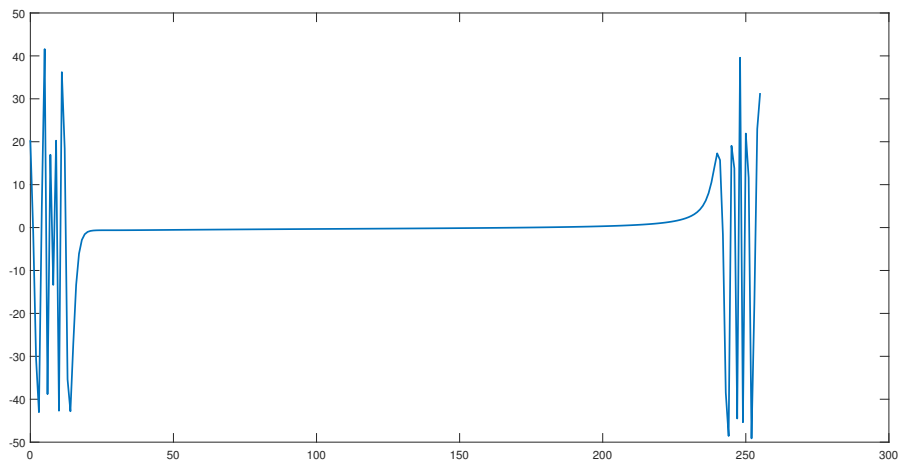
Hartley transform $H(f)$ can be written using FT $X(f)$, of the signal $x(t)$ as:

$$H(f) = R\{X(f)\} - I\{X(f)\} \quad (1.2.4)$$

where $R\{\cdot\}$ and $I\{\cdot\}$ represent the real and imaginary components, respectively.



(a)



(b)

Figure 1.4 Hartley transform of the signals shown in Figure 1.1(a), and in Figure 1.1(b) [top to bottom]. It can be observed that the Hartley spectra is different for both the signals, which is desirable.

1.3 SHORT-TIME FOURIER TRANSFORM AND GABOR TRANSFORM

In order to circumvent the inherent disadvantages of FT, short-time Fourier transform (STFT) was used. It can be defined as:

$$X_{STFT}(\tau, f) = \int_{-\infty}^{\infty} x(t)w(t - \tau)e^{-i2\pi ft} dt \quad (1.3.1)$$

where X_{STFT} is the STFT of the signal $x(t)$ and $w(t - \tau)$ is the window of fixed width shifted by time $t = \tau$.

A sliding window of fixed width was introduced in STFT to obtain the time information on the frequency content of the signal. For demonstration, STFT of the signals shown in Figure 1.1 is shown in Figure 1.5. A rectangular sliding window of size 32 is used with a hop size of 1.

Gabor transform is a modification of STFT where Gaussian window is considered. For a signal $x(t)$, its Gabor transform $X_G(\tau, f)$ is defined as:

$$X_G(\tau, f) = \int_{-\infty}^{\infty} x(t)e^{-\pi(t-\tau)^2} e^{-i2\pi ft} dt \quad (1.3.2)$$

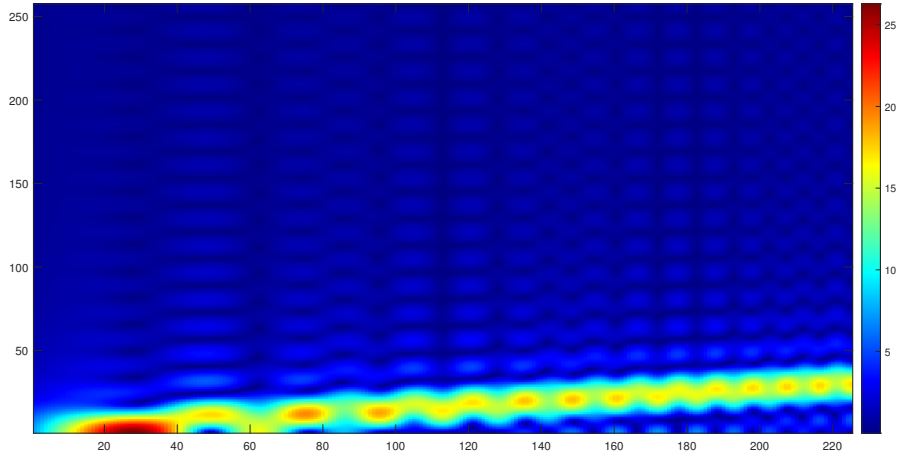
The Gabor transform of the signals associated to Eq. 1.1 is shown in Figure 1.6.

The size of the window in both STFT and Gabor transform is fixed. This fixes the time and frequency resolution. But in many applications, it is necessary to have different resolutions at different frequencies. When a signal has high frequencies, a good time resolution is required, whereas a good frequency resolution is needed when the signal contains low frequencies. Wavelet transform was able to address this as it provided multi-resolution structure. We will also see later that in S-transform (ST), the window width varies according to the frequency and thereby provides multi-resolution structure.

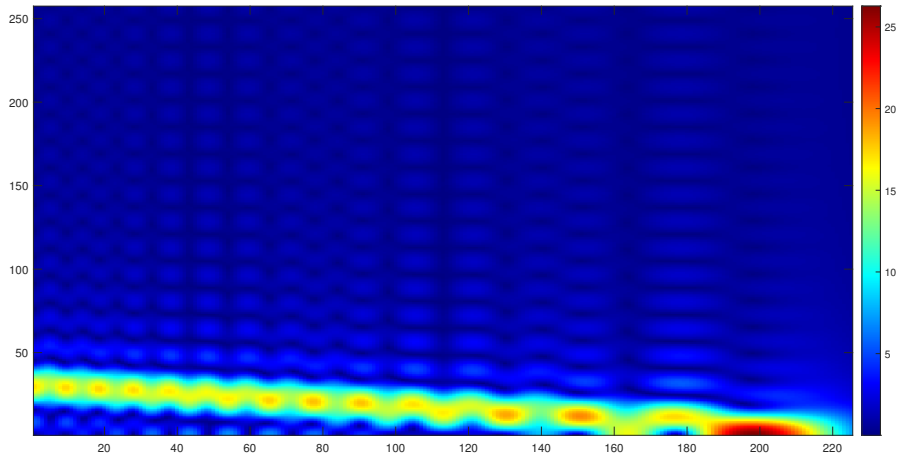
1.4 WAVELET TRANSFORM

Continuous Wavelet Transform of $x(t) \in L^2(\mathbb{R})$, the space of square integrable functions in \mathbb{R} , with delay τ and scale λ , can be defined as (Ventosa et al., 2008).

$$W(\tau, \lambda) = \int_{-\infty}^{\infty} x(t)\psi_{\tau, \lambda}^*(t)dt \quad (1.4.1)$$



(a)



(b)

Figure 1.5 STFT of signals shown in Figure 1.1

where ψ^* is the complex conjugate of the mother wavelet function ψ defined as

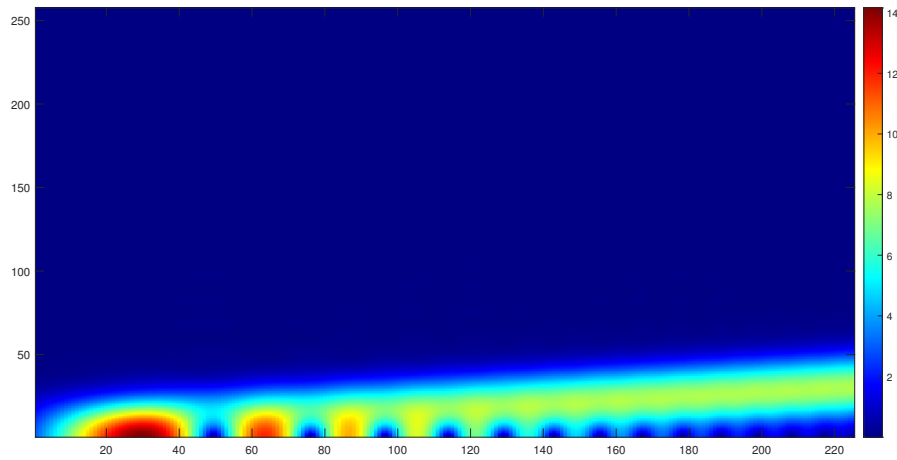
$$\psi_{\tau,\lambda}(t) = \frac{1}{\sqrt{|\lambda|}} \psi\left(\frac{t-\tau}{\lambda}\right) \quad (1.4.2)$$

The reconstruction formula of the wavelet transform is given by

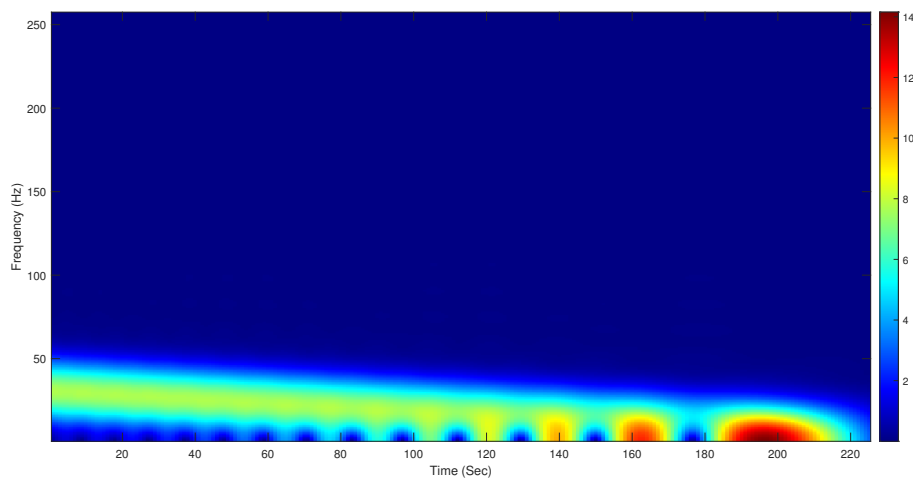
$$x(t) = \frac{1}{C_\psi} \int_{-\infty}^{\infty} \int_{-\infty}^{\infty} W(\tau, \lambda) \frac{1}{\sqrt{\lambda}} \psi\left(\frac{t-\tau}{\lambda}\right) \frac{d\lambda dt}{\lambda^2} \quad (1.4.3)$$

where

$$C_\psi = \int_{-\infty}^{\infty} \frac{|\hat{\psi}(w)|^2}{|w|} dw < \infty \quad (1.4.4)$$



(a)



(b)

Figure 1.6 Gabor Transform of signals shown in Figure 1.1

Wavelet transforms (WT) are extremely popular and are used in many applications. They address the multiresolution issue, present in STFT, by varying the scale of wavelets. However, they do not have any direct relationship with Fourier transform.

The next section discusses in detail about ST. It has a direct relation with the Fourier transform and can also address multi-resolution.

1.5 S-TRANSFORM

ST was proposed by Stockwell et al. (1996). It can be a useful tool to analyse the time-frequency of a signal. This transform has the phase information referenced at the

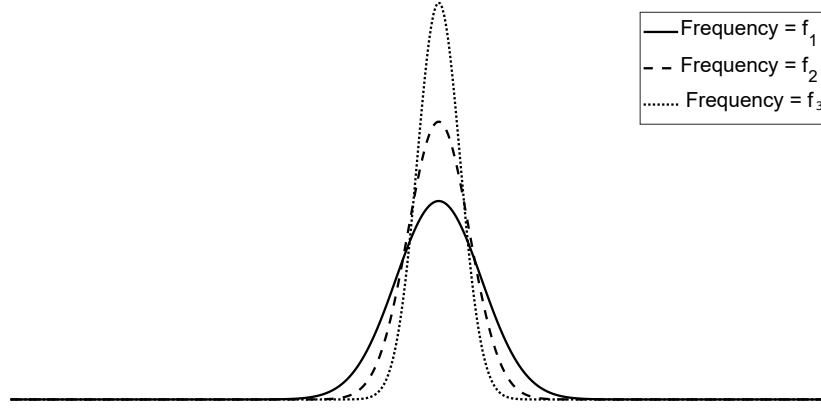


Figure 1.7 Variation of the Gaussian window with frequencies f_1 , f_2 , and f_3 where $f_1 < f_2 < f_3$

time $t = 0$. This absolutely referenced phase enables analysis of the signal using the phase information present in it. In addition, ST can be used to derive the instantaneous frequency of the signal. The S-transform of a continuous signal $x(t)$ is defined as (Stockwell et al., 1996).

$$X_S(\tau, f) = \int_{-\infty}^{\infty} x(t)w(t - \tau)e^{-i2\pi ft} dt \quad (1.5.1)$$

The window function $w(t)$ should satisfy the following condition:

$$\int_{-\infty}^{\infty} w(\tau, f)d\tau = 1 \quad (1.5.2)$$

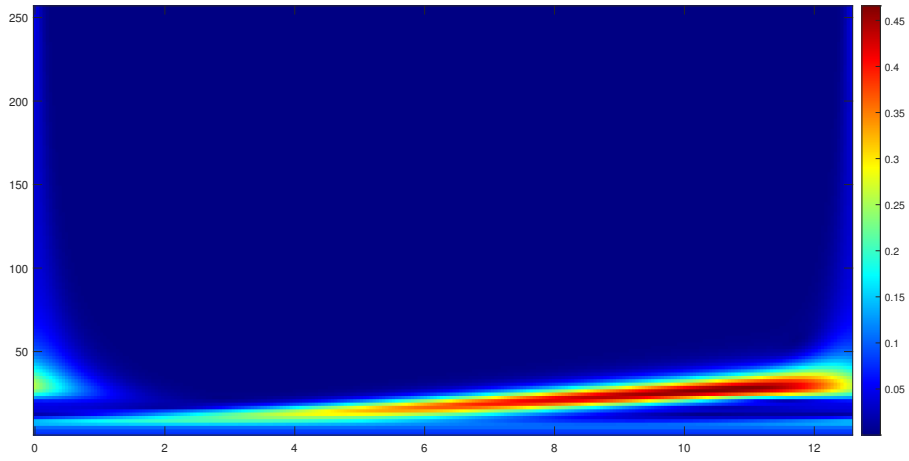
Rewriting (1.5.1) using a Gaussian window:

$$w(t) = \frac{|f|}{\sqrt{2\pi}}e^{-\frac{f^2(t-\tau)^2}{2}} \quad (1.5.3)$$

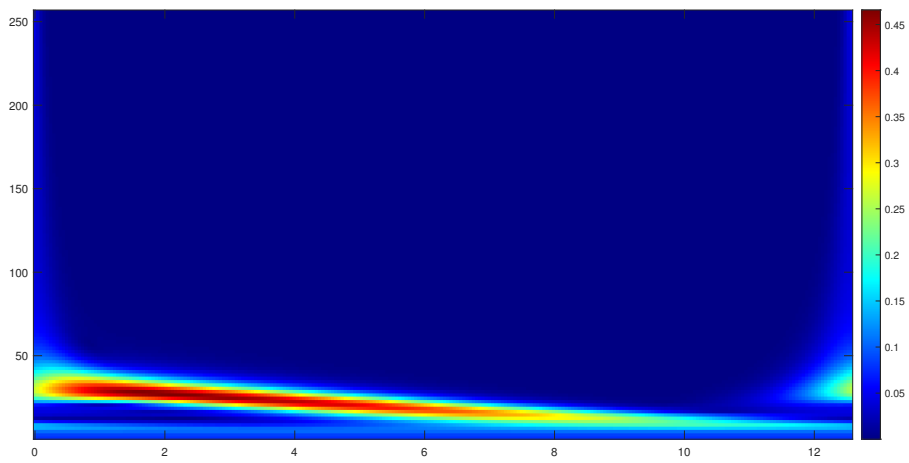
we get

$$X_S(\tau, f) = \int_{-\infty}^{\infty} x(t) \left[\frac{|f|}{\sqrt{2\pi}}e^{-\frac{f^2(t-\tau)^2}{2}} \right] e^{-i2\pi ft} dt \quad (1.5.4)$$

The integrand inside the square bracket of the Eq. (1.5.4) is a translated version of standard Gaussian with frequency dependent standard deviation, and $e^{-i2\pi ft}$ is a phase correcting factor. This frequency dependent Gaussian window is shown in Figure 1.7.



(a)



(b)

Figure 1.8 S-transform of signals shown in Figure 1.1

1.5.1 The relationship between S-transform and Fourier transform

Unlike the wavelet transform, the S-transform has a direct relation with Fourier transform. The FT $X(f)$ of the signal $x(t)$ can be obtained by summing the ST $X_S(t, f)$ over τ as follows

$$X(f) = \int_{-\infty}^{\infty} X_S(\tau, f) d\tau \quad (1.5.5)$$

Eq.(1.5.5) can also be expressed using Eq.(1.5.4) as follows

$$X(f) = \int_{-\infty}^{\infty} \int_{-\infty}^{\infty} x(t) \frac{|f|}{\sqrt{2\pi}} e^{-\frac{f^2(t-\tau)^2}{2}} e^{-i2\pi ft} dt d\tau \quad (1.5.6)$$

The original signal can be recovered from $X(f)$ using inverse Fourier transform as follows:

$$x(t) = \int_{-\infty}^{\infty} X(f) e^{i2\pi ft} df \quad (1.5.7)$$

The above equation can also be written as

$$x(t) = \int_{-\infty}^{\infty} \left\{ \int_{-\infty}^{\infty} X_S(\tau, f) d\tau \right\} e^{i2\pi ft} df \quad (1.5.8)$$

Eq. (1.5.8) can be viewed as an inverse S-transform through the inverse Fourier transform.

1.5.2 The relationship between S-transform and wavelet transform

ST is a hybrid version of WT and FT, as it uses a translated and scalable Gaussian window function to obtain time-frequency resolution. Also, ST is very similar to wavelet transform with Morlet type wavelets with some phase and amplitude adjustments (Gibson et al., 2006). Fourier transform of a signal can be obtained by summing ST over time. Thus, unlike wavelet transforms, the ST has a direct relation with the Fourier transform.

A detailed study on the the relationship between ST and wavelet transforms can be found in (Ventosa et al., 2008). The ST can be defined by using WT as follows:

$$X_S(\tau, \lambda) = C_{ws}(\tau, \lambda) W(\tau, \lambda) \quad (1.5.9)$$

where,

$$C_{ws}(\tau, \lambda) = \frac{e^{-i2\pi k\tau/\lambda}}{\sqrt{|\lambda|} |I_\psi|} \quad (1.5.10)$$

and

$$I_{\Psi} = \int_{-\infty}^{\infty} \Psi(t) e^{i2\pi ft} dt \quad (1.5.11)$$

The scaling factor λ in WT and frequency f in ST are related as $\lambda = k/f$ where k is a constant.

1.5.3 Properties of S-transform

A detailed study on ST was also performed by Ranjan et al. (2018). Some of the important properties are briefly defined below.

1. Linearity

$$S\{ax(t) + by(t)\} = aS_X(\tau, f) + bS_Y(\tau, f) \quad (1.5.12)$$

2. Scaling

$$S\{x(at)\} = S_X(a\tau, \frac{f}{a}) \quad (1.5.13)$$

3. Time Shifting

$$S\{x(t-a)\} = S_X(\tau-a, f) e^{-j2\pi fa} \quad (1.5.14)$$

4. Time-reversal

$$S\{x(-t)\} = S_X^*(-\tau, f) \quad (1.5.15)$$

5. Convolution

$$S\left\{\int_{-\infty}^{\infty} x(t-a)y(a)da\right\} = \int_{-\infty}^{\infty} S_X(\tau-a, f)y(a)e^{-j2\pi fa}da \quad (1.5.16)$$

Here, $S\{\cdot\}$ denotes the ST operator, $S_X(\tau, f)$ and $S_Y(\tau, f)$ are ST of the signals $x(t)$ and $y(t)$, respectively.

1.6 DISCRETE S-TRANSFORM

For discrete time signals $x(kt)$ with N samples, the discrete Fourier transform is given as:

$$X\left[\frac{n}{NT}\right] = \sum_{k=0}^{N-1} x[kT] e^{-\frac{j2\pi nk}{N}} \quad (1.6.1)$$

The corresponding discrete S-transform is defined in Eq. (1.6.2) and (1.6.3) for $n = 1, 2, \dots, N$ and $n = 0$, respectively (Stockwell et al., 1996)

$$X_S \left[jT, \frac{n}{NT} \right] = \sum_{m=0}^{N-1} X \left[\frac{m+n}{NT} \right] e^{-\frac{2\pi^2 m^2}{n^2}} e^{\frac{i2\pi m j}{N}} \quad (1.6.2)$$

$$X_S[jT, 0] = \frac{1}{N} \sum_{m=0}^{N-1} x \left[\frac{m}{NT} \right] \quad (1.6.3)$$

where $j, m, n = 0, 1, 2, \dots, N-1$.

The discrete inverse S-transform is given by

$$x[kt] = \sum_{n=0}^{N-1} \left\{ \frac{1}{N} \sum_{j=0}^{N-1} X_S \left[jT, \frac{n}{NT} \right] \right\} e^{\frac{i2\pi nk}{N}} \quad (1.6.4)$$

1.7 RESEARCH GAP

Numerous research have been carried out in the field of signal and image processing using mutli-resolution time-frequency analysis. More specifically, the usage of wavelet transform has been explored in many applications. While a close association of S-transform with Fourier transform opens a wide opportunity of research, we observe that the research on applications of S-transform is stil developing. ST also has a high computation cost, and complex valued highly redundant transform coefficients.

1.8 RESEARCH MOTIVATION AND OBJECTIVES

While a lot of research has been done using ST, we believe that, application of ST is still in nascent stages. This motivated us to carry out this work. Since its onset, many reserachers have attempted to modify ST to improve time-frequency resolution. We wanted to explore some of these variations and apply them to process signals and images. The main research objectives in this thesis are:

- To find suitable modifications in ST kernel, possibly, a compactly supported kernel.
- Exploring the phase spectrum of ST and apply in signals for better analysis.
- To find applications of ST in signals and images.

1.9 THESIS ORGANIZATION AND CONTRIBUTION

This thesis is divided primarily into six chapters. In Chapter 1, we discussed different types of time-frequency analysis tools and their relation with ST. We have briefly discussed about FT, STFT, Gabor transform and wavelet transform. We have also given an introduction to ST. In Chapter 2, we discuss different modifications of ST. Most of the modifications are done by varying the associated kernel. An asymmetric bi-Gaussian kernel was introduced by Pinnegar and Mansinha (2003a). Some Gaussian kernels whose standard deviation varied using a function of frequency is also discussed here. Finally, kernels based on compact support is discussed. We propose a ST with compactly supported Cheriet-Belouchrani kernel (CBST). We also introduce the discrete orthonormal ST in this chapter.

The Chapters 3 – 5 contain the main work of the thesis, where the focus in these chapters is on the various applications which are based on ST. In Chapter 3, we have made use of the phase information present in the ST to identify the artifacts due to eye blink in an EEG signal. Propagation delay between two adjacent electrodes placed near the eye is used to determine the eye blink in a EEG signal. In Chapter 4, we make use of the proposed CBST to predict short-term wind speed. For this, the wind speed data is divided into multiple sub-series using the proposed CBST. This is followed by an hour ahead prediction using artificial neural networks. In Chapter 5 we employ DOST to despeckle SAR images. A Butterworth filter is used to decompose the SAR image into high and low frequency components. The low frequency components are treated using shock filter, whereas DOST is applied on higher frequency components to remove speckles.

Table 1.1 Thesis contribution

Chapter	ST variation	Application
3	Conventional ST	Ocular artifact detection in EEG
4	CBST (proposed in Chapter 2)	Wind speed prediction
5	2D-DOST	Despeckle SAR images

Chapter 6 contains a conclusion of the thesis. We also discuss the scope of the work that will be carried out in the future.

CHAPTER 2

MODIFICATIONS OF S-TRANSFORM

2.1 Modified S-Transforms

There are many modifications of ST which can be found in literature. A few of the important modifications are discussed below. These modified transforms aim to find a kernel for improving the time-frequency (TF) representation of the non-stationary time series.

Most of the modified window functions satisfy the following condition:

$$\int_{-\infty}^{\infty} w(\tau, f) d\tau = 1 \quad (2.1.1)$$

Eq. (2.1.1) ensures that when ST is integrated over time, it results in Fourier transform of the original signal which is given in Eq. 1.5.5. Thus, the signal can be perfectly reconstructed from its ST.

We propose a modified kernel of ST with compact support. To evaluate the performance, in terms of frequency resolution, with different modifications of ST along with the proposed one, we consider the following four signals:

1. The first signal under consideration consists of single frequency, given by:

$$x_1(t) = \sin(10\pi t) \quad (2.1.2)$$

2. The frequency content of the second signal considered, varies sinusoidally. Using such a signal, we wanted to observe the behaviour of various modified ST when the frequency periodically changes over time:

$$x_2(t) = \cos(100\pi t - 20\pi t^2) + \cos(4\pi \sin(5\pi t) + 80\pi t) \quad (2.1.3)$$

3. Thirdly, the next signal contains a frequency component which increases linearly

and another decreases logarithmically over time:

$$x_3(t) = \cos(20\pi \log(25t + 1)) + \cos(50\pi t + 100\pi t^2) \quad (2.1.4)$$

4. By considering the signal given below, we will observe the behaviour of modified STs at low as well as high frequencies.

$$x_4(t) = \cos(132\pi t + 14\pi t^2) + \cos(10\pi t - 2\pi t^2) + \cos(30\pi t + 6\pi t^2) \quad (2.1.5)$$

The signals and their STs are shown in Figures 2.1 and 2.2 respectively.

2.1.1 Variation 1 : Asymmetric window for hyperbolic ST

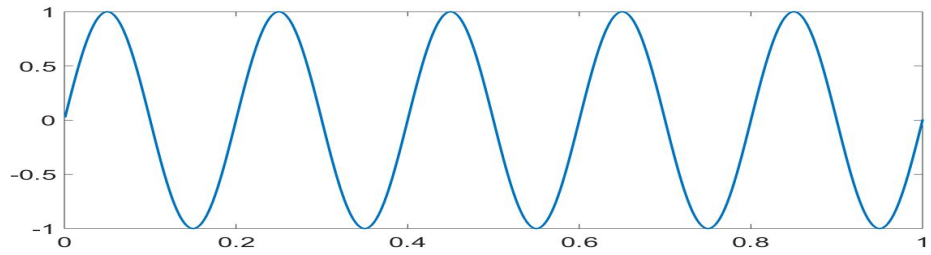
Pinnegar and Mansinha (2003b) presented a generalized ST in which the shape of the window function is asymmetric. They have shown that the conventional ST exhibits low frequency resolution at the onset of events. To overcome this problem, they have introduced an asymmetric window which is tapered in the front and back directions. The window function has frequency dependent asymmetry. If the window is symmetric, a better frequency resolution is provided. At high frequencies, when the time resolution is good, symmetric window is used to improve the frequency resolution. At low frequencies, the asymmetry of the window is increased to improve the time resolution. Using a hyperbolic function, they have constructed the asymmetric window w_{HY} which is more wide at low frequencies.

$$w_{HY}(\tau - t, f) = \frac{2|f|}{\sqrt{2\pi}(\gamma_{HY}^F + \gamma_{HY}^B)} e^{-\frac{f^2[X(\tau-t, \gamma_{HY}^B, \gamma_{HY}^F, \lambda_{HY}^2)]^2}{2}} \quad (2.1.6)$$

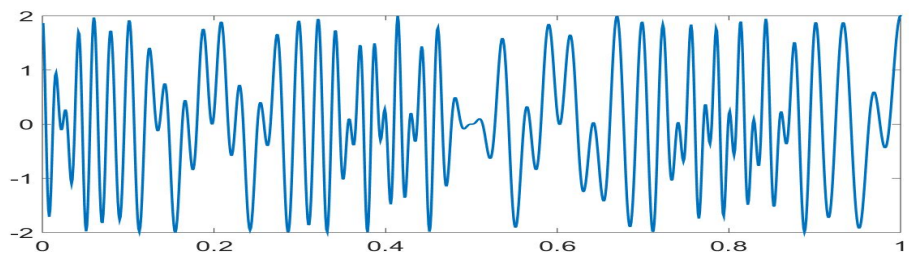
where

$$\begin{aligned} X(\tau - t, \gamma_{HY}^B, \gamma_{HY}^F, \lambda_{HY}^2) \\ = \left(\frac{\gamma_{HY}^B + \gamma_{HY}^F}{2\gamma_{HY}^B \gamma_{HY}^F} \right) (\tau - t - \zeta) + \left(\frac{\gamma_{HY}^B - \gamma_{HY}^F}{2\gamma_{HY}^B \gamma_{HY}^F} \right) \sqrt{(\tau - t - \zeta)^2 + \lambda_{HY}^2} \end{aligned} \quad (2.1.7)$$

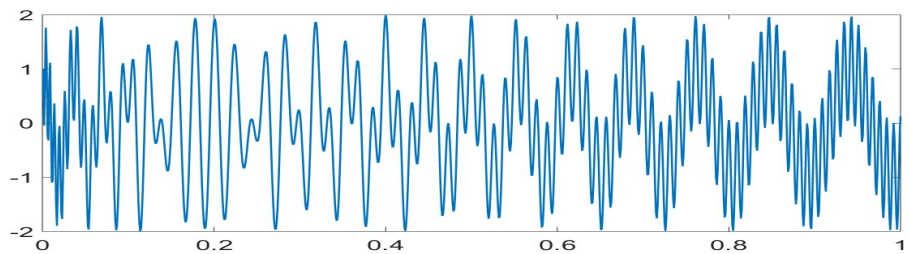
In Eq. (2.1.7), X is a hyperbola in $(\tau - t)$. γ_{HY}^B and γ_{HY}^F are the backward and forward taper parameter, respectively. λ_{HY} is a positive curvature parameter. Translation



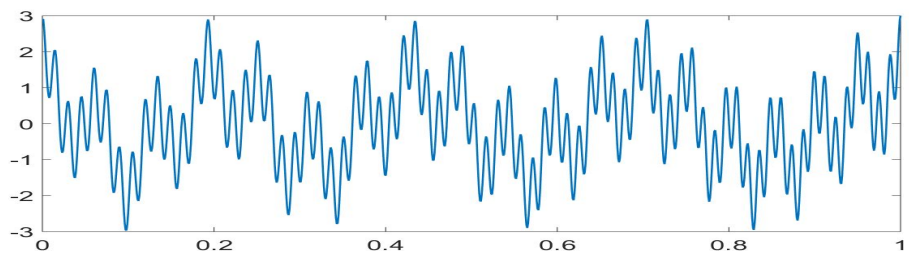
(a)



(b)



(c)



(d)

Figure 2.1 Signals used to evaluate the different versions of ST (a) $x_1(t)$ (b) $x_2(t)$ (c) $x_3(t)$ (d) $x_4(t)$

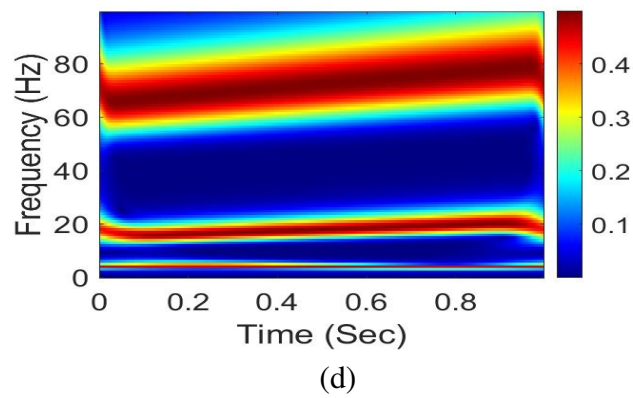
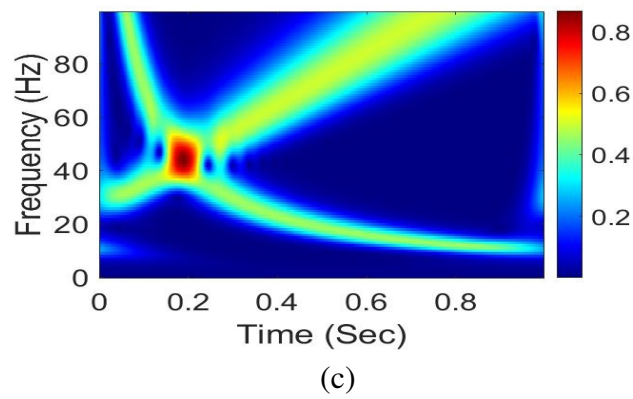
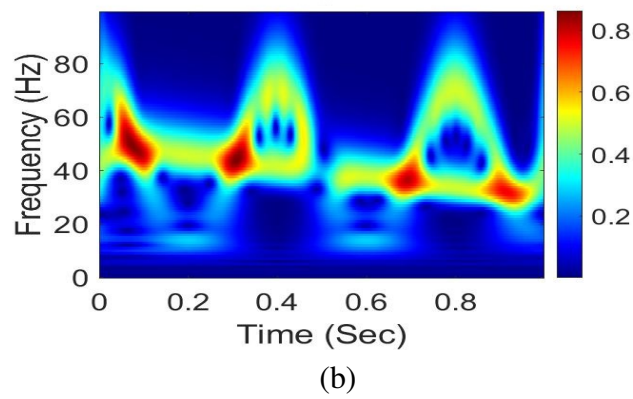
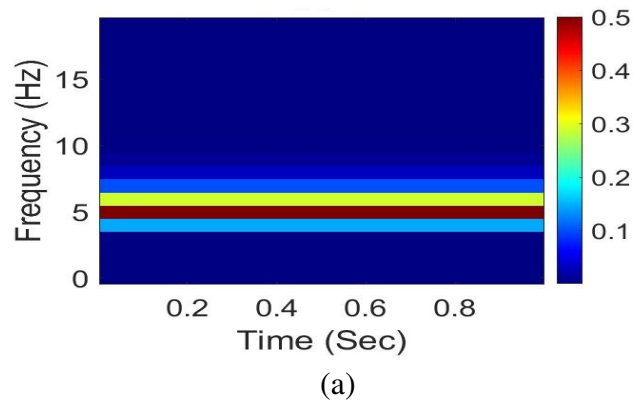


Figure 2.2 The time-frequency plot of signals using conventional ST (a) $x_1(t)$ (b) $x_2(t)$ (c) $x_3(t)$ (d) $x_4(t)$

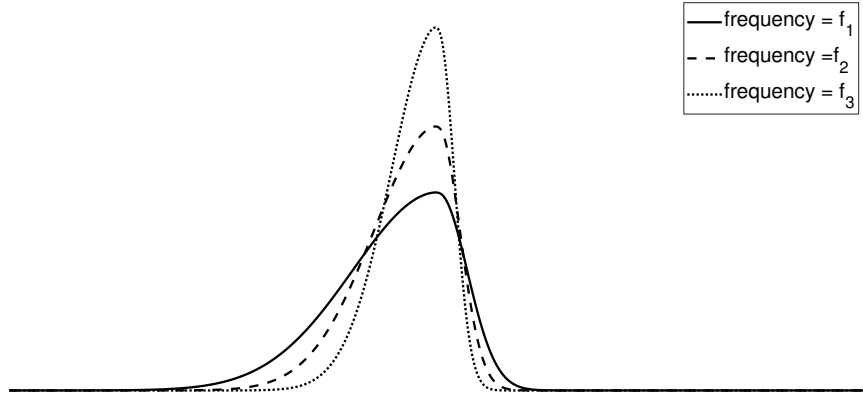


Figure 2.3 Variation of the asymmetric window with frequencies $f_1 < f_2 < f_3$

parameter ζ ensures that the peak of w_{HY} occurs at $(\tau - t) = 0$ and it is defined by

$$\zeta = \sqrt{\frac{(\gamma_{HY}^B - \gamma_{HY}^F)^2 \lambda_{HY}^2}{4\gamma_{HY}^B \gamma_{HY}^F}} \quad (2.1.8)$$

The hyperbolic ST is then expressed as follows

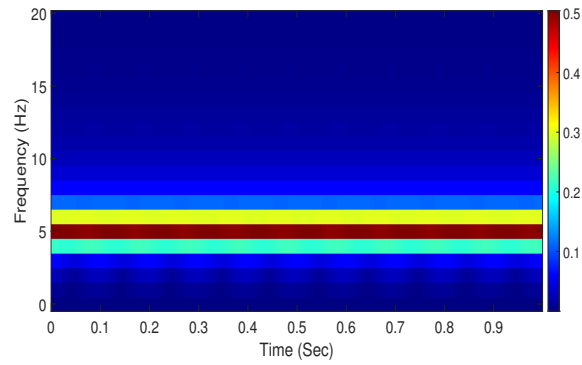
$$X_S(t, f) = \int_{-\infty}^{\infty} x(\tau) w_{HY}(\tau - t, f) e^{-i2\pi f t} d\tau \quad (2.1.9)$$

Figure 2.3 shows variation in the shape of asymmetric kernel suggested by Pinnegar and Mansinha (2003b). Figure 2.4 shows the results of the hyperbolic ST .

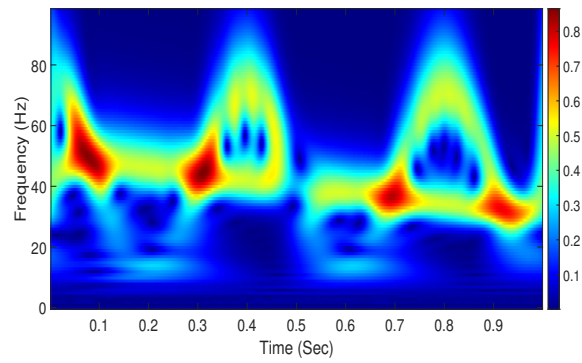
2.1.1.1 Observations

The following observations have been made on comparing the TF representation shown in Figure 2.4 with the one shown in Figure 2.2

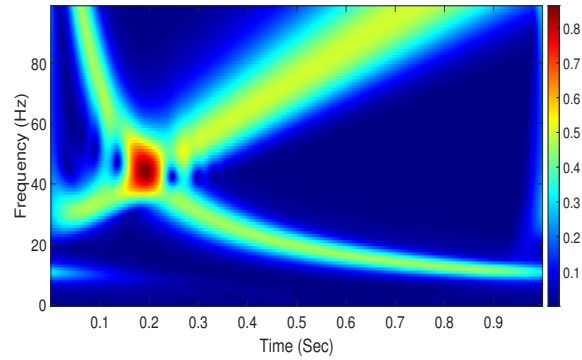
1. At lower frequencies, the TF resolution is extremely good in hyperbolic ST . However, the resolution deteriorates at higher frequencies.
2. The TF resolution is poor when the frequency is changing periodically as seen in case of signal $x_2(t)$. Also, some unwanted frequency components seem to have appeared.



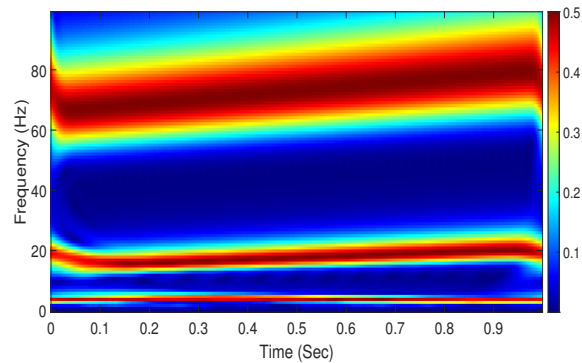
(a)



(b)



(c)



(d)

Figure 2.4 The time-frequency plot, using hyperbolic ST of the signals (a) $x_1(t)$ (b) $x_2(t)$ (c) $x_3(t)$ (d) $x_4(t)$

2.1.2 Modified ST based on standard deviation of the Gaussian window

In the ST , originally proposed by Stockwell et al. (1996), the standard deviation is a function of frequency as shown in equation below:

$$\sigma(f) = \frac{1}{|f|} \quad (2.1.10)$$

Many researchers have worked on modifying the standard deviation of the Gaussian window. Sejdic et al. (2008), Assous and Elkington (2012), George (2009), Moukadem et al. (2015) have varied the width of the Gaussian window by using a frequency dependent standard deviation. These variations are discussed below.

2.1.2.1 Variation 2 :Window Width Optimized S-Transform

Sejdic et al. (2008) have modified the window of ST to increase the energy concentration in the time-frequency domain. This method is named as "Window Width Optimized S-Transform" (WWOST). The standard deviation σ of the window is modified as shown in the following equation:

$$\sigma(f) = \frac{1}{|f|^p} \quad (2.1.11)$$

WWOST is then expressed as follows

$$X_S(t, f) = \int_{-\infty}^{\infty} x(\tau) \frac{|f|^p}{\sqrt{2\pi}} e^{-\frac{f^{2p}(t-\tau)^2}{2}} e^{-i2\pi ft} d\tau \quad (2.1.12)$$

The parameter p controls the window width and the optimal value of p is determined by evaluating the concentration measure $CM(p)$ which is defined as

$$CM(p) = \frac{1}{\int_{-\infty}^{\infty} \int_{-\infty}^{\infty} |S_x^p(t, f)| dt df} \quad (2.1.13)$$

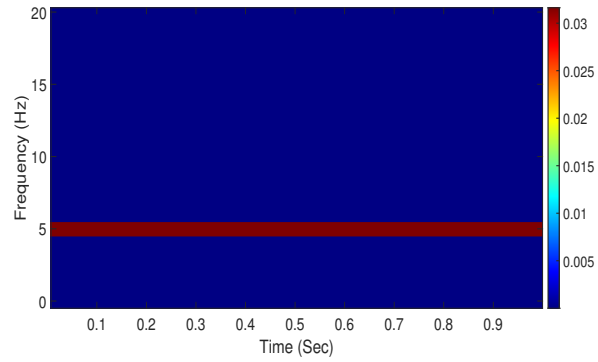
where,

$$S_x^p(t, f) = \frac{S_x(t, f)}{\sqrt{\int_{-\infty}^{\infty} \int_{-\infty}^{\infty} |S_x^p(t, f)|^2 dt df}} \quad (2.1.14)$$

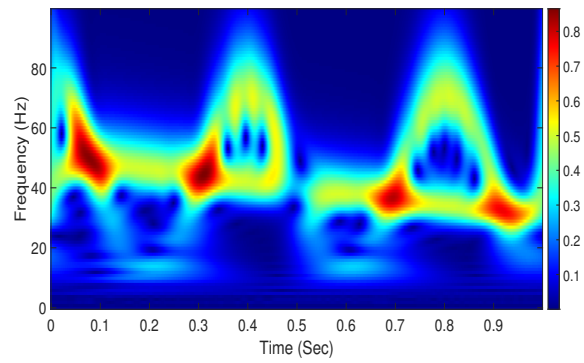
and

$$p_{opt} = \max_p [CM(p)] \quad (2.1.15)$$

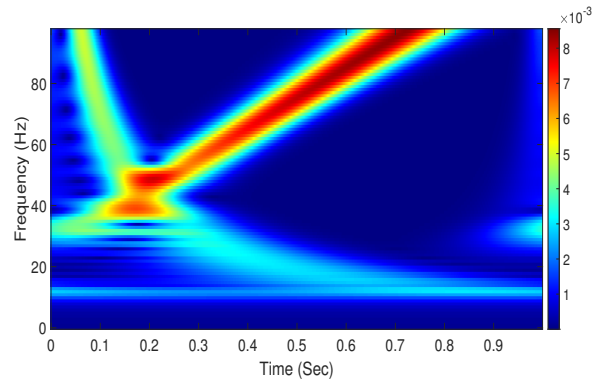
Figure 2.5 shows results of WWOST shown in Eq. (2.1.12)



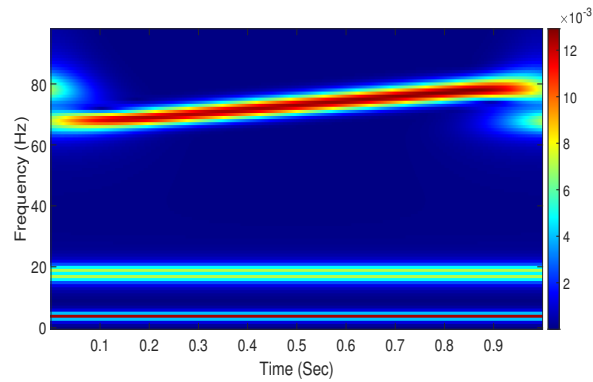
(a)



(b)



(c)



(d)

Figure 2.5 The time-frequency plot, using WWOST of the signals (a) $x_1(t)$ (b) $x_2(t)$ (c) $x_3(t)$ (d) $x_4(t)$

2.1.2.2 Observations

The following observations have been made on comparing the time-frequency representation shown in Figure 2.5 to the one shown in Figure 2.2

1. The TF resolution is comparatively good since the concentration measure is calculated to determine the WWOST parameters. This is more apparent in case of TF representation of the signal $x_4(t)$ in Figure 2.5(d).
2. The TF resolution is not very impressive in low frequency band when the frequency is changing periodically as seen in case of signal $x_2(t)$ whose WWOST is shown in Figure 2.5(b). Also some unwanted frequencies seem to have appeared.
3. As seen in Figures 2.5(b) and 2.5(c), TF representation of signals $x_2(t)$ and $x_3(t)$, is not very good at the borders of signal.

2.1.2.3 Variation 3 :Another modification of ST (MST) by (George et al., 2009; Assous and Boashash, 2012)

A scaling parameter $\gamma(f)$ as defined by the Eq. 2.1.17 is introduced by George et al. (2009); Assous and Boashash (2012). This scaling parameter is used to modify the frequency dependent standard deviation $\sigma(f)$ as indicated in Eq. (2.1.16)

$$\sigma(f) = \frac{\gamma(f)}{|f|} \quad (2.1.16)$$

where,

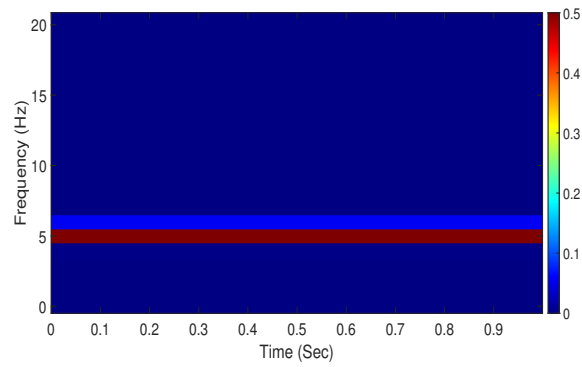
$$\gamma(f) = \alpha f + \beta \quad (2.1.17)$$

Thus the MST is defined as follows

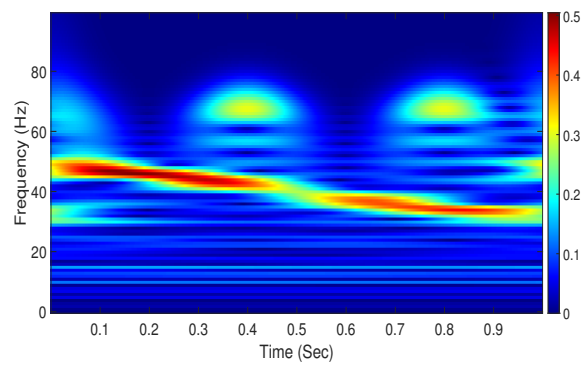
$$X_S(t, f) = \int_{-\infty}^{\infty} x(\tau) \frac{|f|}{(\alpha f + \beta)\sqrt{2\pi}} e^{\frac{-f^2(t-\tau)^2}{2(\alpha f + \beta)^2}} e^{-i2\pi f t} d\tau \quad (2.1.18)$$

By modifying the ST in this manner, the authors have achieved data dependent progressive improved resolution. George et al. (2009) have determined the typical range for α and β to be 0.25 – 0.5 and 0.5 – 3, respectively by trial and error in their experiments. Whereas, Assous and Boashash (2012) found that the suitable values of α and β to be equal to four times the variance ($4\sigma^2$) and $\frac{1}{N}$, respectively, to evaluate the phase correlation between the spatially separated signals. Here N is the length of signal considered.

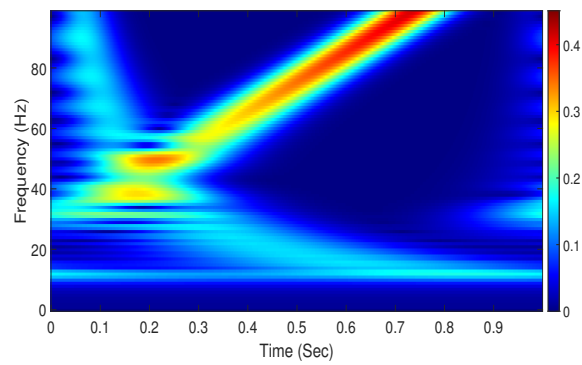
Figure 2.6 shows the results of MST.



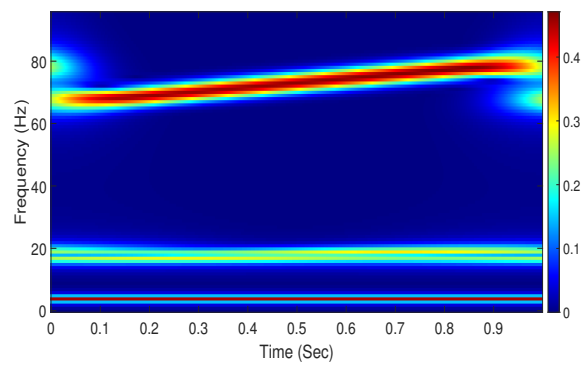
(a)



(b)



(c)



(d)

Figure 2.6 The time-frequency plot, using MST of the signals (a) $x_1(t)$ (b) $x_2(t)$ (c) $x_3(t)$ (d) $x_4(t)$

2.1.2.4 Observations

The following observations have been made on comparing the time-frequency representation shown in Figure 2.6 to the one shown in Figure 2.2

1. The TF resolution is comparatively good at all frequencies, when there is low variation in frequency. In Figures 2.6(a) and 2.6(d) the frequency varies slowly with time and hence a better TF resolution is obtained.
2. The time-frequency resolution is poor when the frequency is changing rapidly over time as seen in case of signal $x_2(t)$ and $x_3(t)$ in Figures 2.6(b) and 2.6(c). In particular, it is not able to capture the sinusoidal shape of the frequency variation in Figure 2.6(b). Also the logarithmic frequency component in Figure 2.6(c) cannot be clearly recognised.
3. Also, from Figures 2.6(c) and 2.6(d), we observe that, some unwanted frequency components seem to have appeared especially at the onset and during the end of signal.

2.1.2.5 Variation 4 : Optimized ST proposed by Moukadem et al. (2015)

Moukadem et al. (2015) have extended the works by Sejdic et al. (2008) and Assous and Boashash (2012) to develop a more generic version of ST . The authors have optimized the energy concentration in time-frequency plane, in addition to adding several other parameters to obtain a better time-frequency resolution in transformed domain. Here the $\gamma(f)$ is modified as follows

$$\gamma(f) = (mf^p + k)f^{(1-r)} \quad (2.1.19)$$

Thus the ST is modified as

$$X_S(t, f) = \int_{-\infty}^{\infty} x(\tau) \frac{|f|^r}{(mf^p + k)\sqrt{2\pi}} e^{\frac{-f^{2r}(t-\tau)^2}{2((mf^p+k)^2)}} e^{-i2\pi f t} d\tau \quad (2.1.20)$$

While the parameter values in case of George et al. (2009); Assous and Boashash (2012) have been determined empirically, Moukadem et al. (2015) have determined the parameters using an optimization technique. For this, energy concentration measure similar to the one used in Sejdic et al. (2008) is implemented. The energy concentration

measure is defined as follows:

$$CM(m, p, k, r) = \frac{1}{\int_{-\infty}^{\infty} \int_{-\infty}^{\infty} \overline{S_x^{m,p,k,r}(t, f)} |dt df} \quad (2.1.21)$$

where

$$\overline{S_x^{m,p,k,r}(t, f)} = \frac{S_x^{m,p,k,r}(t, f)}{\sqrt{\int_{-\infty}^{\infty} \int_{-\infty}^{\infty} |S_x^{m,p,k,r}(t, f)|^2 dt df}} \quad (2.1.22)$$

The optimization problem can be written as

$$\arg \max_{m,p,k,r} \left(\frac{1}{\sqrt{\int_{-\infty}^{\infty} \int_{-\infty}^{\infty} |S_x^{m,p,k,r}(t, f)| dt df}} \right)$$

subject to:

$$\begin{aligned} nT_s f_{max}^r - k - m &\leq 0 \\ m f_{max}^p + k - lT_s &\leq 0 \\ 0 &\leq m, p, k, r \leq 3 \end{aligned} \quad (2.1.23)$$

Here, the values of n and l are determined empirically to 10 and 1000, respectively. The parameter T_s is the sampling interval of the signal with maximum frequency f_{max}

2.1.2.6 Observations

The following observations have been made on comparing the time-frequency representation shown in Figure 2.7 to the one shown in figure 2.2

1. A good resolution of time and frequency is achieved at all frequencies for MST.
2. Unlike in previous case, the TF resolution is good when the frequency is changing periodically as seen in case of signal $x_2(t)$ in Figure 2.7(b) .
3. Also some unwanted frequencies are introduced especially at the onset and during the end of signal. This can be clearly seen in Figures 2.7(c) and 2.7(d)
4. From Figure 2.7(a), it is also observed that the TF resolution for a signal with constant frequency is not as good as the one observed in Figure 2.5(a)

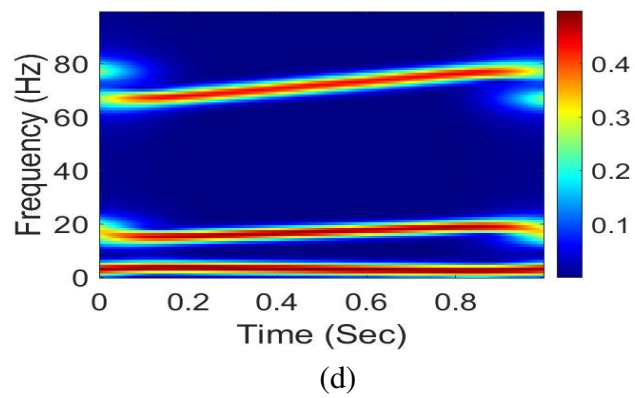
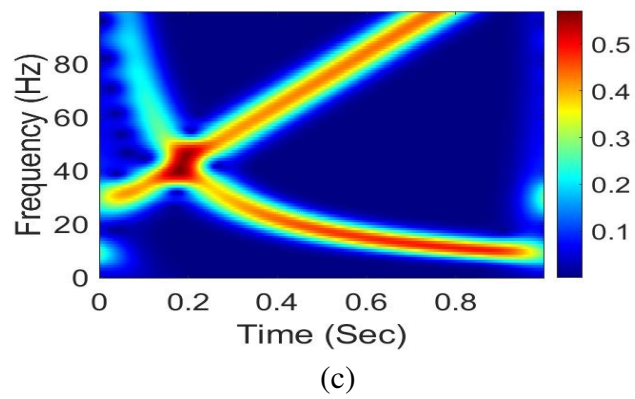
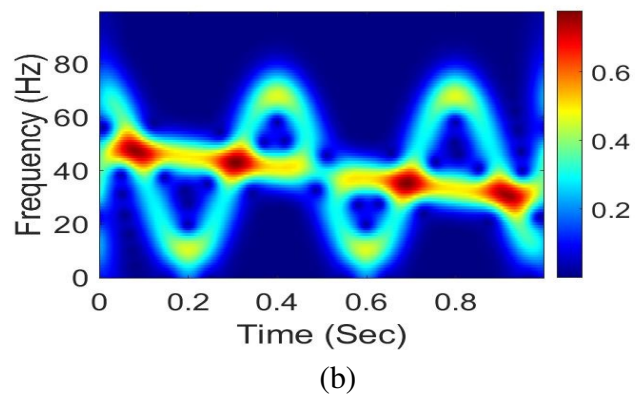
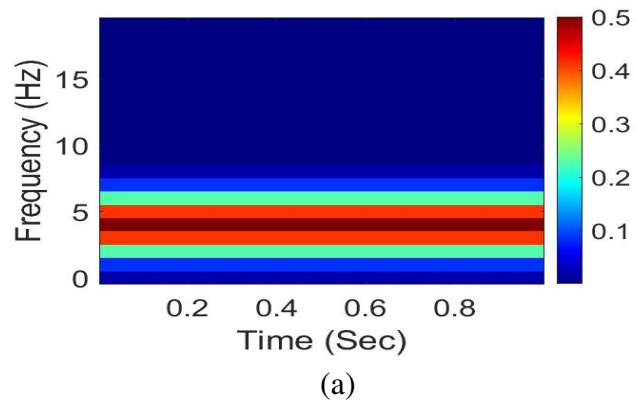


Figure 2.7 The time-frequency plot, using method mentioned in Moukadem et al. (2015) of the signals (a) $x_1(t)$ (b) $x_2(t)$ (c) $x_3(t)$ (d) $x_4(t)$

2.2 MODIFIED ST BASED ON COMPACT SUPPORT KERNEL

Different modifications of ST that have been discussed above, do not have compact support window function. Due to the infinite support of the kernel, an implementation of the exact algorithm is not possible. Therefore, to overcome this issue, the following modifications using compactly supported kernel for ST are proposed.

2.2.1 Variation 5: Modified ST with compactly supported kernel (CSKST)

Zidelmal et al. (2017) have proposed a kernel for ST which has a compact support. They have used a kernel defined as follows:

$$w(t) = \begin{cases} \frac{1}{C_\gamma}(1-t^2)^\gamma, & \text{if } t^2 < 1 \\ 0, & \text{otherwise} \end{cases} \quad (2.2.1)$$

where $\gamma = \frac{1}{2\sigma^2}$ and C_γ is obtained numerically as

$$C_\gamma = \Delta t \sum_{i=1}^N (1-t_i^2)^\gamma \quad (2.2.2)$$

where $t_i = -1 + i\Delta t$ and $\Delta t = \frac{2}{N}$

For a variable support λ , the kernel can be defined as

$$w_\lambda(t) = \begin{cases} \frac{1}{C_\gamma D_\gamma}(\lambda^2 - t^2)^\gamma, & \text{if } t^2 < \lambda^2 \\ 0, & \text{otherwise} \end{cases} \quad (2.2.3)$$

The scale parameter λ is assumed to be a function of frequency which is defined as

$$\lambda(f) = \frac{m}{p + f^r} \quad (2.2.4)$$

The CSKST is then defined as follows:

$$S_x^{m,p,r}(t, f) = \frac{1}{C_\gamma} \left(\frac{p + f^r}{m} \right)^{2\gamma+1} \int_{-\infty}^{\infty} x(t) \left(\frac{m^2}{(p + f^r)^2} - (t - \tau)^2 \right)^\gamma e^{-i2\pi ft} dt \quad (2.2.5)$$

Here the values of m, p and r are determined based on maximizing the energy con-

centration measure

$$CM(m, p, r) = \frac{1}{\int_{-\infty}^{\infty} \int_{-\infty}^{\infty} \left| \overline{S_x^{m,p,r}}(t, f) \right| dt df} \quad (2.2.6)$$

where,

$$\overline{S_x^{m,p,r}}(t, f) = \frac{S_x^{m,p,r}(t, f)}{\sqrt{\int_{-\infty}^{\infty} \int_{-\infty}^{\infty} |S_x^{m,p,r}(t, f)|^2 dt df}} \quad (2.2.7)$$

The optimization problem can be written as

$$\arg \max_{m,p,r} \left(\frac{1}{\sqrt{\sum_1^N \sum_{f_{min}}^{f_{max}} |\overline{S_x^{m,p,r}}(t, f)|}} \right)$$

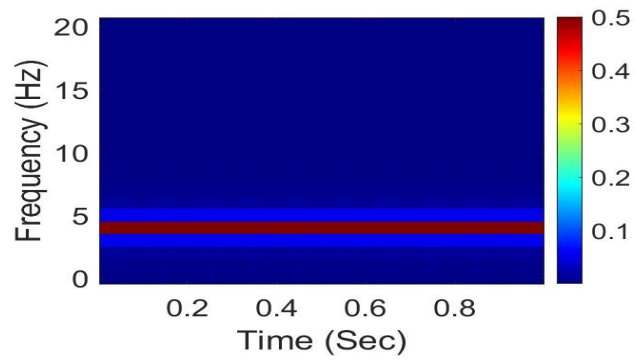
subject to:

$$\begin{aligned} KT_s f_{max}^r - pKT_s - m &\leq 0 \\ m/(p+1) - LT_s &\leq 0 \\ 0 \leq m, p &\leq 3 \\ 0 \leq r &\leq 1 \end{aligned} \quad (2.2.8)$$

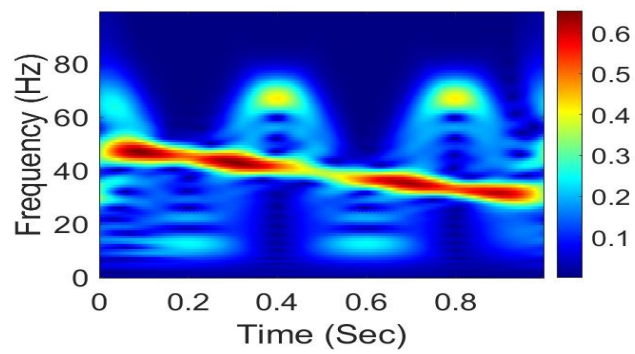
Note that there is no analytical expression for C_γ in Eq. (2.2.2) which turns out to be one of the drawbacks of this approach.

2.2.1.1 Observations

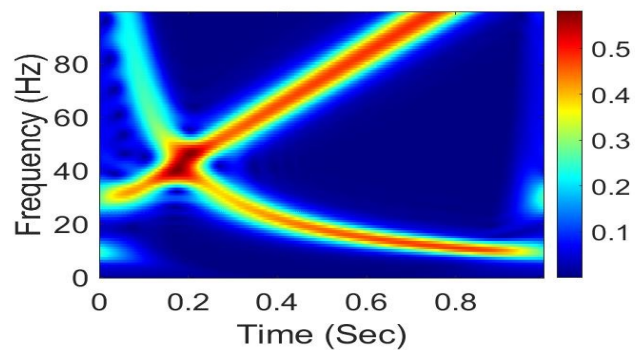
1. In CSKST, when the frequencies vary slowly, a good frequency resolution is achieved at all frequencies. This can be observed in case of signal $x_4(t)$ in Figure 2.8(d)
2. However, it can be clearly seen in Figure 2.8(b) that, when the frequency varies periodically, CSKST is unable to capture the exact spectrum.



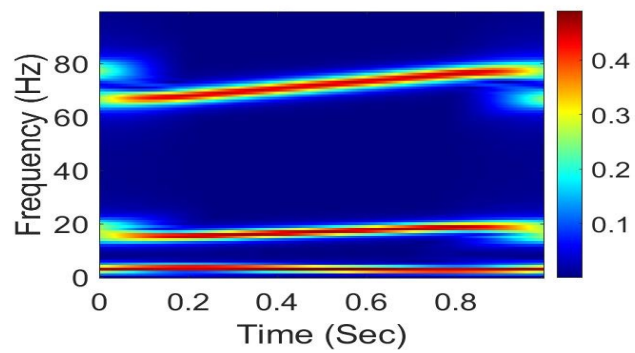
(a)



(b)



(c)



(d)

Figure 2.8 The time-frequency plot, transformed using CSKST of signals (a) $x_1(t)$ (b) $x_2(t)$ (c) $x_3(t)$ (d) $x_4(t)$

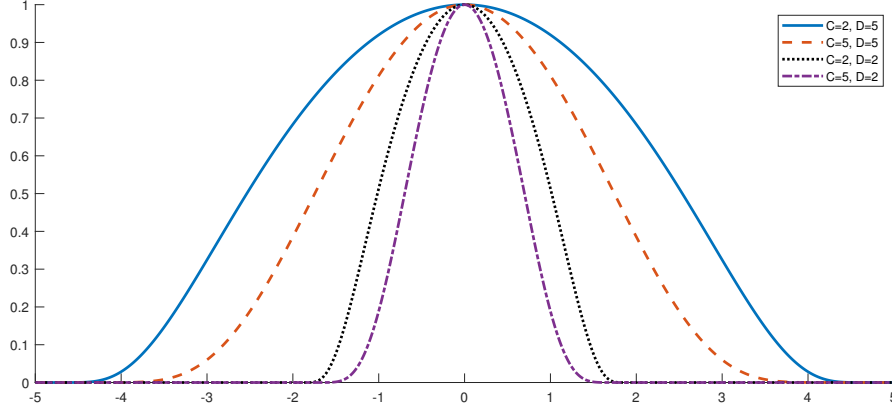


Figure 2.9 Variation of the CB kernel with change in parameters C and D

2.2.2 Proposed ST using a modified kernel

Inspired from the above approach, we propose a variation of compactly supported Cheriet-Belouchrani (CB) kernel, instead of original Gaussian kernel.

2.2.2.1 General form of CB kernel

The general form of CB kernel (Abed et al., 2012; Abed and Belouchrani, 2018) is given by the following expression

$$G_{CB}(t, \tau) = \begin{cases} e^{e_{CB}}, & \text{if } \frac{t^2 + \tau^2}{D^2} < 1 \\ 0, & \text{otherwise} \end{cases} \quad (2.2.9)$$

where,

$$e_{CB} = C + \frac{CD^2}{t^2 + \tau^2 - D^2} \quad (2.2.10)$$

For a fixed support D , values of C determine the shape of the kernel. On increasing the values of C , the kernel width reduces. The variations in the kernel width with different values of C and D are demonstrated in Figure 2.9.

2.2.2.2 Proposed CBST

The proposed kernel for CBST with compact support is similar to Eq. (2.2.9), which is defined as:

$$w_{CB}(t, f) = \begin{cases} \frac{1}{\kappa} e^{\frac{CD(f)^2}{t^2 - D(f)^2}}, & \text{if } t^2 < D(f)^2 \\ 0, & \text{otherwise} \end{cases} \quad (2.2.11)$$

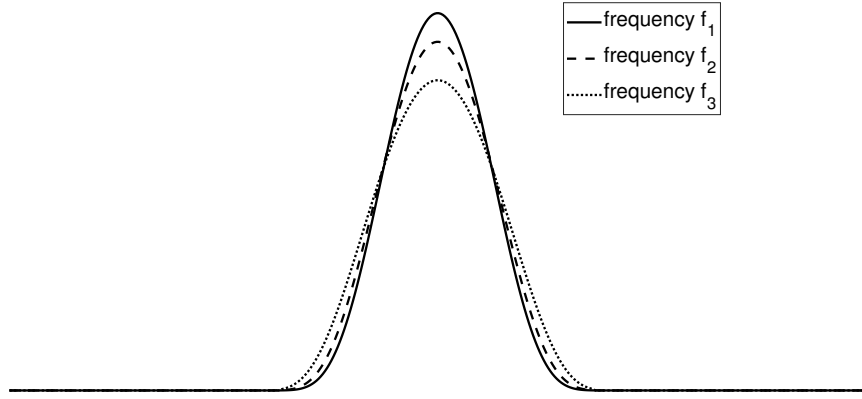


Figure 2.10 Variation of the proposed window with frequencies $f_1 < f_2 < f_3$, for fixed values of parameters m, p, k and C .

Here, κ ensures that the normality condition in Eq. 2.1.1 is satisfied, and is given by

$$\kappa = \int_{-D(f)}^{D(f)} e^{\frac{CD(f)^2}{t^2 - D(f)^2}} dt \quad (2.2.12)$$

The function $D(f)$ determines the support of the kernel, and is designed in such a way that it decreases with increase in frequency and vice-versa which is given below:

$$D(f) = mf^p + k \quad (2.2.13)$$

where $p \leq 0$, m and k are constants whose values are determined using optimization technique discussed in the next subsection.

Thus, the proposed CBST can be defined by

$$X_S(t, f) = \int_{-\infty}^{\infty} x(\tau) w_{CB}(\tau, f) e^{-i2\pi f t} d\tau \quad (2.2.14)$$

2.2.2.3 Optimization of CBST kernel parameters

A concentration measure M_X^α (Stanković, 2001; Sejdic et al., 2008) is used for optimization of the kernel parameters C in Eq. 2.2.11, and p, k, m in Eq. 2.2.13. It is defined as:

$$M_X^\alpha = \left(\int_{-\infty}^{\infty} \int_{-\infty}^{\infty} |\tilde{X}_S(\tau, f)|^{\frac{1}{\alpha}} d\tau df \right)^\alpha \quad (2.2.15)$$

where X_S is the a time-frequency representation of the signal $x(t)$ using CBST. Here, $\tilde{X}_S(\tau, f)$ is given by:

$$\tilde{X}_S(n, k) = \frac{X_S(\tau, f)}{\sqrt{\int_{-\infty}^{\infty} \int_{-\infty}^{\infty} |X_S(\tau, f)|^2}} \quad (2.2.16)$$

The objective function is based on minimizing the concentration measure shown in Eq.(2.2.15). The value of α is dependent on the application. Most of the researchers (Sejdic et al., 2008; Moukadem et al., 2015; Zidelmal et al., 2017) have chosen $\alpha = 1$.

We define the objective function for optimization of the kernel parameters as:

$$\arg \min_{m,p,k,C} (M_X^\alpha) \quad (2.2.17)$$

subject to:

$$\begin{aligned} 0 &\leq m \leq 10 \\ -10 &\leq p \leq 0 \\ 0 &\leq k \leq 10 \\ 0 &\leq C \leq 10 \end{aligned}$$

The ranges for m , p , k , and C are determined experimentally based on the application.

2.2.2.4 Observations

1. Unlike the conventional ST, the frequency-resolution does not vary with frequency. At higher frequencies the frequency resolution improves in case of CBST.
2. When the frequency varies periodically, as seen in Figure 2.11(b), the frequency resolution is better in case of CBST than that of CSKST.

2.2.3 Numerical comparison of proposed CBST with conventional ST and CSKST

Renyi entropy can be considered as an effective measure for estimating the information content in the time-frequency distribution of the signal (Baraniuk et al., 2001), which is defined as:

$$R_X^\alpha = \frac{1}{1-\alpha} \log_2 \left(\sum_{n=1}^N \sum_{k=1}^N |X_S^\alpha(n, k)| \right), \quad (2.2.18)$$

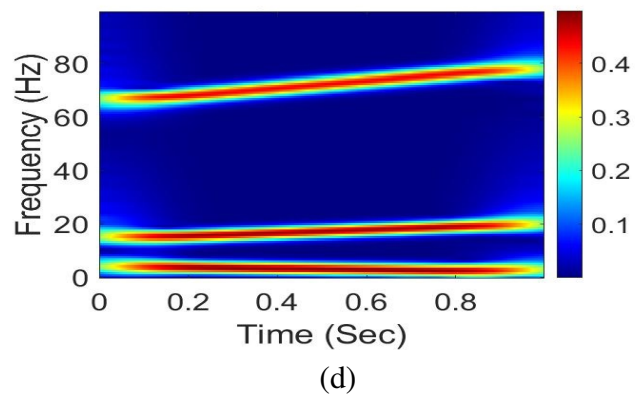
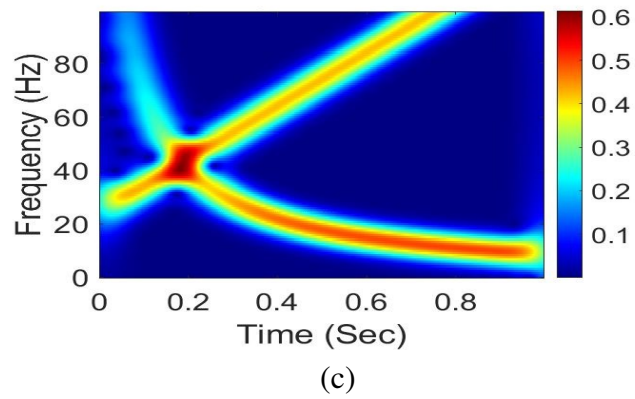
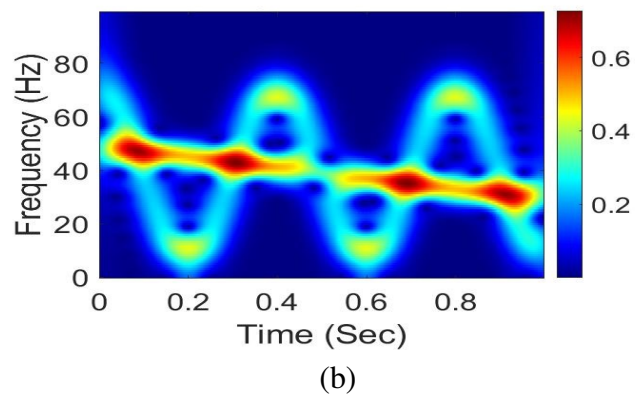
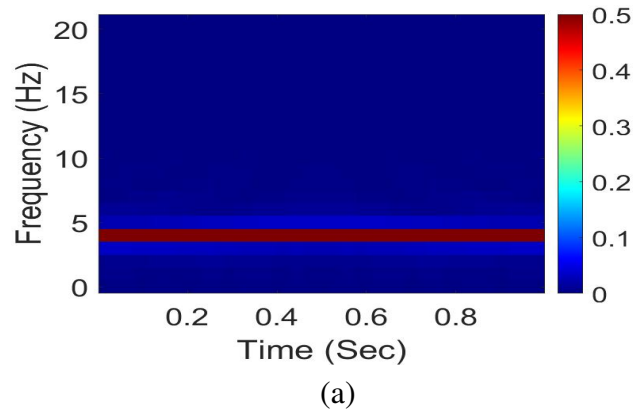


Figure 2.11 The time-frequency plot transformed using proposed CBST, for the signals (a) $x_1(t)$ (b) $x_2(t)$ (c) $x_3(t)$ (d) $x_4(t)$

where, α is chosen as 2. A lower entropy indicates better concentration of energy in the time-frequency domain. The CBST possesses minimum Renyi entropy in most of the test signals as compared to ST and CSKST which is evident in Table 2.1.

Table 2.1 Renyi entropy of variations of ST having compact support using the test signals

Method	$x_1(n)$	$x_2(n)$	$x_3(n)$	$x_4(n)$
ST	11.713	15.555	15.384	15.728
CSKST	10.721	15.424	15.074	14.439
CBST	10.4371	15.361	15.019	14.422

2.3 DISCRETE ORTHONORMAL STOCKWELL TRANSFORM

Discrete orthonormal S-transform (DOST) for a one-dimensional signal u with N samples was introduced by Stockwell (2007) which can be defined as follows:

$$S[\tau, \nu] = \sum_{k=0}^{N-1} u[k] S_{\nu, \beta, \tau}[k], \quad (2.3.1)$$

where,

$$S_{\nu, \beta, \tau}[k] = \frac{ie^{-i\pi\tau}}{\sqrt{\beta}} \frac{e^{-i2\pi(k/N - \tau/\beta)(\nu - \beta/2 - 1/2)} - e^{-i2\pi(k/N - \tau/\beta)(\nu + \beta/2 - 1/2)}}{2\sin(\pi(k/N - \tau/\beta))} \quad (2.3.2)$$

Here, $\{S_{\nu, \beta, \tau}[k] | \nu, \beta, \tau, k\}$ is a set of basis functions where β determines the frequency bandwidth, τ gives the local time sample, and ν is referred as the "voice" which is similar to the centre frequency. Thus, the basis function is defined for a given time τ , along a certain central frequency ν having a fixed bandwidth of β . Moreover, the set of these basis functions given by Eq. 2.3.2 are orthonormal to each other (Stockwell, 2007).

In octave sampling (where the bandwidth increases dyadically, with the increase in voice), for a signal with N samples, such that N is a power of 2, a variable p can be introduced such that $p = 0, 1, \dots, \log_2(N) - 1$. While a detailed description of DOST can be found in Stockwell (2007), the relations between p, β, ν, τ , are given as follows:

For $p = 2, \dots, \log_2(N) - 1$,

$$\beta = 2^{p-1} \quad (2.3.3)$$

$$\nu = 3 \times 2^{p-2} \quad (2.3.4)$$

$$\tau = 0, 1, \dots, 2^{p-1} - 1 \quad (2.3.5)$$

2.4 TWO DIMENSIONAL DOST

Two-dimensional DOST (2D-DOST) is defined by Drabycz et al. (2009) for an image $I[x, y]$ of size $M \times N$ as shown below:

$$S[x', y', v_x, v_y] = \frac{1}{\sqrt{2^{p_x + p_y - 2}}} \sum_{m=-2^{p_x-2}}^{2^{p_x-2}-1} \sum_{n=-2^{p_y-2}}^{2^{p_y-2}-1} \left(I_f[m + v_x, n + v_y] e^{2\pi i \left(\frac{mx'}{2^{p_x-1}} + \frac{ny'}{2^{p_y-1}} \right)} \right) \quad (2.4.1)$$

where $p_x = 2, \dots, \log_2(M) - 1$, $p_y = 2, \dots, \log_2(N) - 1$; v_x and v_y are defined in terms of p_x and p_y , respectively using Eq. (2.3.4). And the two dimensional Fourier transform $I_f[m, n]$ of the image $I[x, y]$ is defined as

$$I_f[m, n] = \sum_{x=0}^{M-1} \sum_{y=0}^{N-1} I[x, y] e^{-2\pi i \left(\frac{mx}{M} + \frac{ny}{N} \right)} \quad (2.4.2)$$

The DOST coefficients of an image can be divided into different voice-images. Each voice-image consists of a set of coefficients $S[x', y', v_x, v_y]$ with the same value of voice pairs (v_x, v_y) . The size of these voice-images depends on the value of the voice pairs (v_x, v_y) . These voice-images are used to despeckle the SAR images in Chapter 5.

2.4.1 2D-DOST patterns for some binary images

A white dot at location $(2, 2)$ is placed on an image with black background of size 256×256 . The image is observed in the DOST domain which is shown in Figure 2.12. The white lines in the transformed image indicate the effect of DOST on the white-dot in a black background. Voice images in DOST domain can be seen clearly here. Since octave sampling is employed, the voice sizes vary in a dyadic manner. The effect of DOST on horizontal and vertical lines are also shown in Figure 2.13

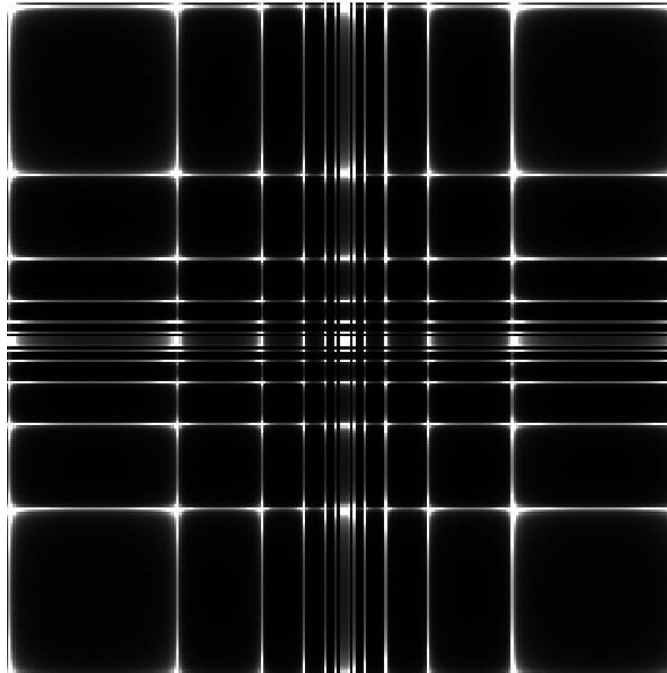


Figure 2.12 2D - DOST of the image with a white dot with black background

2.5 CONCLUSION

In this chapter, we have reviewed the different modified forms of ST present in literature. The kernel width in the traditional ST varies with frequency. However, the frequency resolution reduces at higher frequencies. A lot of research work has been done by other researchers on modifying the gaussian kernel to improve the resolution.

We have introduced a compactly supported CB kernel for ST that offers superior frequency resolution compared to the traditional ST. We have made use of this ST with compactly supported kernel, in Chapter 4, along with artificial neural network, to predict the wind speed.

ST contains highly redundant coefficients. To this end, in this chapter, we discuss about discrete orthonormal S-transform (DOST). While it is based on ST, it employs orthonormal basis functions for its representation. Due to the sheer amount of transformation coefficients, image transformation using conventional ST is not ideal. The DOST coefficients are non-redundant. This makes it an ideal candidate for image processing applications.

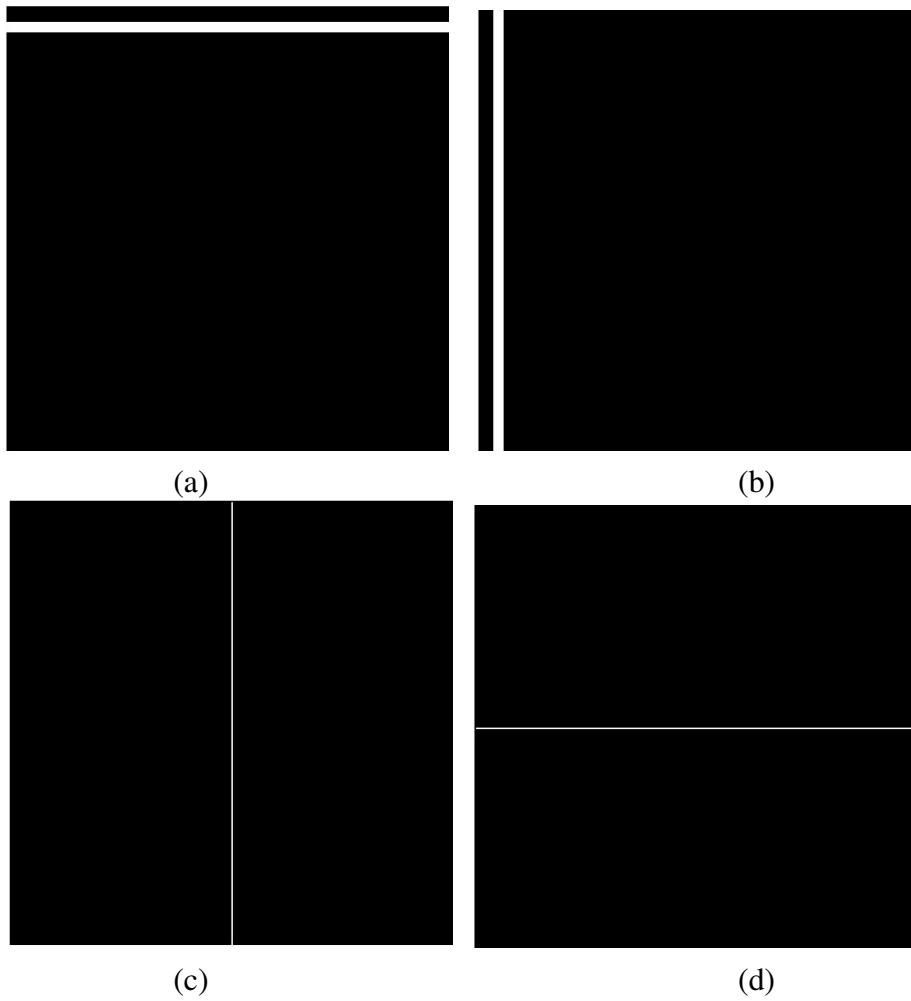


Figure 2.13 (a) Image with a white horizontal line (b) Image with a white vertical line
 (c) 2D - DOST of image in (a) (d) 2D - DOST of image in (b)

CHAPTER 3

DETECTION OF OCULAR ARTEFACT IN EEG SIGNAL USING S-TRANSFORM

EEG signals are complex signals that record the brain activity. They are measured by either placing electrodes on the scalp or surgically placing electrodes on the exposed surface of the subject's brain. Most commonly, these EEG recordings are recorded for a few hours to analyse the underlying dynamics of the brain. EEG can provide various information about nervous system related disorders like epilepsy, Alzheimer's disease, dementia.

The placement of the electrodes to record EEG signals using the 10-20 system is shown in the Figure 3.1

The 10-20 system is a standardized, internationally recognised system which shows how the electrodes are placed on the scalp of the subject. This system allows the electrodes to be placed on all the regions of the brain, namely: frontal (F), parietal (P), temporal (T) and occipital (O). The electrodes placed on the left-hand side of the brain are labelled with odd numbers whereas on the right-hand sides are labelled with even number. And the midline electrodes are labelled "z" instead of using numbers for labelling. The electrodes which are labelled FP1 and FP2 are placed above the eye. Since the EEG is recorded over a long period of time, the patient may move about and also look around causing muscle and ocular artefact, respectively in the EEG signals. This may contaminate the EEG signal.

For the medical examiners to analyse pure EEG signals, such artefacts need to be removed. A lot of work are available in literature to remove the artefacts from EEG signal. Some of the methods suggest the use of independent component analysis (ICA) and its variations (Akhtar et al., 2012). However, there are reports suggesting that the usage of ICA affects the phases of the signals. Also, artefact detection techniques need human intervention to determine which of the independent component contains

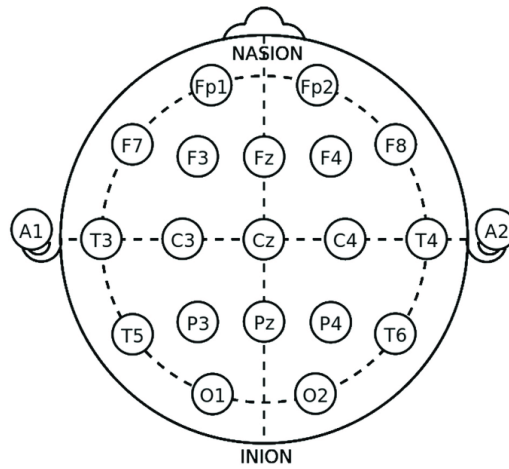


Figure 3.1 The 10-20 electrode placement system to record EEG (Rojas et al., 2018)

the artefact so as to separate it from the rest of the EEG signals (Devuyst et al., 2009; Jung et al., 2000). Efforts are being made by researchers to avoid the human intervention in ICA driven techniques (Radüntz et al., 2015). Some other removal techniques using discrete wavelet transform (DWT), discrete cosine transform (DCT) have also been suggested and implemented successfully in Krishnaveni et al. (2006); Senapati and Routray (2011); Zikov et al. (2002). Ocular artefact removal is also attempted by many researchers using S-transform and its modified versions (Senapati and Routray, 2011; Upadhyay et al., 2015). However, these techniques do not make use of the phase information in the EEG signals. The phase of EEG signals determines the signal interdependency. Phase of the EEG signal is investigated by da Silva (2006) to identify the underlying neural activity in the EEG signal.

This study aims at automatic detection of ocular artefacts using phase information extracted from S-transform of EEG signals.

Artefacts are unwanted components in the EEG signals which may affect the signal reading, thereby not allowing the signal to be interpreted properly. One of the most common artefacts is the ocular artefact. This artefact arises due to the movement of the eye including eye-blinks. In most cases, detection of ocular artefacts in EEG signals is done by skilled professionals who are small in number. We propose a new approach of automatic detection of ocular artefacts using the phase information present in the S-transform of EEG signal. S-transform of a signal provides absolutely referenced phase information of the signal in addition to time-frequency information. A time delay exists between the signals recorded by electrodes placed at different distances from the point of origin of the artefact. This time delay translates to phase shift in the frequency domain. The phase information of the EEG signal recorded from different electrodes placed in the frontal region are used to detect the artefacts generated near the eye.

3.1 ANALYSIS OF EEG SIGNAL USING CROSS-ST

In this study, time, frequency and phase analysis of EEG signal has been carried out using ST. The signal due to eye movements generated near one electrode affects the signals at neighbouring electrodes. However, upon measuring the signals at two neighbouring electrodes, a small time delay exists which corresponds to the propagation delay. The propagation delay is indicated by phase change in the corresponding ST of the signals. This phase change can be used to detect the source of the signal in a patient. For example, the phase information present in the signal can be used to find the origin of the ictal spikes in epilepsy patients and can also be used to determine if the seizure was due to a focal discharge or a generalized one (Pinnegar et al., 2009). However, it was also pointed out that if the ictal events are very close to each other, a wide Gaussian window function in the ST can not discriminate between the ictal spikes. And if the noise in the recorded EEG signal is high, the ST may not be useful. The phase between the two signals is measured as phase synchrony. Lower values of phase synchrony indicates low correlation between the signals.

Since the ST localizes spectral components in time, the cross correlation of specific events in two spatially separated S-transforms gives the phase difference and hence the phase synchrony can be estimated.

Cross-ST of two signals $x(t)$ and $y(t)$ is defined as follows (Assous and Boashash, 2012)

$$CrossST(t, f) = X_S(t, f).Y_S(t, f)^* \quad (3.1.1)$$

where $()^*$ denotes the complex conjugate.

The phase of the cross-ST is given by Assous and Boashash (2012)

$$arg(CrossST(t, f)) = \phi_x(t, f) - \phi_y(t, f) \quad (3.1.2)$$

where ϕ_x and ϕ_y are phases of the signals $x(t)$ and $y(t)$ respectively. The above equation shows that the phase difference (phase synchrony) between the two signals is equal to cross-power spectrum.

It is not very hard to show that, if a signal $x(t)$ in time domain is shifted by time t_1 , then the phase of the signal in its S-transform domain is shifted by $2\pi ft_1$ which is also observed in Fourier transform. This can be explained as follows.

If a signal originating near an electrode consists of ocular artefact, its neighbouring electrodes also record this activity with some propagation delay. This propagation delay translates to phase shift in the transformed domain. Also it is known that, higher values

of phase synchrony indicates higher correlation between the signals. One can use electrodes close to the eye (example FP1, F3, F7 electrodes for the left eye and FP2, F4, F8 for the right eye in 10-20 system positioning) to obtain the phase plot. This phase plot is obtained using cross-ST.

In order to check if the ocular artefact originated from the left eye, signals recorded at electrodes FP1, F3 and F7 are considered. High values of phase synchrony between the signals at electrodes pairs (FP1 and F3) and (FP1 and F7) at the same point of time indicates that an artefact generated near electrode FP1 has propagated to F3 and F7. This segment of the signal is considered to contain an ocular artefact if it lies in the frequency band of 0-16Hz and the signal at electrode FP1 has relatively high amplitude.

An algorithm is given below to detect ocular artefacts generated by left eye using the electrodes FP1, F3 and F7.

Algorithm 1 Algorithm to detect ocular artefacts using electrodes FP1, F3 and F7

Input: EEG segments at electrodes FP1, F3, F7

Output: Ocular artefact zones along the time axis (*artefactDetected*)

```

1: procedure ARTEFACT-DETECT
2:    $S1(t, f) = ST(\text{EEG segments at electrodes FP1})$ 
3:    $S2(t, f) = ST(\text{EEG segments at electrodes F3})$ 
4:    $S3(t, f) = ST(\text{EEG segments at electrodes F7})$ 
5:    $\text{crossST}_{FP1F3} = S1(t, f) \cdot S2(t, f)^*$ 
6:    $\text{crossST}_{FP1F7} = S1(t, f) \cdot S3(t, f)^*$ 
7:   for all rows  $i$  and columns  $j$  of the matrices, select  $0 < \text{frequency} < 16\text{Hz}$ 
8:   if  $\text{abs}(S1(i, j)) \geq \text{threshold}_1$  and  $\text{abs}(\text{angle}(\text{crossST}_{FP1F3}(i, j))) \geq$ 
    $\text{threshold}_2$  and  $\text{abs}(\text{angle}(\text{crossST}_{FP1F7}(i, j))) \geq \text{threshold}_3$  then
9:      $\text{artefactDetected}(j) \leftarrow 1$ 
10:  if  $\text{artefactDetected}(j) = 1$  then
11:    for  $k=j:1$  do
12:      if  $\text{crossST}_{FP1F3}(i, k) > \text{threshold}_2$  and  $\text{crossST}_{FP1F7}(i, k) > \text{threshold}_3$ 
   then
13:         $\text{artefactDetected}(k) \leftarrow 1$ 
14:    end for

```

3.2 RESULTS AND DISCUSSION

In this study, 19 electrodes are used to collect the EEG data, from a healthy human subject, with a sampling rate of 256 Hz. The signal is preprocessed using a low pass

filter with a cut-off frequency of 30 Hz followed by normalization. Normalisation removes any unwanted bias during signal acquisition. The signal consists of eye-blink artefacts and the signals at electrodes labelled FP1, F3, and F7, using average reference montage, are shown in Figure 3.2(a), 3.2(b) and 3.2(c) respectively. The S-transforms of these signals are displayed in Figure 3.3(a), 3.3(b), 3.3(c). The amplitude of ST are colour-coded from blue to red as shown in these figures.

The phase synchrony between signals at electrodes (FP1 and F3) and (FP1 and F7) are displayed in Figure 3.4(a) and Figure 3.4(b) respectively. These phase synchrony values are colour-coded from blue to red. It is found that the phase synchrony values are high at eye blinks. Also the signal zones where phase synchrony values are high for the signal at electrode FP1 with respect to signal at neighbouring electrodes (F3 and F7) are considered as ocular artefacts. The ocular artefact zone for the signal captured by the electrode FP1 is shown in Figure 3.5.

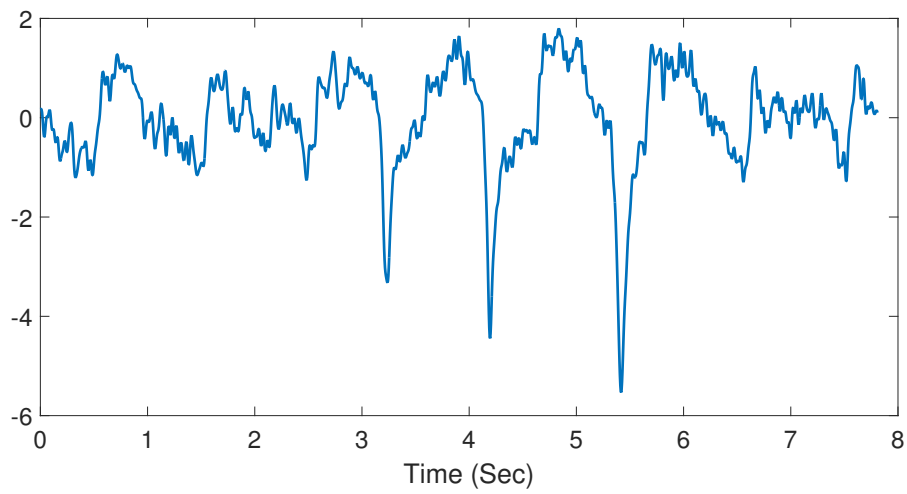
Three threshold values are used in the algorithm. Here, $threshold_1$ indicates the minimum amplitude of the signal that can be considered as an eye blink. This value of $threshold_1$ is the sum of mean and standard deviation of the signal.

The other two thresholds, namely $threshold_2$ and $threshold_3$ determine the minimum phase difference that should exist between the two signals for interpreting the signal as an artefact. Both these values (in radian) are suitably chosen to be unity. Note that the threshold values can be made to change adaptively.

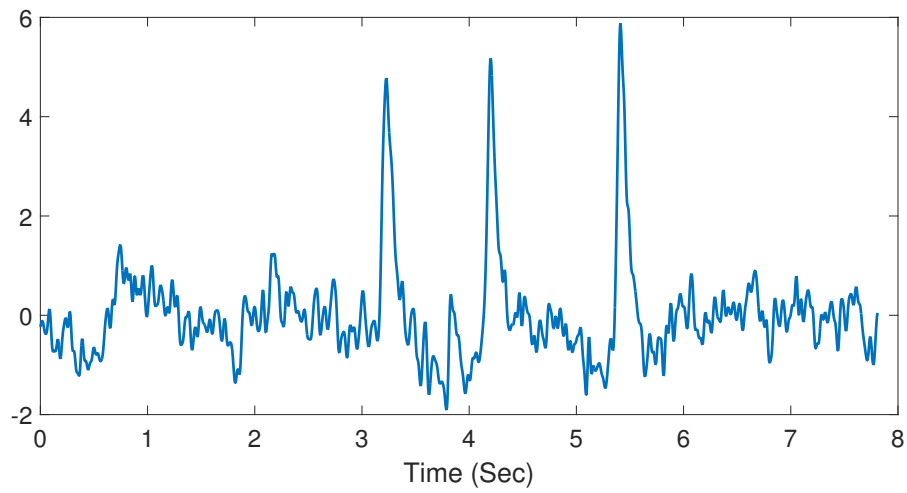
3.3 CONCLUSION

Artifacts are unwanted components of the EEG signal. We have made an attempt to automatically detect the eye-blink ocular artifact from the EEG signal using phase information present in the S-transform of the EEG signal. For a signal originating from a given region, a phase difference due to propagation delay exists between neighbouring electrodes. This phase information has been used while determining the artifacts in the signal.

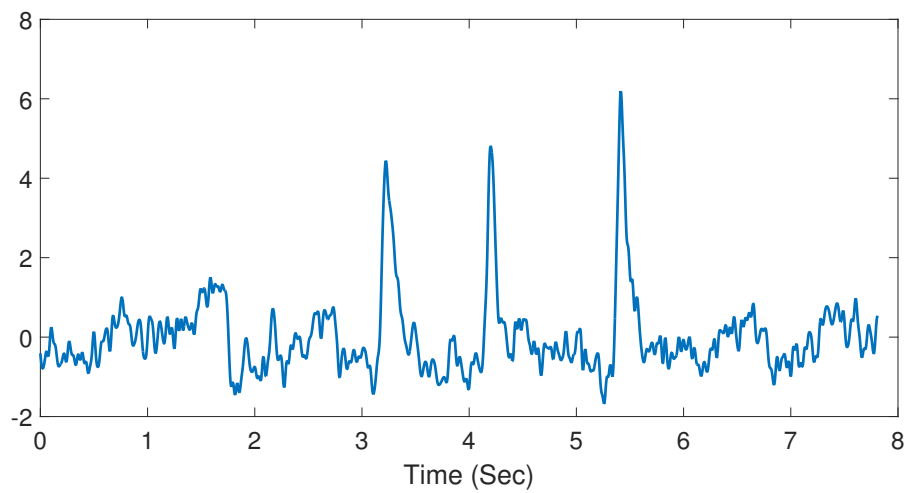
This detection technique could be extended to detect other artifacts in EEG signal and recognize their origin so that they can be successfully removed from EEG signal.



(a)

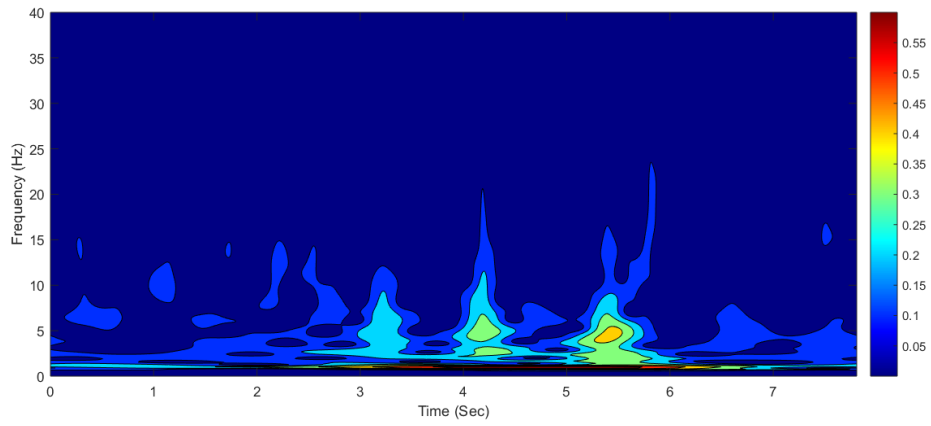


(b)

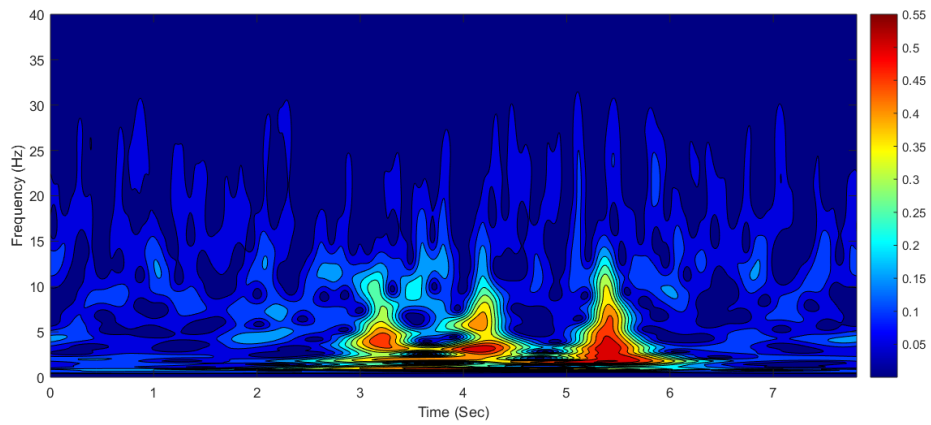


(c)

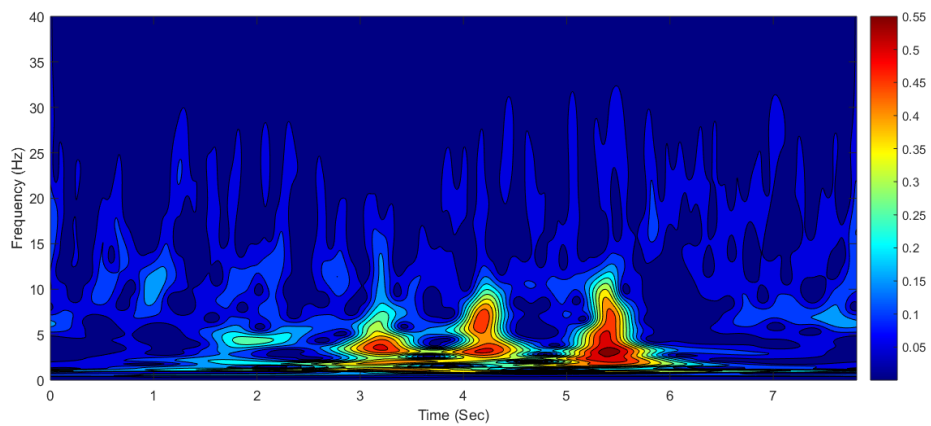
Figure 3.2 EEG signal at electrodes (a) FP1 (b) F3 (c) F7 using average montage



(a)

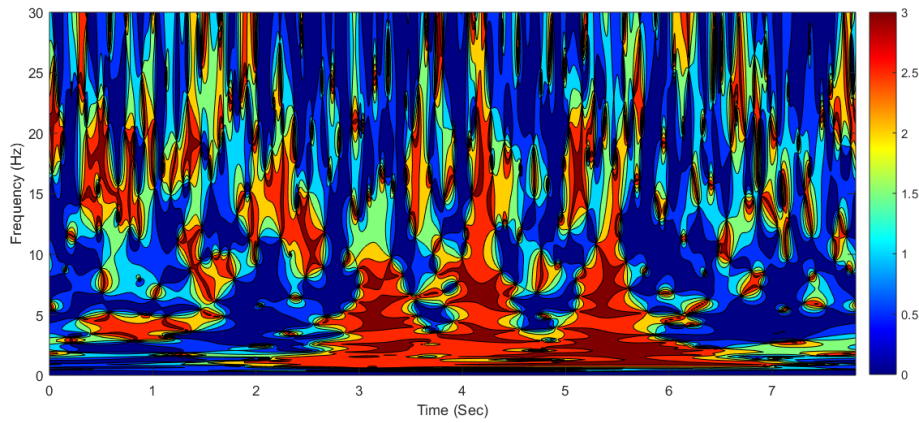


(b)

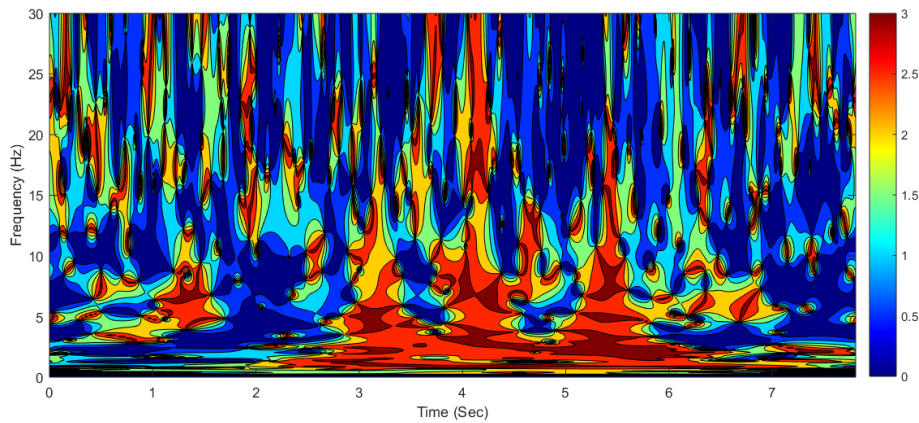


(c)

Figure 3.3 S-transform of EEG signal at electrodes (a) FP1, (b) F3, (c) F7. The graphs are colour coded to indicate the amplitude values of the signal components, which varies continuously from blue via green, yellow to red. The blue and red indicate the low and high values of the amplitude respectively.



(a)



(b)

Figure 3.4 Phase synchrony between the signals at electrodes (a) FP1 and F3 and (b) FP1 and F7. The colour bar with blue via yellow to red indicate phase difference (in radian) between the signals. Higher phase difference is indicated in red.

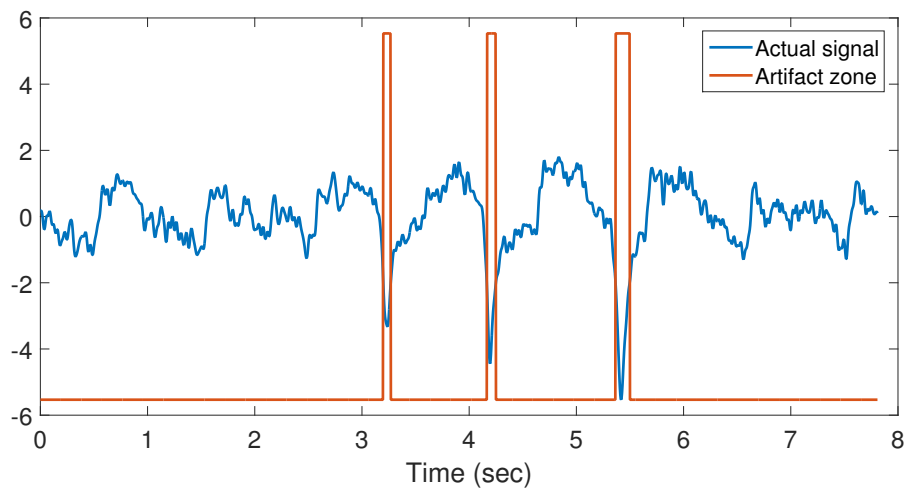


Figure 3.5 The signal at electrode FP1: red vertical boxes denote the detected ocular artefact zone due to eye blink

CHAPTER 4

SHORT-TERM WIND SPEED FORECASTING USING S-TRANSFORM WITH COMPACTLY SUPPORTED KERNEL AND ARTIFICIAL NEURAL NETWORK

Wind energy is one of the most abundant, clean, feasible, and fast-growing renewable energy sources. However, due to the intermittent nature of wind, the operators face various issues and challenges in scheduling, management of reserves, and integration of wind energy into the grid. Thus, forecasting wind speed becomes essential to mitigate the impact of unpredictability inherent to the wind.

The methods for forecasting wind speed are divided into three major categories, namely very-short term (up to 30 minutes), short-term (generally less than 6 hours), and long-term (day/week ahead) prediction (Marugán et al., 2018).

Long-term forecasting is used to predict wind speed, using physical methods that involve other meteorological data. Numerical weather predictors in association with neural networks are employed for long-term prediction (Ramasamy et al., 2015; Shamshirband et al., 2016).

Short-term forecasting of wind speed is essential for efficient power management and scheduled maintenance of the wind power systems. Generally, these forecasting methods involve statistical and machine learning algorithms such as models based on autoregressive moving average (ARMA), support vector machines (SVM), and artificial neural networks (ANN) (Tascikaraoglu and Uzunoglu, 2014).

In short-term forecasting, many of the recent works on wind speed prediction, decompose the wind speed data into several sub-series before forecasting. Wavelet transforms (Liu et al., 2013; Ramesh Babu and Arulmozhivarman, 2013; Doucoure et al., 2016; Yu et al., 2017b), and empirical mode decompositions (EMD), and their varia-

tions (Liu et al., 2012; Hong et al., 2013; Ren et al., 2014; Yu et al., 2017a; Han et al., 2018; Santhosh et al., 2018; Mi et al., 2019; Qu et al., 2019; Singh and Pradhan, 2020; Liu et al., 2020; Zhang et al., 2020b) are a few of the popular methods to decompose the time series. Variations of models based on ANN, SVM, and ARMA are some of the most popular choices for short-term prediction (Marugán et al., 2018; Qian et al., 2019).

Singular spectrum analysis (SSA) is used in combination with many of the signal decomposition techniques to improve the prediction accuracy (Yu et al., 2017a,b; Mi et al., 2019).

Yu et al. (2017b) decomposed the wind speed using three-level wavelet decomposition. The trend of the sub-series having the highest frequency is extracted using SSA. Elman neural network is used to predict each of the sub-series. The final prediction is obtained by combining all the prediction results.

Very short-term forecasting of the wind speed was carried out by Singh et al. (2019). They used maximal overlap discrete wavelet transform (MODWT) to divide the wind speed into several sub-series followed by prediction using autoregressive integrated moving average (ARIMA). Wind speed forecasting was finally achieved by applying inverse-MODWT to all the forecast sub-series.

The EMD based decomposition techniques result in several intrinsic mode functions (IMF) and a residue. In some of the methods that utilize EMD, the IMF with the highest frequency component, referred to as IMF1, is modified (or discarded) for better prediction accuracy. Yu et al. (2017a) compared the prediction accuracy of different variations of EMD. They obtained the IMFs by applying EMD, EEMD (ensemble EMD), CEEMDAN (complete EEMD with adaptive noise). Denoising was done by applying SSA on IMF1. Then, wind speed forecasting was achieved by predicting the IMFs and residue using Elman neural network. Han et al. (2018) decomposed the wind speed series using EMD and applied the linear (ARIMA) model on EMD residue and one of the non-linear prediction models SVM, random forest (RF), backpropagation (BP), extreme learning machines (ELM) and CNN on the IMFs. Mi et al. (2019) used SSA for denoising the wind speed time series, followed by feature prediction using a variation of SVM. These features were obtained by decomposing wind speed data using EMD. The final result is obtained by the recombination of various predictions. Qu et al. (2019) used CEEMDAN to decompose the wind speed data. Empirical wavelet transform is employed to further decompose the IMF1. Prediction of the time series is achieved by using a backpropagation neural network whose parameters are optimized using flower-pollination algorithm. IMFs generated from an improved CEEMDAN was used by Liu et al. (2020). A new time series is constructed discarding the IMF1. Various

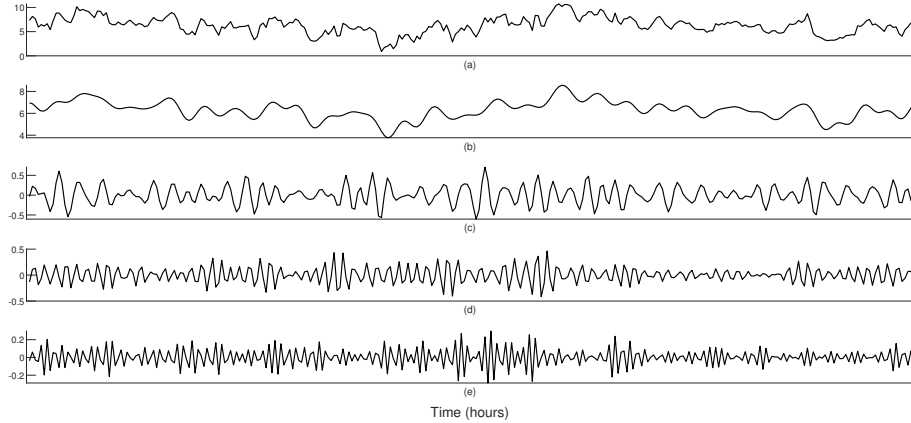


Figure 4.1 Wind speed time series of Case 2 and its four decomposed sub-series of different frequency bands, using CBST, in increasing order (top to bottom).

forecasting algorithms are used to forecast wind speed. Lorenz disturbance sequence along with EMD based decomposition was used by Zhang et al. (2020b) for forecasting of the wind speed. The prediction was made by applying a radial basis kernel function (RBF) neural network on the IMFs and ARIMA on residue. Zhang et al. (2020a) used variational mode decomposition (VMD) to decompose the wind speed. While the forecasting for the linear part of the wind speed was carried out using ARMA, principal component analysis - RBF (PCA-RBF) was used to forecast the non-linear part.

In order to predict wind speed, we have used CBST along with ANN. We have termed this procedure as "CBST-ANN". In this work, we conduct a study on the effect of the decomposition of the data into several sub-series, in the prediction model. For forecasting, the time-series is first decomposed into equal-width frequency bands using CBST. Inverse ST is then applied for each of these bands. This operation results in a new set of band-limited sub-series. Then, ANN is used on each of these sub-series for forecasting.

For illustration, wind speed data in Case-2, have been decomposed into four equal frequency bands, using CBST, which are shown in Figure 4.1.

The following subsections explain the various steps involved in the wind speed prediction at timestamp $N + 1$, of a time series of length N .

4.1 PADDING AND SIGNAL DECOMPOSITION USING CBST

The steps involved in the frequency-based decomposition of the wind speed data are enumerated as follows:

1. The wind speed data used for forecasting is a finite time series. This leads to border distortion, which appears at the boundaries (onset and end) of the time-

frequency distribution of the time series. These artifacts affect the forecasting results.

In order to reduce this distortion we have used the following padding technique to extend the time series. A padding of size $M < N$ is chosen, such that it is neither too big nor too small. Large value of M increases computational cost and also possibly causes extreme distortion. Unwanted spectral components appear at the border for very small value of M . The value of $M = 20$ is chosen in this context.

For a wind speed time series $w(n), n = 1, 2, \dots, N$, create a time series $\tilde{w}(n)$ by padding $w(n)$ using symmetric extension as follows:

$$\tilde{w} = \{w(M), w(M-1), w(M-2) \dots, w(2), w(1), w(1), w(2), \dots, w(N-1), w(N), w(N), w(N-1), w(N-2), \dots, w(N-M+1)\} \quad (4.1.1)$$

2. Obtain the CBST of $\tilde{w}(n)$.
3. Divide the result in Step 2, into F number of frequency bands. Prediction error can be reduced by selecting an appropriate value of F . Figure 4.7 plots the forecasting errors for different values of F . For high prediction accuracy, $F = 12$ is selected.
4. Create F number of zero-matrices of same size as that of the CBST matrix obtained above.
5. Replace the elements in the zero matrix with corresponding elements of the frequency band. The remaining elements of the matrix are left unchanged.
6. Apply inverse ST to each of these frequency bands to obtain F number of sub-series $\tilde{w}_s(t)$, where $s = 1, 2 \dots F$.
7. Each of these sub-series is of length $N + 2M$. Discard the first M and the last M values in each of the sub-series to obtain the sub-series $w_s(t)$ of length N , for further processing.

For illustration, we have shown in Figure 4.2(b), the CBST of $\tilde{x}_3(n), n = (M+1), (M+2) \dots (M+N)$, which is in the original support of $x_3(n)$, i.e., after discarding the padding part of the signal $\tilde{x}_3(n)$. One can observe in Figure 4.2 that, in case of zero padding, the amplitude spectrum at the border is distorted whereas, it is intact if padding scheme given by Eq. (4.1.1) is applied to the time-series.

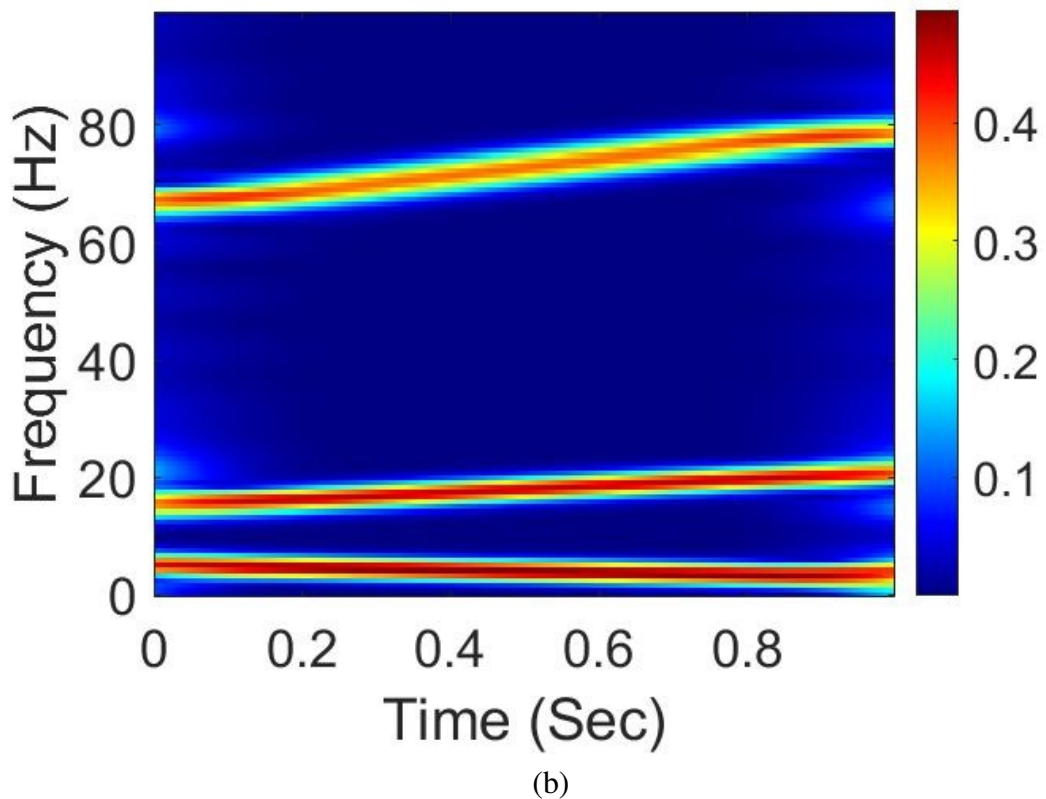
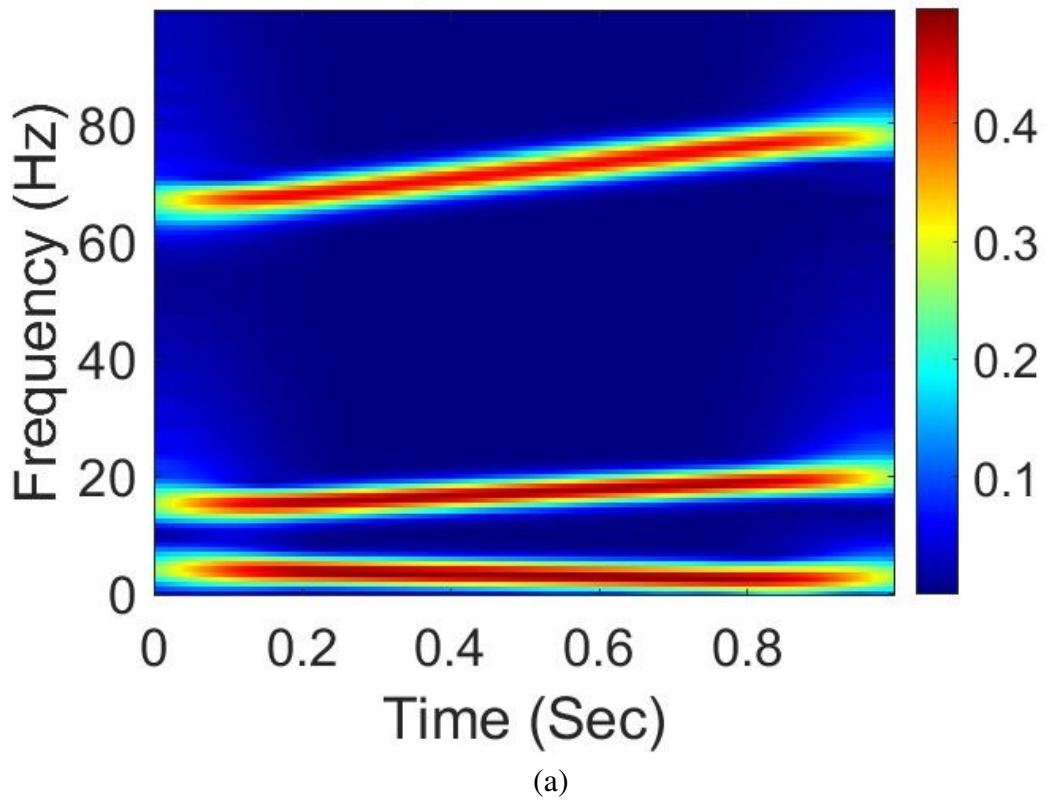


Figure 4.2 Padding effect at the border in the time-frequency distribution of the signal $x_3(n)$. (a) CBST with zero padding (b) CBST with padding shown in Eq. (4.1.1).

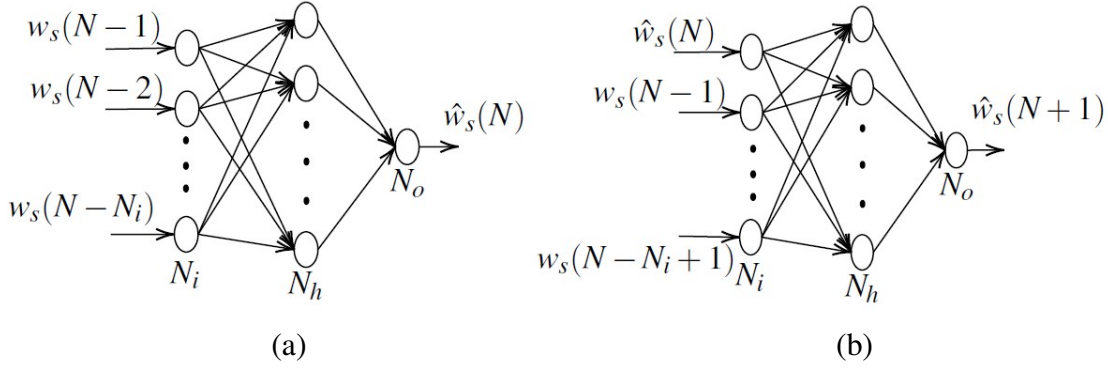


Figure 4.3 Structure of the ANN used for estimating (a) N^{th} sample (b) $(N+1)^{th}$ sample

4.2 FORECASTING USING ANN

A non-linear autoregressive neural network model with LM algorithm is applied on the decomposed sub-series, for forecasting (Nazaré et al., 2019).

To build a forecasting model using ANN for each of the sub-series w_s , the samples $1 \dots (N-1)$ are utilized for predicting N^{th} sample as shown in Figure 4.3(a). It is to be noted that the N^{th} sample is already available in the original time series. However, the padding results in some small amount of distortion in the value of N^{th} sample. A closed-loop network is simulated using the same ANN to predict the $(N+1)^{th}$ sample of the sub-series. This is shown in Figure 4.3(b). We have selected five input nodes (N_i) and fifteen nodes (N_h) in the hidden layer, for our experiment.

The forecast results are recombined to obtain the predicted wind speed data $\hat{w}(N+1)$ as follows:

$$\hat{w}(N+1) = \sum_{s=1}^F \hat{w}_s(N+1) \quad (4.2.1)$$

where, $\hat{w}(N+1)$ is the predicted wind speed at $(N+1)^{th}$ sample, and s represents the number of sub-series.

Algorithm 2 shows the steps involved in the implementation of wind speed forecasting. Figure 4.4 shows a simplified block diagram for wind speed prediction using CBST-ANN.

Algorithm 2 Algorithm for one-step short-term wind speed prediction using the proposed CBST-ANN method

Input: Wind speed data(w) with N samples, Number of input node N_i ,
Hidden layer nodes N_h , Frequency bands F , Padding size M

Output: Predicted wind speed \hat{w} at $(N + 1)^{th}$ sample

- 1: Compute $\tilde{w}(n)$ (use Eq. (4.1.1))
 - 2: $\tilde{W} \leftarrow CBST(\tilde{w})$ (use Eq. (3.3))
 - 3: K = total rows in \tilde{W}
 - 4: N_t = total columns in \tilde{W}
 - 5: $blockSize \leftarrow K/F$
 - 6: **for** $s = 1, 2, \dots, F$
 - 7: $\tilde{W}_s = ZeroMatrix[K][N_t]$
 - 8: $j \leftarrow i + blockSize - 1$
 - 9: **for** $k = i, (i + 1), \dots, j$
 - 10: **for** $l = 1, 2, \dots, N_t$
 - 11: $\tilde{W}_s[k][l] \leftarrow \tilde{W}[k][l]$
 - 12: **end for**
 - 13: **end for**
 - 14: $i \leftarrow j + 1$
 - 15: $\tilde{w}_s \leftarrow InverseST(\tilde{W}_s)$ (use Eq. (1.5.8))
 - 16: **for** $a = 1, 2, \dots, N$
 - 17: $w_s(a) \leftarrow \tilde{w}_s(a + M)$
 - 18: **end for**
 - 19: $\hat{w}_s(N) \leftarrow predict(w_s(N - N_i), \dots, w_s(N - 1))$
 - 20: $\hat{w}_s(N + 1) \leftarrow predict(w_s(N - N_i + 1), \dots, w_s(N - 1), \hat{w}(N))$
 - 21: **end for**
 - 22: $\hat{w}(N + 1) \leftarrow \sum_{s=1}^F \hat{w}_s(N + 1)$
-

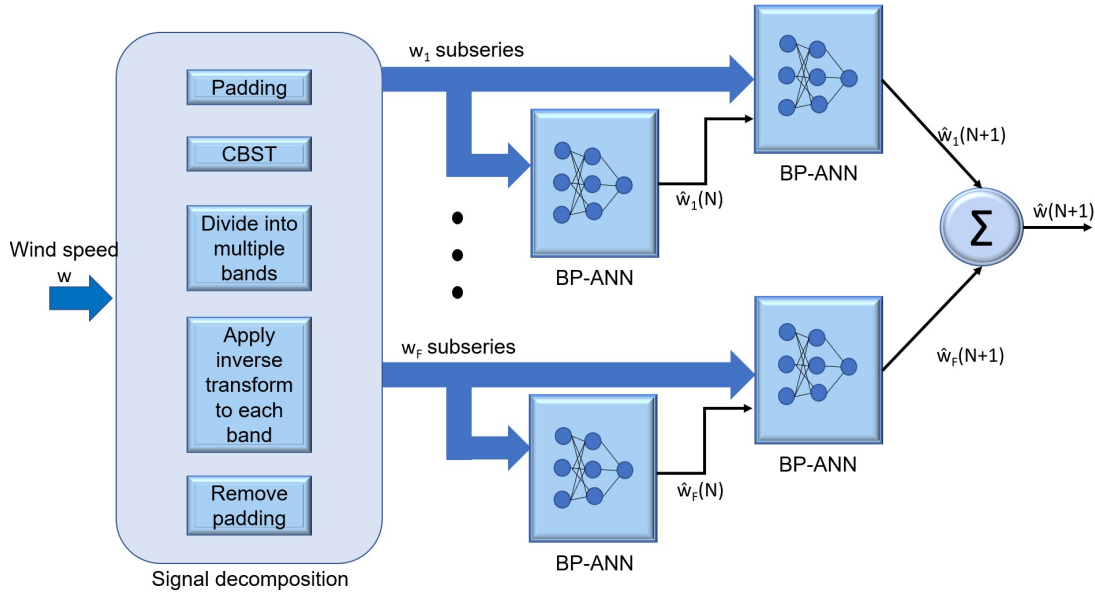


Figure 4.4 Block diagram depicting the proposed CBST-ANN method for short-term forecasting of wind speed w

4.3 EXPERIMENTAL RESULTS

The proposed hybrid CBST-ANN model is compared with some other popular methods, which involve variations of discrete wavelet transforms (DWT) or EMD.

The wavelet based forecasting methods utilize MODWT. MODWT has the advantage that, it can be used to decompose time-series of any sample size, whereas in DWT, the size is limited to 2^j , where j is a positive integer. Also, the resultant approximate and detail coefficients of the time-series are of the same length as the original series, in case of MODWT. Decomposition of wind speed data based on MODWT is carried out by many researchers for wind speed prediction (Kiplangat et al., 2016; Doucoure et al., 2016; Li and Liao, 2018; Singh et al., 2019). In the MOWDT-ANN method, ANN algorithm is used on the transformed coefficients for forecasting. Inverse MODWT is then applied to the predicted values to obtain the final prediction results.

SSA has been used by many researchers for denoising the high frequency sub-series. Decomposition involving wavelet transform with SSA (Yu et al., 2017b) is used to compare the forecasting results of different methods.

Empirical mode decomposition and its variations such as ensemble empirical mode decomposition (EEMD), and complete ensemble empirical mode decomposition with adaptive noise (CEEMDAN), are also included for comparisons. In these methods, prediction of the next sample takes place by predicting the values in the IMFs and the residue. SSA in combination with EEMD is also seen to give low prediction error for wind speed forecasting (Yu et al., 2017a). Thus for determining the effectiveness of

proposed method for short-term wind speed forecasting, aforementioned methods that involve EMD have been used for comparison.

4.3.1 Parameters for evaluation

Mean absolute percentage error (MAPE), mean square error (MSE), and mean average error (MAE) have been used to compare the performance of various methods.

MAPE (Fard and Akbari-Zadeh, 2014) is defined as :

$$MAPE = \frac{1}{N} \sum_{k=1}^N \frac{|\bar{x}_k - x_k|}{x_k} \times 100, \quad (4.3.1)$$

where, \bar{x}_k and x_k are the predicted and actual values of the k^{th} data point and, N is the number of predicted data points in the time series.

MSE (Doucoure et al., 2016) and MAE (Marugán et al., 2018) are defined respectively as:

$$MSE = \frac{1}{N} \sum_{k=1}^N |\bar{x}_k - x_k|^2, \quad (4.3.2)$$

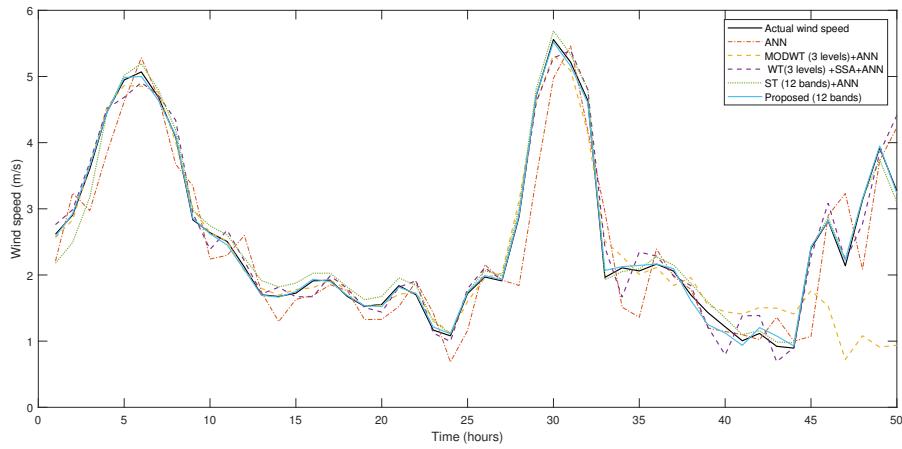
$$MAE = \frac{1}{N} \sum_{k=1}^N |\bar{x}_k - x_k|, \quad (4.3.3)$$

Smaller values of the above error measures are desirable for good forecasting results.

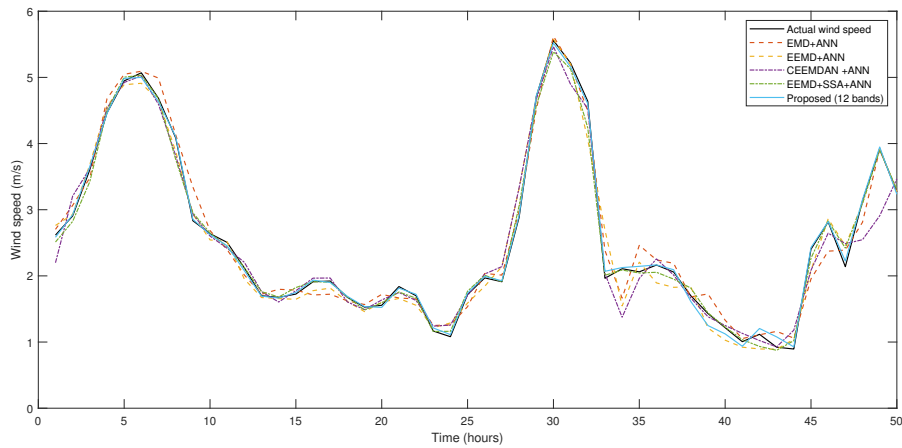
Three wind speed datasets, of various regions of India, are considered for the evaluation of wind speed prediction. For a better analysis of the proposed CBST-ANN method, we have considered simulated wind speed data as well as data recorded using anemometer and LiDAR instrument at different heights.

4.3.2 Case 1: Prediction using simulation data

The simulated wind speed data using nonhydrostatic mesoscale model is obtained from the website www.meteoblue.com. We have used hourly simulated wind speed data from the coastal region of Mangalore, India. The first 250 samples are used for training and the next 50 are for testing. Figure 4.5 shows the forecasting of wind speed for the given data using various algorithms. The preliminary results show that decomposing the data using CBST yields low prediction error. Table 4.1 compares the parameters



(a)

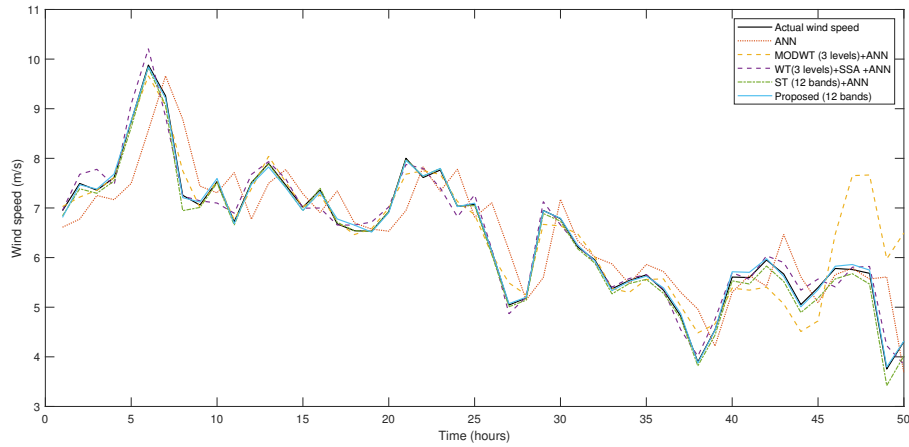


(b)

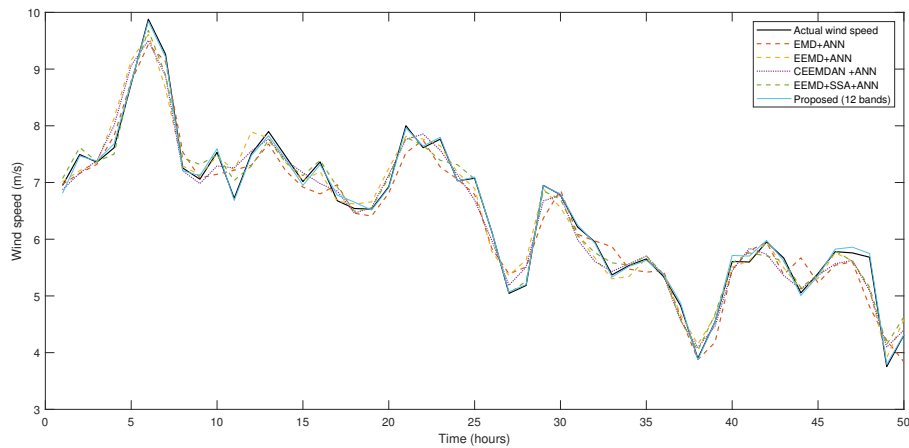
Figure 4.5 Case 1: Hourly wind speed data forecasting. Proposed CBST-ANN method compared with (a) variations of DWT and ANN, (b) variations of EMD

Table 4.1 MAPE, MSE, and MAE values for short-term (one-hour) prediction of wind speed (Case 1).

Method	MAPE (%)	MSE ($(m/s)^2$)	MAE (m/s)
ANN	16.9627	0.2704	0.3955
MODWT-ANN (3 level)	15.1590	0.4965	0.3483
WT-SSA-NN(3 level)	8.5715	0.0641	0.1779
EMD-ANN	7.6565	0.0424	0.1578
EEMD-ANN	7.5215	0.0461	0.1508
CEEMDAN-ANN	7.0056	0.0636	0.1611
EEMD-SSA-ANN	3.4419	0.0131	0.0784
ST-ANN (12 bands)	5.6779	0.0231	0.1229
CBST -ANN (12 bands)	2.3528	0.0030	0.0412



(a)



(b)

Figure 4.6 Case 2: Hourly wind speed data forecasting. Proposed CBST-ANN method compared with (a) variations of DWT and ANN, (b) variations of EMD

MAPE, MSE, and MAE for various methods.

4.3.3 Case 2: Wind speed recorded at 100m height

In Case 2, we have used the wind speed data collected at 100m height for every 10 minutes (Bharani and Sivaprakasam, 2019) from Tamil Nadu, India. Hourly data is obtained using down-sampling by averaging the ten-minute data (Blanchard and Samanta, 2020). The first 300 samples are used for training and the next 50 are for testing. Figure 4.6 shows the results of one-step prediction using different methods. Table 4.2 demonstrates MAPE, MSE, and MAE.

We also observe that, for wind speed time series, the error in prediction depends on the number of sub-series that are obtained using frequency-based decomposition.

Table 4.2 MAPE, MSE, and MAE values for short-term (one-hour) prediction of wind speed (Case 2).

Method	MAPE (%)	MSE ($(m/s)^2$)	MAE (m/s)
ANN	9.6947	0.5773	0.5872
MODWT-ANN (3 level)	6.2098	0.3966	0.3309
WT-SSA-ANN (3 level)	2.7548	0.0463	0.1778
EMD-ANN	5.8522	0.1951	0.3555
EEMD-ANN	3.0987	0.0567	0.1898
CEEMDAN-ANN	3.3839	0.0676	0.2088
EEMD-SSA-ANN	2.4906	0.0396	0.1542
ST-ANN (12 bands)	1.5459	0.0142	0.0887
CBST -ANN (12 bands)	0.7601	0.0038	0.0486

For data considered in Case 2, the prediction errors are plotted against the number of frequency bands used. This result is shown in Figure 4.7. It can be observed that, the prediction errors decreases on increasing the number of frequency bands up to around 15, after that it stabilizes to almost a constant. We have fixed the number of frequency bands used for the prediction of wind speed to 12.

4.3.4 Case 3: Coastal wind speed forecasting

Offshore wind farms offer several advantages. Unlike onshore winds, the offshore winds are stronger and more consistent. Potential locations for such wind farms along the Indian coast was explored by Murali et al. (2014). They identified three regions along the west coast of the Indian subcontinent. National Institute of Wind Energy (NIWE) set up LiDAR instruments in the Gulf of Khambat, Gujarat, India for the assessment of the feasibility of offshore wind farms.

The wind speed is recorded from LiDAR at different heights. For prediction, wind speed at heights 80m, 100m, 120m and 200m have been considered. For the LiDAR dataset, the first 110 samples have been used for training and the next 30 are tested. The prediction results are shown in Figure 4.9. Table 4.4 tabulates the error parameters of the prediction results.

Apart from the data from LiDAR, the wind speed has also been recorded every 10 minutes from a coastal wind mast at the height of 100m using anemometer. The hourly data using down-sampling have been obtained by averaging the ten-minute data. These data are available at www.niwe.res.in. Wind speed data of size 300 are used for training and 50 samples are used for testing. The forecast results are shown graphically

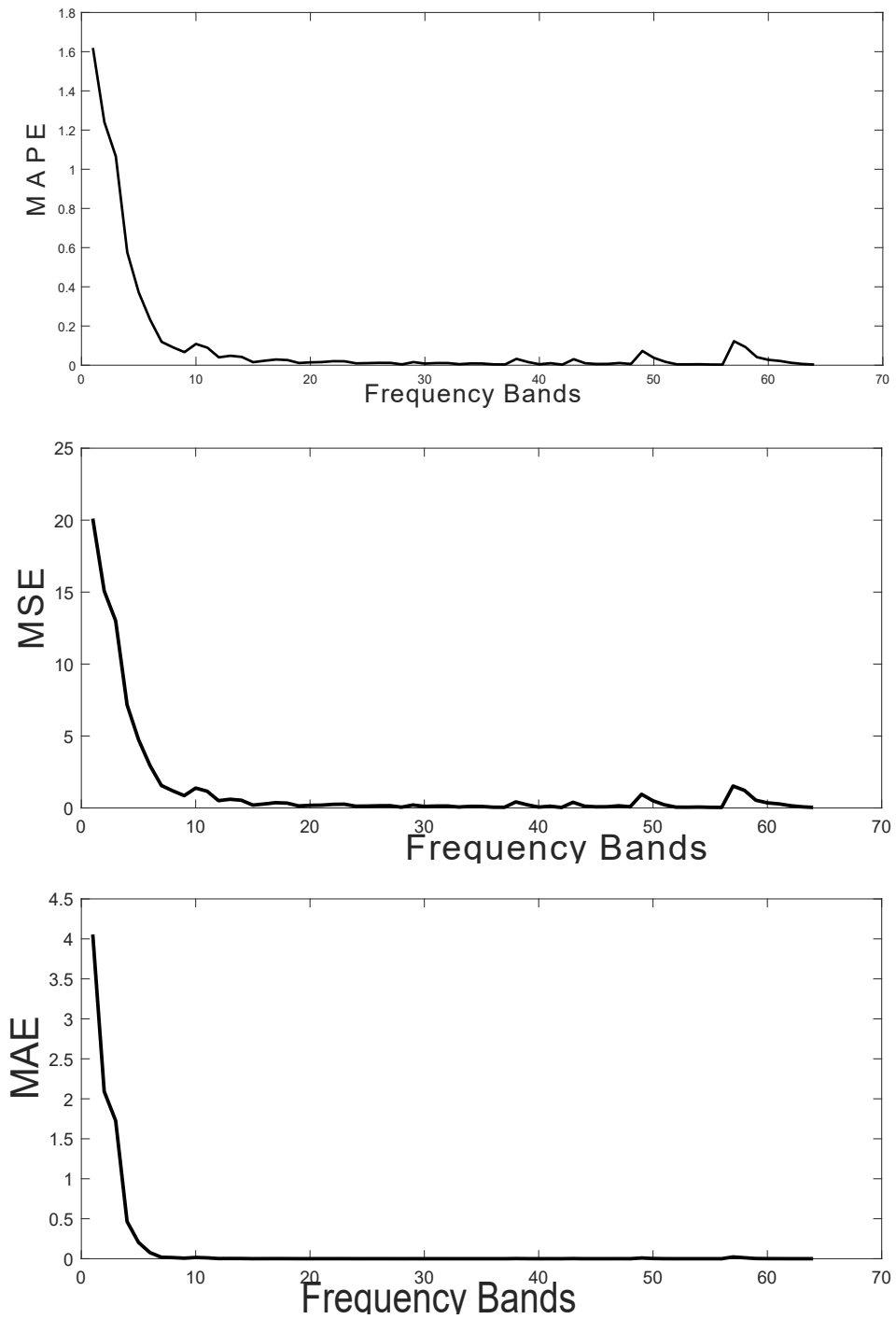
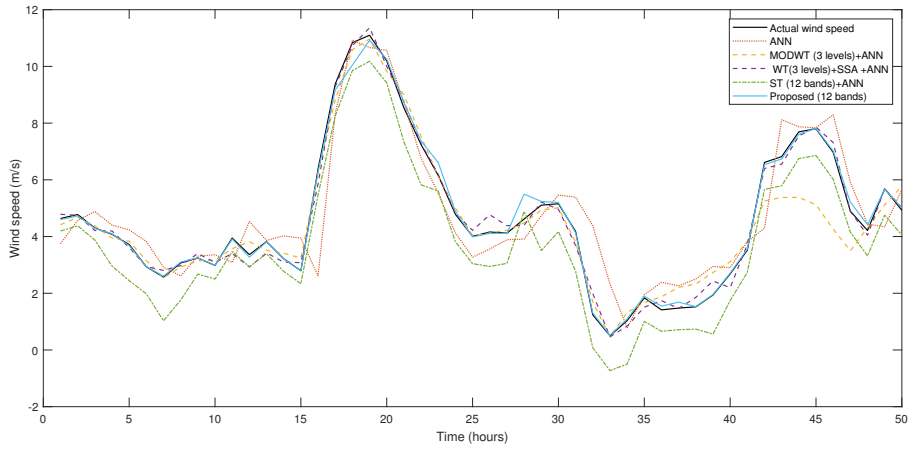
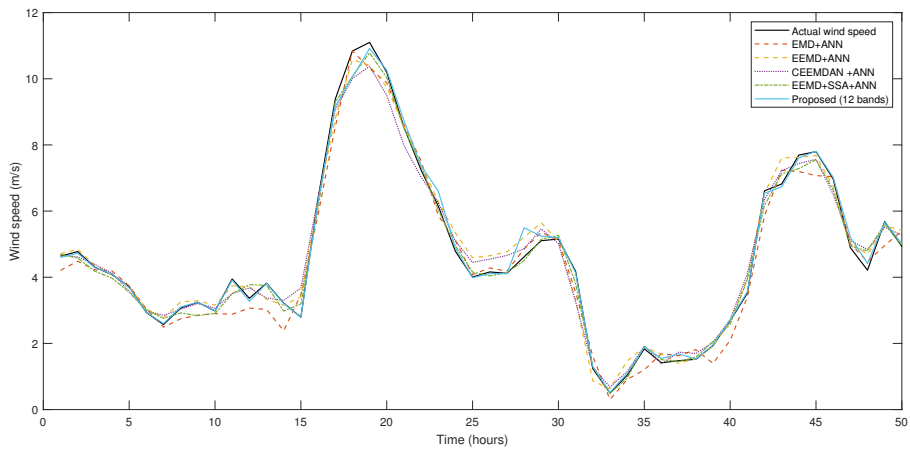


Figure 4.7 Effect of increasing frequency bands on prediction error. (a) MAPE (b) MSE (c) MAE



(a)



(b)

Figure 4.8 Case 3: Hourly wind speed data forecasting onshore at Jafarabad, Gujrat, India. Proposed CBST-ANN method compared with (a) variations of DWT and ANN (b) variations of EMD

Table 4.3 MAPE, MSE, and MAE values for short-term (one-hour) prediction of wind speed recorded from 100m mast (Case 3).

Method	MAPE (%)	MSE $((m/s)^2)$	MAE (m/s)
ANN	30.2043	1.1200	0.7716
MODWT-ANN (3 level)	12.5030	0.6273	0.4879
WT-SSA-ANN (3 level)	7.4757	0.0787	0.2197
EMD-ANN	10.3696	0.1971	0.3551
EEMD-ANN	7.8205	0.1971	0.274
CEEMDAN-ANN	7.3848	0.1971	0.2904
EEMD-SSA-ANN	4.6450	0.0635	0.1915
ST-ANN (12 bands)	31.2573	0.9391	0.9101
CBST -ANN (12 bands)	2.5515	0.0411	0.1083

Table 4.4 MAPE, MSE, and MAE values for short-term (one-hour) prediction of wind speed measured using LiDAR.

Height (m)	MAPE (%)	MSE $((m/s)^2)$	MAE (m/s)
80	4.1121	0.0376	0.1370
100	3.4804	0.024	0.1194
120	3.5112	0.0272	0.1180
200	4.7179	0.0490	0.1678

in Figure 4.8, and the error parameters are tabulated in Table 4.3.

4.4 CONCLUSION

In this chapter, we have proposed a hybrid time series forecasting model involving CBST and ANN. The model decomposes the wind speed data into different sub-series. ANN algorithm, for one step prediction is applied to each sub-series. The number of input nodes and size of the hidden layer are kept constant for one-step prediction. Decomposing the wind speed time-series based on frequency, reduces the error in forecasting. This procedure is followed for prediction of wind speed using ST and CBST. In both ST and CBST based methods, lower prediction errors are observed in comparison to the methods which involved different versions of EMD and DWT. However, we observe that CBST offers the least prediction error for short-term (hour-ahead) forecasting of wind speed. In the future, we plan to attempt a more detailed study to determine the ideal size of the input nodes and the hidden layer for all the sub-series. In addition to this, by considering the other features of the sub-series, we plan to improve the prediction error.

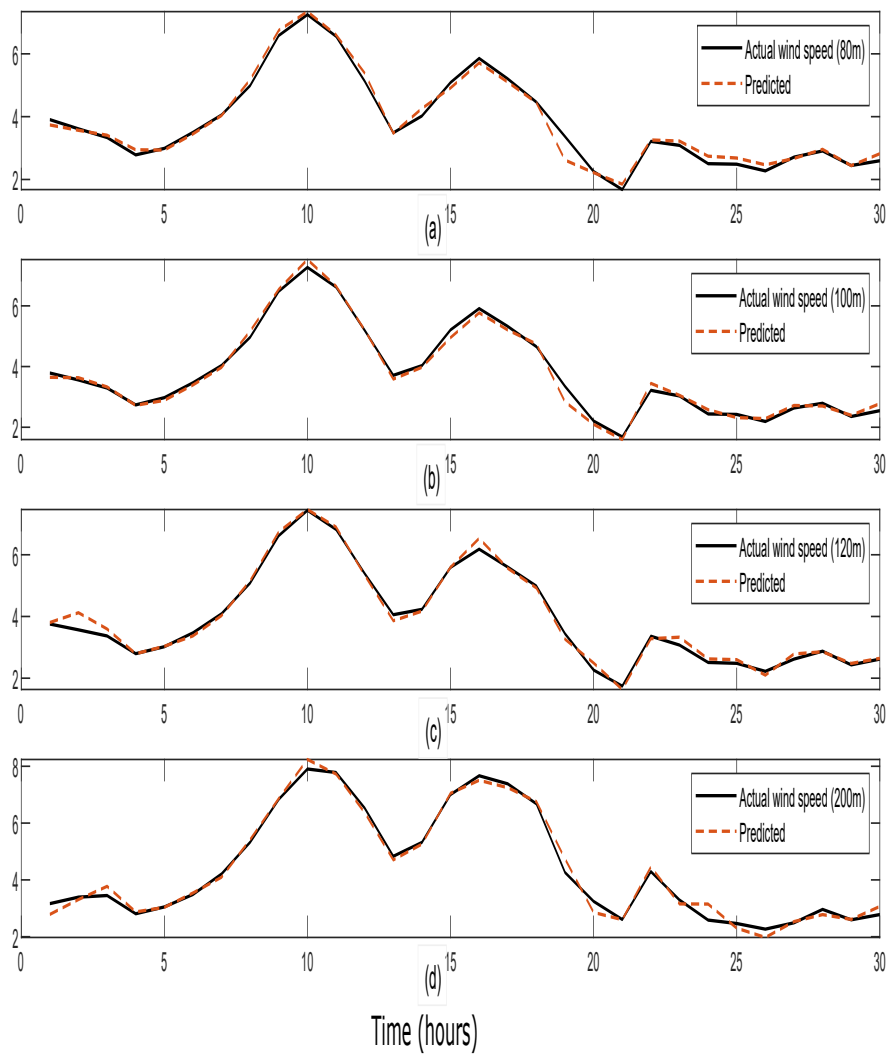


Figure 4.9 Case 3: Hourly wind speed LiDAR data forecasting using proposed CBST-ANN method at various height, (a) 80m (b) 100m (c) 120m (d) 200m

CHAPTER 5

DESPECKLING OF SAR IMAGES USING SHOCK FILTERS AND TWO DIMENSIONAL DISCRETE ORTHOGONAL S-TRANSFORM

5.1 INTRODUCTION TO SAR IMAGE DESPECKLING

Synthetic aperture radar (SAR) images provide useful information on various geophysical aspects which comprise of, and not limited to, vegetation, atmospheric information. However, the presence of speckle in the SAR image makes the image interpretation difficult. The speckle in SAR images is data-dependent. During the acquisition of SAR images, surfaces reflect the incident microwave signal. Based on the type and nature of the surface, the scattering of the signal takes place, which causes speckle in the acquired image. Speckle in the homogeneous regions appears granular due to the difference in phases of the backscatter (Dasari et al., 2015).

Various methods are developed to reduce the effect of speckle. For example, increasing the number of looks helps in reducing the amount of speckle. In multi-look schemes, the radar beam is divided into many sub-beams to obtain several *looks* of the same scene. These looks are averaged to reduce the speckle. This is called multi-look processing. The advent of high speed and computationally efficient computers resulted in the employment of other computational techniques for speckle reduction. Such techniques are used either in the spatial or in the transformed domain.

Popular spatial domain methods to despeckle SAR images generally employ modified techniques involving spatial filters (Lee; Frost et al., 1982; Kuan et al., 1985; Lee et al., 2009), and non-local methods (Buades et al., 2005; Jidesh and Balaji, 2018; Zhong et al., 2013). These non-local methods determine the value of the target pix-

els based on their similarity to the other pixels in the image.

SAR image despeckling in the transformed domain involves various popular transformation techniques like wavelet (Parrilli et al., 2012; Chierchia et al., 2017; Singh et al., 2018), curvelet (Li et al., 2011; Swamy and Vani, 2016), and shearlet (Hou et al., 2012; Liu et al., 2017). Most of these methods determine a threshold to modify the values of transformed coefficients. This non-linear thresholding technique is often termed as shrinkage. Shrinkage can be classified broadly as hard and soft thresholding. For a given threshold T , the generalized soft and hard thresholding schemes for a transformed coefficient C are given by Eq. (5.1.1) and (5.1.2) respectively as follows:

$$C_s = \max(0, C - T) \quad (5.1.1)$$

$$C_h = \begin{cases} 0 & \text{if } |C| \leq T, \\ C & \text{otherwise} \end{cases} \quad (5.1.2)$$

Wavelet transform has been successfully used with thresholding schemes for denoising images and speckle reduction in SAR images. Some important wavelet thresholding techniques include RiskShrink (Donoho and Johnstone, 1994), SureShrink (Donoho and Johnstone, 1995), BayesShrink (Chang et al., 2000).

A strategy suggested by Birgé and Massart (1997) can be used to determine the threshold for wavelet transformed SAR image (Aghabalaei et al., 2018), where the threshold depends on the level of the wavelet decomposition. A systematic approach for the aforementioned strategy is explained by Sidhik (2015). In this thresholding scheme for 2-D wavelet transform with d_o decomposition levels, at a level $d \leq d_o$, only K_w largest coefficients are retained. This value of K_w is determined as follows:

$$K_w = \frac{n_w}{(d_o + 1 - d)^p}, \quad (5.1.3)$$

where n_w indicates the number of approximation coefficients in the coarsest level of wavelet decomposition. Based on the application, the value of p is selected in Eq. (5.1.3).

Another time-frequency analysis tool, S-transform (ST), has been used in image despeckling. The two-dimensional ST (2DST) has been used for despeckling SAR images by Gao et al. (2016). Speckle is considered to be a high-frequency component in the SAR image. 2DST is computed for high-frequency components of the image using a sharp cut-off frequency. This is followed by shrinkage of these 2DST coefficients. For faster execution, low-frequency components of the image are left unprocessed. The 2DST coefficients are grouped together in frequency pairs. The threshold

value for shrinkage is primarily determined by finding the distance between frequency pairs, followed by estimating the weighted standard deviation of the speckle. A soft thresholding scheme is employed for shrinkage of the ST coefficients. However, the main disadvantage of this method is that applying 2DST on image results in a four-dimensional structure. This method utilizes large memory and has high computational time complexity.

In contrast to continuous ST, the DOST is an efficient representation of ST. Noise removal in images using shrinkage of DOST coefficients is proposed by Sun et al. (2014) using a soft thresholding scheme to denoise myocardial contrast echocardiography images.

For an $N \times N$ image, 2DST has computational complexity of $O(N^4 \log(N))$ (Drabycz et al., 2009) whereas it is $O(N^2 \log(N))$ in case of 2D-DOST for the same image (Wang and Orchard, 2009). The computational time required for DOST is low, which forms one of the motivating factors to use this in SAR image despeckling. Also, DOST can decompose the given image into multiple smaller groups of coefficients, which are arranged together to obtain *voice-images*. The voice-images can be processed in the two-dimensional domain, whereas ST requires the image to be processed in four dimensions. The memory requirement for storing the transformed image is less when compared to ST.

Since, speckle is predominant in the higher frequency components of SAR images (Gao et al., 2016), it is essential to segregate these components and treat them separately. In the proposed method, Butterworth filter is used on the SAR image to obtain the low and high frequency components. The DOST coefficients of the transformed image are modified using hard thresholding. Inverse DOST follows this step. Shock filter (Alvarez and Mazorra, 1994) is used to remove residual speckle on the low-frequency components before adding it back to the image. Edge preservation using edge detection (Touzi et al., 1988; Dai et al., 2004) is performed to retain the edges. The proposed algorithm is able to offer good quality of "speckle-free" estimate of SAR image with fast execution time. This method can be applied to both single and multi-look images.

The proposed method uses two-dimensional DOST and shock filter for despeckling.

5.1.1 Shock Filter

Shock filters are generally used in image deblurring applications to produce a piecewise smooth image. It is used in the proposed method for creating sharper edges and smooth homogeneous regions. Before using the shock filter, a Gaussian blur is applied to the given image I as follows:

$$G^{(0)} = \sum_{x=0}^{M-1} \sum_{y=0}^{N-1} I(x,y)g(s-x,t-y), \quad (5.1.4)$$

where g is a Gaussian kernel with zero mean. This operation is performed prior to the application of shock filter to reduce the adverse effects due to the sharpening of speckle features. Thereafter, the following iteration scheme is applied to arrive at the desired solution:

$$G^{(n+1)} = G^{(n)} - \delta t \times \text{sign}(\Delta G^{(n)}) |\nabla G^{(n)}|, \quad (5.1.5)$$

where, $\nabla G^{(n)}$ and $\Delta G^{(n)}$ are the gradient and Laplacian of G in the n^{th} iteration respectively and δt is the incremental step size. For an appropriately chosen step size, the scheme (5.1.5) converges. See Osher and Rudin (1990); Weickert (2003) for a detailed discussion and applications of shock filter.

5.2 SAR IMAGE DESPECKLING USING 2D-DOST

Speckles are signal dependent, and therefore often modeled as multiplicative noise. An acquired image I consists of noise free image I_{nf} and noise N , and can be represented in a simplified form as follows:

$$I(x,y) = I_{nf}(x,y)N(x,y) \quad (5.2.1)$$

The speckle in SAR images is generally modeled as data dependent multiplicative noise which follows a gamma distribution (Frost et al., 1982). Therefore, it becomes essential to introduce a variance stabilizing transform. A logarithmic transform is applied on the spatial domain of the SAR image to stabilize the variance (Bartlett, 1947).

While the speckle is observed in the high frequency components of the image, the lower frequency component of the image is processed separately to ensure better results.

The log-transformed image is passed through a filter to separate high (I_{hpf}) and low-frequency (I_{lpf}) image components. Any 2-D filter, for example, a Gaussian or a Butterworth filter is suitable to separate the lower and higher frequencies. We have chosen a two-dimensional, second-order Butterworth filter for the separation task, as it

provides sufficient accuracy. The high-pass Butterworth filter is represented as follows:

$$H(u, v) = \frac{1}{1 + \left(\frac{D_o}{D(u, v)}\right)^{2n}}, \quad (5.2.2)$$

where, $H(u, v)$ is the frequency response of the filter at frequency pair (u, v) , D_o is the cut-off distance, $D(u, v)$ is the Euclidean distance from the origin to (u, v) , and n denotes the filter order.

The low-pass filter $L(u, v)$ can be obtained by subtracting the filter response in Eq. (5.2.2) from unity:

$$L(u, v) = 1 - H(u, v) \quad (5.2.3)$$

The low-pass filter component is then processed using the shock filter as explained in Subsection 5.1.1. The usage of shock filter enables enhancement of the edges and hence compensates for any edge lost during the shrinkage of the high-frequency components of the SAR image. It also helps in attenuating the small variations in the image.

The shrinkage of higher frequency components is performed using DOST. For this, the image is transformed using 2D-DOST as specified in Eq. (2.4.1). Individual voice-images are then considered. Let $S_{voice} = (s_{x,y})_{1 \leq x \leq m, 1 \leq y \leq n}$ be such a voice-image of size $V = m \times n$. For every voice-image, a suitable threshold is selected using the following strategies:

1. For smaller voice-images, the absolute values of the coefficients of the voice-image are considered and the median of these values is used as the threshold T . In the current implementation, the threshold of voice-images with size smaller than 4, is selected by using their median values as:

$$T = \text{median}(\{|s_{x,y}| : 1 \leq x \leq m, 1 \leq y \leq n\}) \quad (5.2.4)$$

2. For voice-images whose sizes are larger than 4, the threshold T , shown in Eq. (5.1.3), is selected. This strategy is inspired by Birgé-Massart thresholding for wavelets (Birgé and Massart, 1997).

In the proposed thresholding strategy, for a voice-image of size V , a value K is chosen as follows:

$$K = \frac{V}{((V_{max})^{\frac{1}{2}} + 1 - (V)^{\frac{1}{2}})^p}, \quad (5.2.5)$$

where V_{max} is the size of the largest voice image and $p \geq 1$. We have selected $p = 2$ for the evaluation of our results.

For $i = (x - 1)n + y, 1 \leq x \leq m, 1 \leq y \leq n$ and $i = 1, 2, 3 \dots V$, we define

$$C_i = s_{x,y}$$

Let $C = \{C_i : i = 1, 2 \dots V\}$, and $d_1 = \max\{|x| : x \in C\}$, $d_2 = \max\{|x| : x \in C - \{d_1\}\} \dots, d_K = \max\{|x| : x \in C - \{d_1, d_2, \dots, d_{K-1}\}\}$.

The threshold T , which is the K^{th} largest (in absolute value) element of the matrix S_{voice} , is defined by

$$T = d_K \tag{5.2.6}$$

After selecting a suitable threshold, only those voice components larger than this threshold value are retained in the voice-image and the rest are discarded as shown in Eq. (5.1.2). A new image in the DOST domain is then reconstructed using these modified voice-images. The inverse DOST (IDOST) is then applied to obtain a new component of the SAR image. The main advantage of this shrinkage is that the texture of the image is well preserved. These steps are outlined in Algorithm 4. The modified high and low-frequency components are combined to get a despeckled image. A debiasing stage is introduced in order to ensure that the introduction of the logarithmic transformation does not add any bias to the resultant despeckled image. This debiasing is done by subtracting the mean from the resultant image before applying the exponential transform to obtain despeckled image I_e . Finally, the edge information is reintroduced into the resultant despeckled image by using the ratio based edge detector explained in Section 5.3.

Algorithm 3 demonstrates the above mentioned basic steps that are involved in the proposed despeckling method of the SAR image.

Algorithm 3 Algorithm for despeckling SAR image using 2D-DOST

Input: Speckled SAR image I

Output: Despeckled SAR image I_o

```
1: procedure 2D-DOST-DESPECKLING
2:    $I' \leftarrow \text{Log}(I)$ 
3:    $I_{lpf} \leftarrow \text{LowPassFilter}(I')$ 
4:    $I_{hpf} \leftarrow \text{HighPassFilter}(I')$ 
5:    $I'_{lpf} \leftarrow \text{ShockFilter}(I_{lpf})$ 
6:    $I'_{hpf} \leftarrow \text{2D-DOST Shrinkage}(I_{hpf})$ 
7:    $I'_a \leftarrow I'_{lpf} + I'_{hpf}$ 
8:    $I'_d \leftarrow \text{Debias}(I'_a)$ 
9:    $I_e \leftarrow \text{Exp}(I'_d)$ 
10:   $I_o \leftarrow \text{ImageEdgeEnhancement}(I_e, I)$ 
```

Algorithm 4 Algorithm for 2D-DOST shrinkage on I_{hpf}

Input: High-frequency component I_{hpf} of speckled image

Output: High-frequency component I'_{hpf}

```
1: procedure 2D-DOSTSHRINKAGE
2:    $I_D = \text{DOST}(I_{hpf})$ 
3:    $S_{\text{voice}}$  = voice images obtained from DOST
4:    $\text{maxVoiceSize}$  = Maximum size of voice image
5:   for  $\forall S_{\text{voice}}$  do
6:      $\text{voiceSize} \leftarrow \text{size}(S_{\text{voice}})$ 
7:     if  $\text{voiceSize} < \text{minimum value}$  then
8:        $T \leftarrow \text{median}(|S_{\text{voice}}|)$ 
9:     else
10:       $K \leftarrow \frac{\text{voiceSize}}{((\text{maxVoiceSize})^{\frac{1}{2}} + 1 - (\text{voiceSize})^{\frac{1}{2}})^p}$ 
11:       $T \leftarrow K^{\text{th}}$  largest value of  $|S_{\text{voice}}|$ 
12:      $T_{\text{logical}} \leftarrow |S_{\text{voice}}| \geq T$ 
13:      $S'_{\text{voice}} \leftarrow S_{\text{voice}} \cdot T_{\text{logical}}$ 
14:   end for
15:   Rearrange all  $S'_{\text{voice}}$  to obtain modified DOST  $I'_D$ 
16:    $I'_{hpf} \leftarrow |\text{IDOST}(I'_D)|$ 
```

Algorithm 5 Algorithm for edge enhancement using ratio based edge detection

Input: Original Speckled Image (I), Despeckled Image (I_e)

Output: Enhanced Image (I_o)

```
1: procedure IMAGEEDGEENHANCEMENT
2:    $I_b = \text{binarize}(I_e)$ 
3:    $I_a = \text{countNeighbours}(I_b)$ 
4:    $m = 1, 2, \dots, 12, d = 1, 2$ 
5:   Find masked averages using all masks
6:   for  $\forall$  masks  $M_m$  and directions  $d$ 
7:     Find  $R_{m,d}(x,y)$  using  $a_1^d(x,y), a_2^d(x,y)$  using Eq. (5.3.8)
8:   end for
9:   Estimate ratio based image  $R'$  using  $R_{m,d}$ 
10:  if at every pixel  $(x,y), R'_{x,y} <$  minimum value then
11:     $I_o(x,y) \leftarrow \alpha I_e(x,y) + (1 - \alpha)I(x,y)$ 
12:  else
13:     $I_o(x,y) \leftarrow I_e(x,y)$ 
```

5.3 EDGE ENHANCEMENT USING RATIO BASED EDGE DETECTION

Image sharpening is done after the despeckling of the image. This involves a post-processing step. It is achieved by first, detecting the edges of the given image. For enhancing the image, Dai et al. (2004) used edge detection technique inspired from (Touzi et al., 1988).

Here, from the despeckled image I_e , a binary map I_b is obtained for a suitably chosen threshold T_b as follows:

$$I_b(x,y) = \begin{cases} 1 & \text{if } I_e(x,y) > T_b, \\ 0 & \text{otherwise} \end{cases} \quad (5.3.1)$$

Further, a matrix I_a can be obtained using the binary map I_b as:

$$I_a(x,y) = \sum_{(x,y) \in N(x,y)} I_b(x,y) \quad (5.3.2)$$

where $N(x,y)$ denotes the immediate neighbourhood of the pixel location (x,y) .

The masks $M_m(x,y)$, $m = 1, 2 \dots 12$ of size 3×3 that are shown in Figure 5.1 are applied over the matrix I_a to obtain a new matrix I_m as:

$$I_m(x,y) = \sum_{l=0}^{M-1} \sum_{k=0}^{N-1} I_b(x,y) M_m(x-k, y-l) \quad (5.3.3)$$

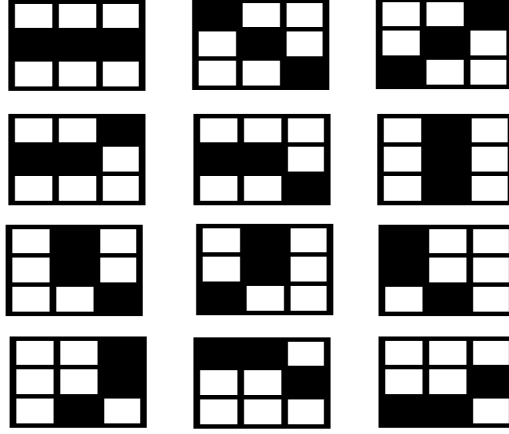


Figure 5.1 Edge directions used for edge detection. Each cell in the 3×3 direction mask consists of a binary value represented here as white (0) and black (1)

Let $d = \{1, 2\}$, then for a location (x, y) , $a_1^d(x, y)$ and $a_2^d(x, y)$ can be defined as:

$$a_1^1(x, y) = I_m(x + 2, y) \quad (5.3.4)$$

$$a_2^1(x, y) = I_m(x - 2, y) \quad (5.3.5)$$

$$a_1^2(x, y) = I_m(x, y + 2) \quad (5.3.6)$$

$$a_2^2(x, y) = I_m(x, y - 2) \quad (5.3.7)$$

The ratio matrix $R_{m,d}$ is computed as

$$R_{m,d}(x, y) = \begin{cases} a_1^d(x, y)/a_2^d(x, y) & \text{if } a_1^d(x, y) \leq a_2^d(x, y) \\ a_2^d(x, y)/a_1^d(x, y) & \text{otherwise} \end{cases} \quad (5.3.8)$$

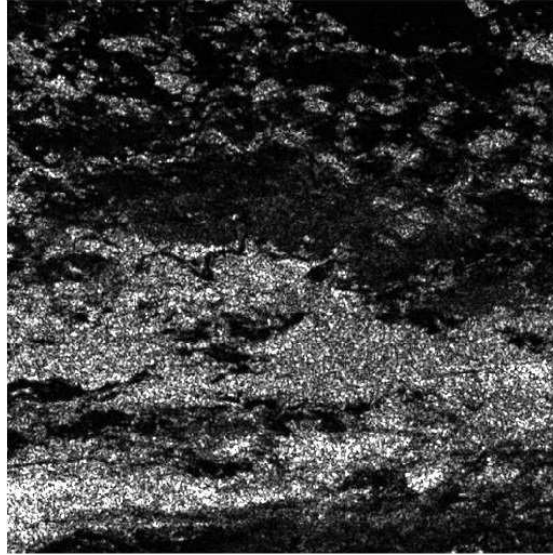
The least value of $R_{m,d}(x, y)$ for a given location (x, y) is selected as the constituent component of final ratio based image R' as follows:

$$R'(x, y) = \min_{\substack{m=1\dots 12 \\ d=1,2}} \{R_{m,d}(x, y)\} \quad (5.3.9)$$

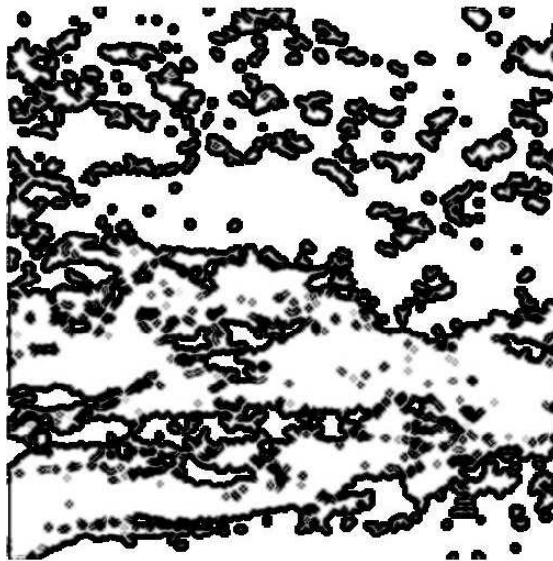
R' obtained from the image shown in Figure 5.2(a) is displayed in Figure 5.2(b), where, the darker shades represent the edges.

Then the edge map E is obtained by comparing R' to a threshold T_{edge} as follows:

$$E(x, y) = \begin{cases} 1 & \text{if } R'(x, y) \leq T_{edge} \\ 0 & \text{otherwise} \end{cases} \quad (5.3.10)$$



(a)



(b)

Figure 5.2 (a) Zoomed-in view of SAR Image shown in Figure 5.4(a), (b) Ratio based image R' obtained by applying the method specified in Section 5.3 on image shown in (a).

A threshold $T_{edge} = 0.5$ is chosen in the implementation of the method. The steps involved in the process of edge enhancement is outlined in Algorithm 5.

To ensure that the edges are not lost in the process of despeckling, at the region where edges are detected, a weighted average replaces the pixel value of the despeckled image using the following map:

$$I_o(x,y) = \begin{cases} \alpha I_e(x,y) + (1 - \alpha)I(x,y) & \text{if } E(x,y) = 1, \\ I_e(x,y) & \text{otherwise} \end{cases} \quad (5.3.11)$$

where, I_e is the despeckled image, I is the original image and α is used to determine the amount of speckled edge that can be allowed in the final image I_o . The value of α is varied from 0 to 1.

5.4 EXPERIMENTS AND RESULTS

Peak signal to noise ratio (PSNR) and structural similarity index (SSIM) are the common statistical measures used for evaluating the performance of various restoration methods. However, ground truth image is required for their evaluation. Since speckle-free ground truth SAR image is not available for evaluation of the performance, we have used an optical image shown in Figure 5.3(a). This image is assumed to be noise and speckle free. Multiplicative gamma distributed noise is introduced to the image. This noisy image is used for analysis of the proposed algorithm for evaluation of PSNR and SSIM. Figure 5.3(c) demonstrates the result of the proposed method on image shown in Figure 5.3(b).

The obtained image is normalized to the range $[0 - 1]$ before calculating PSNR and SSIM. The PSNR is expressed as:

$$PSNR = 10 \log_{10} \left(\frac{1}{MSE} \right), \quad (5.4.1)$$

where, the mean square error (MSE) is given as:

$$MSE = \frac{\sum_{m=1}^M \sum_{n=1}^N (I(m,n) - I_o(m,n))^2}{M \times N} \quad (5.4.2)$$

and I and I_o are the noise-free and the despeckled images respectively.

SSIM measures the amount of similarity between the structures of two images under consideration. The highest value of the similarity index between the two images is equal

Table 5.1 PSNR and SSIM obtained after using various despeckling methods on SAR image shown in Figure 5.3(b)

Methods	PSNR	SSIM
PPB	15.6876	0.9928
MuLog (with BM3D)	24.9163	0.9996
SAR-BM3D	14.3551	0.9898
Wavelet shrinkage	17.6755	0.9956
2DST	19.0215	0.9981
Shearlet	13.6983	0.9880
Proposed	22.8187	0.9995

to 1, and 0 indicates the lowest value. SSIM between two images I and I_o is given by:

$$SSIM = \frac{(2\mu_I\mu_{I_o} + c_1)(2\sigma_{I,I_o} + c_2)}{(\mu_I^2 + \mu_{I_o}^2 + c_1)(\sigma_I^2 + \sigma_{I_o}^2 + c_2)}, \quad (5.4.3)$$

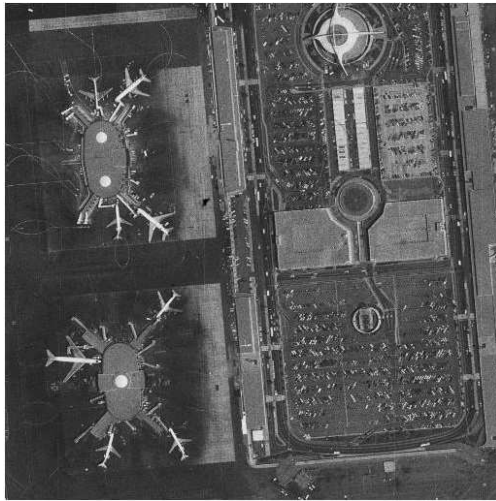
where, c_1 and c_2 are constants, μ_I and μ_{I_o} are mean values and σ_I^2 , $\sigma_{I_o}^2$ are the variances of I and I_o respectively.

Various methods that have been tested and compared for despeckling of images include some well-known methods like 2DST (Gao et al., 2016), shearlet transform (Liu et al., 2017). Further, some other methods which have been tested include SAR-BM3D (Parrilli et al., 2012), wavelet denoising (Birgé and Massart, 1997), probabilistic patch based (PPB) denoising (Deledalle et al., 2009), MuLog (Deledalle et al., 2017). The performance measures MSE, PSNR, SSIM are tabulated for various methods along with the proposed method in Table 5.1 for the synthetically generated noisy image. It can be seen that the proposed method offers promising results while removing speckles from the optical image.

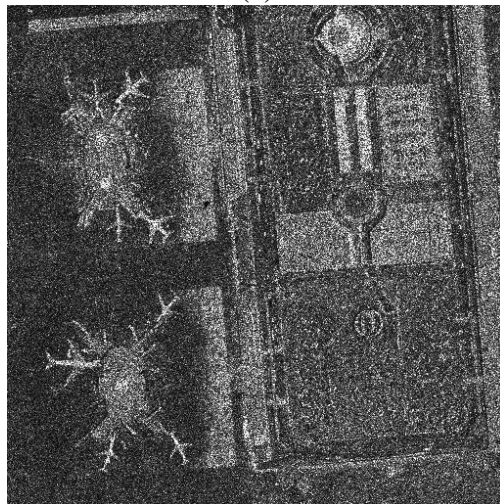
The proposed 2D-DOST method is tested on single-look and multi-look SAR images, including the ones shown in Figure 5.4(a), 5.6(a), and 5.8(a). These images are obtained from Sentinel-1 (single-look, C-Band), AIRSAR (multi-look, C-Band) and TerraSAR-X (multi-look, X-Band) databases for SAR images.

Various other measures which are commonly employed for evaluation of speckle reduction are explained by Argenti et al. (2013). They include equivalent number of looks (ENL), target to clutter ratio (TCR). Edge preservation index (EPI), expectation of ratio image (ERI) (Gao et al., 2016) are the other measurement tools commonly employed for evaluation of SAR despeckling methods. These performance measures are defined in Eq. (5.4.4)-(5.4.7).

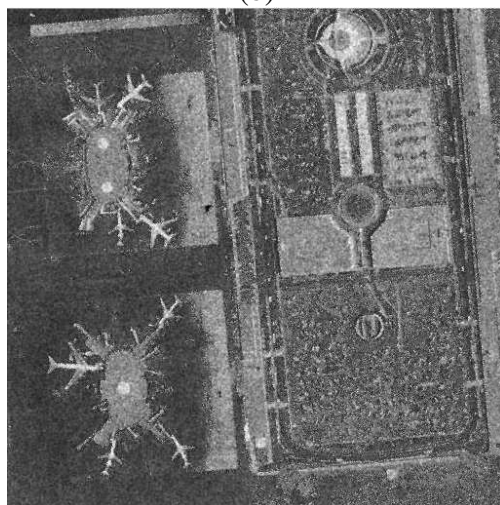
Speckles present in homogeneous regions affect the interpretability of SAR image.



(a)



(b)



(c)

Figure 5.3 (a) A "noise-free" image of airport (b) image corrupted by multiplicative gamma distributed noise and (c) despeckled image using the proposed scheme. Image courtesy: USC-SIPI Image Database

A good despeckling algorithm must be able to suppress the speckles in this region. ENL is used to determine the smoothing performance of the algorithm in a fairly homogeneous region of the SAR image. A high value of ENL indicates low speckle in the region. ENL for a SAR image is calculated as:

$$ENL = \frac{\mu_{I_o}^2}{\sigma_{I_o}^2}, \quad (5.4.4)$$

where, μ_{I_o} and $\sigma_{I_o}^2$ are respectively, mean and variance of the homogeneous part of despeckled image I_o . The ENL values given in Table 5.2 are computed for regions marked in red in Figure 5.4, 5.6, and 5.8

Despeckling algorithms should preserve point targets that are generally identified by strong scatters in the region. TCR is evaluated on a small patch, having strong scatters, on the image. It is used to determine the strength of the scatter with respect to its neighborhood. TCR for a small patch is computed as:

$$TCR = 20 \log_{10} \frac{P_{max}}{\mu_P}, \quad (5.4.5)$$

where, P_{max} is the maximum pixel intensity and μ_P is the mean value of pixel intensities in the patch of interest P in the despeckled image.

The ratio-image is the ratio of individual pixels in the speckled image to that of the despeckled image. ERI measures the expectation of this ratio-image which is given by:

$$ERI = E \left[\frac{I}{I_o} \right] \quad (5.4.6)$$

where E stands for the expectation operator. For an ideal despeckling algorithm, this ratio should be unity.

The operations involved in despeckling of SAR images may cause unwanted loss of edges. hence, in heterogeneous regions of the image, edges must be preserved. EPI is a ratio that measures the quality of the edges in the despeckled image with respect to the speckled image. EPI is defined as

$$EPI = \frac{\sum_{i,j} \sqrt{(I_o(i,j) - I_o(i+1,j))^2 + (I_o(i,j) - I_o(i,j+1))^2}}{\sum_{i,j} \sqrt{(I(i,j) - I(i+1,j))^2 + (I(i,j) - I(i,j+1))^2}}, \quad (5.4.7)$$

Table 5.2 Quantitative Measures for the evaluation of SAR images shown in Figures (5.4,5.6 and 5.8)

Figure	Methods	ERI	TCR	EPI	ENL
Figure 5.4	PPB	0.8995	5.2541	0.0748	97.7558
	MuLog (BM3D)	0.888	5.7452	0.0669	34.5204
	SAR-BM3D	0.8572	5.0494	0.1344	20.6941
	Wavelet shrinkage	0.9446	6.099	0.1405	32.5328
	2DST	1.2825	8.7731	0.5169	158.9057
	Shearlet	1.021	6.7798	0.6046	118.7441
	Proposed	1.1232	5.7233	0.367	72.7418
Figure 5.6	PPB	0.9402	6.2914	0.0766	237.3833
	MuLog (BM3D)	1.2145	9.3561	0.145	62.6279
	SAR-BM3D	0.9895	6.8518	0.2658	76.3608
	Wavelet shrinkage	0.9770	7.5736	0.1785	173.1816
	2DST	1.124	9.3617	0.6461	284.4824
	Shearlet	1.1311	8.9363	0.5551	266.5996
	Proposed	1.02	7.3115	0.3337	157.1365
Figure 5.8	PPB	0.9838	9.0692	0.2601	32.2781
	MuLog (BM3D)	1.0839	10.2648	0.3882	37.2257
	SAR-BM3D	1.0046	9.4586	0.6836	49.1795
	Wavelet shrinkage	1.0272	9.4514	0.5032	46.911
	2DST	1.1241	10.329	0.8269	66.8896
	Shearlet	1.0271	9.6892	0.5611	38.3767
	Proposed	1.0337	8.5999	0.7328	66.6066

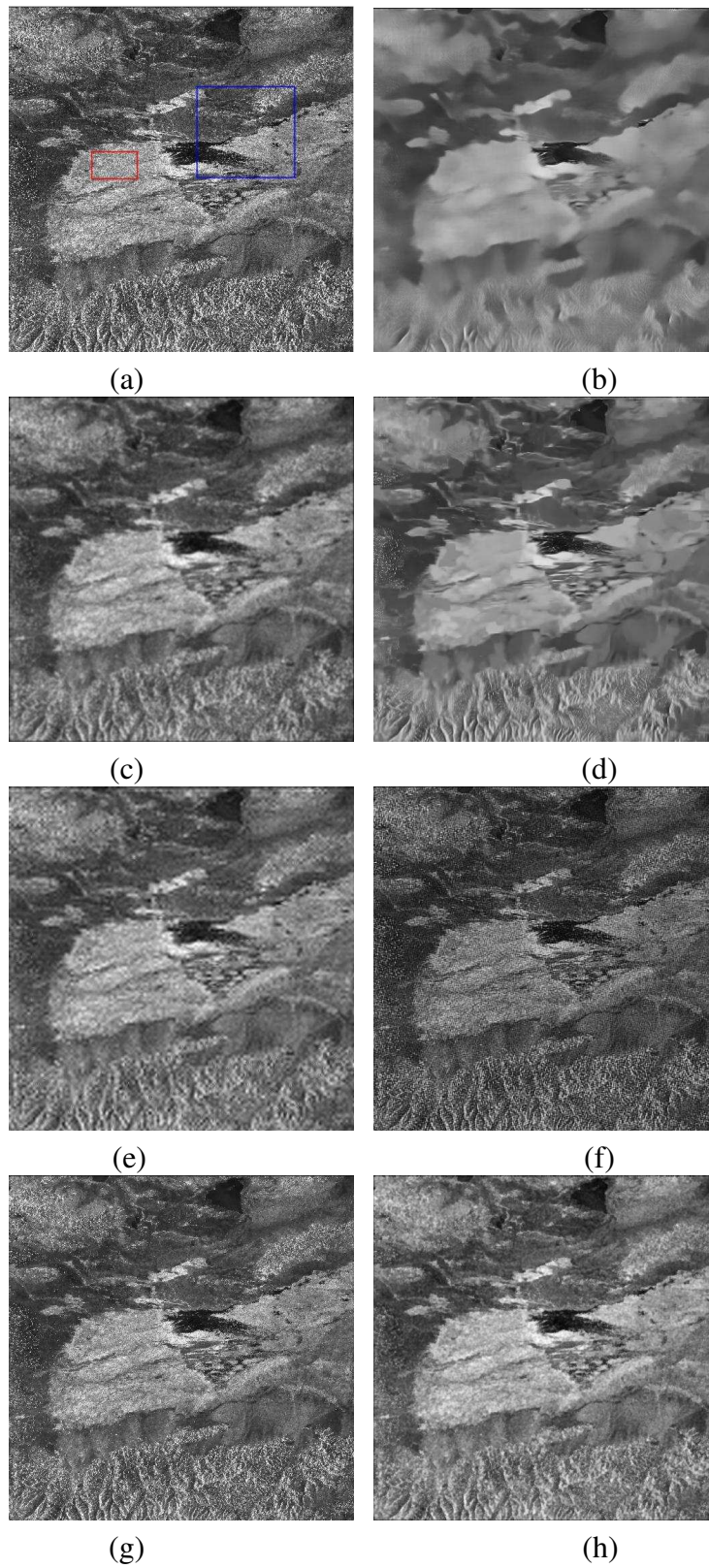


Figure 5.4 Despeckled images of SAR image using various algorithms (a) Original SAR image (b) PPB (c) MuLog (with BM3D) (d) SAR-BM3D (e) Wavelet transform (f) 2DST (g) Shearlet transform (h) Proposed method. Image courtesy: Sentinel-1

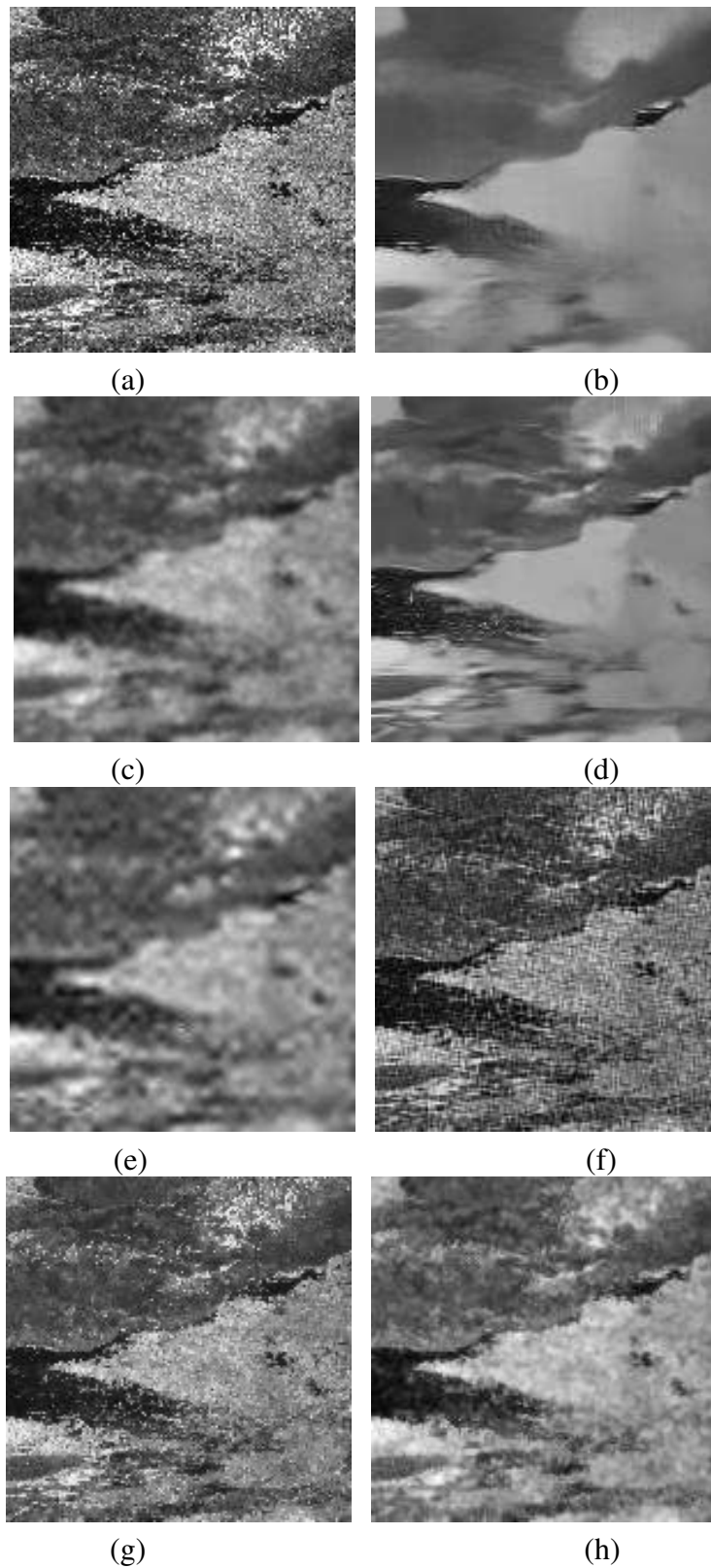


Figure 5.5 Zoomed-in view of the region under blue rectangle shown in Figure 5.4 using various algorithms (a) Original SAR image (b) PPB (c) MuLog (with BM3D) (d) SAR-BM3D (e) Wavelet transform (f) 2DST (g) Shearlet transform (h) Proposed method.

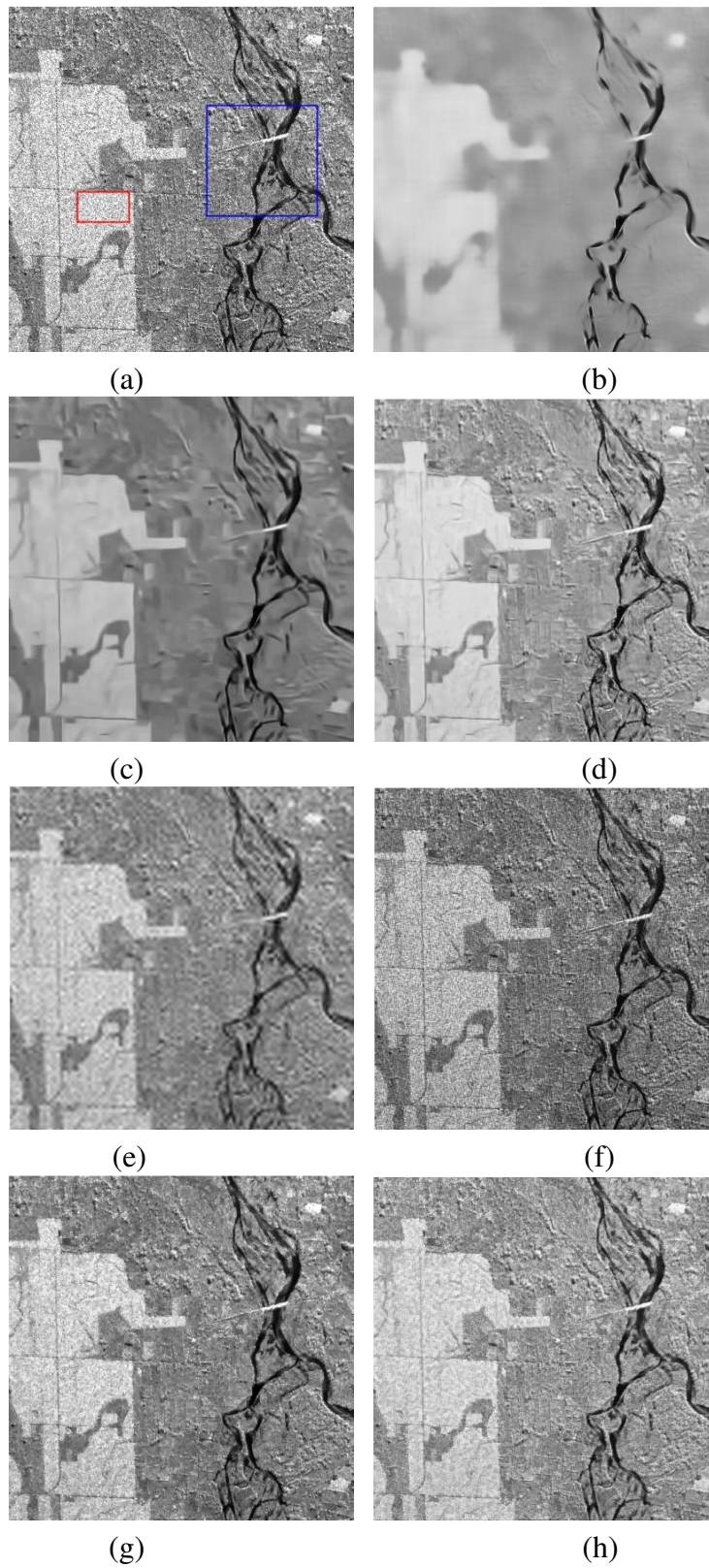


Figure 5.6 Despeckled images of SAR image using various algorithms (a) Original SAR image (b) PPB (c) MuLog (with BM3D) (d) SAR-BM3D (e) Wavelet transform (f) 2DST (g) Shearlet transform (h) Proposed method. Image courtesy: NASA/JPL-Caltech

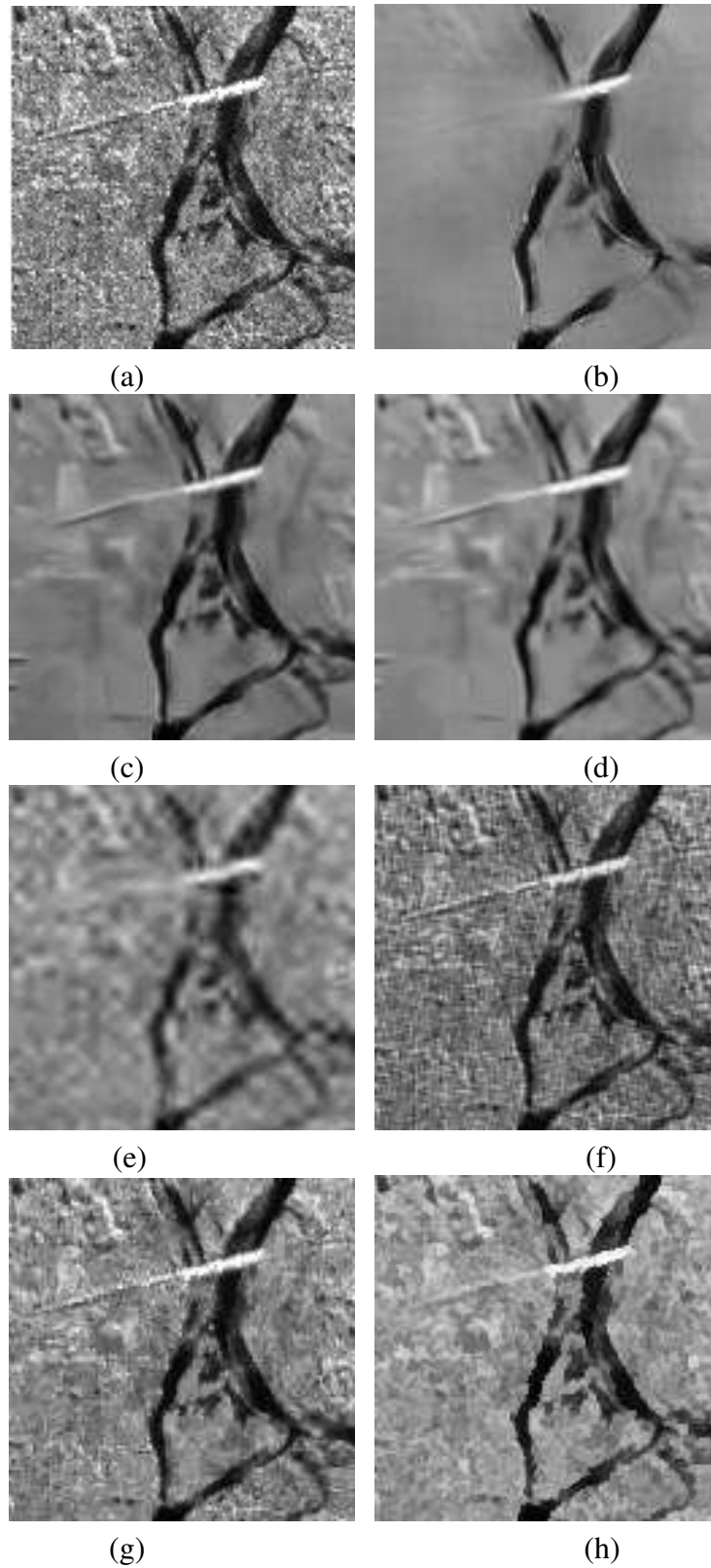


Figure 5.7 Zoomed-in view of the region under blue rectangle shown in Figure 5.6 using various algorithms (a) Original SAR image (b) PPB (c) MuLog (with BM3D) (d) SAR-BM3D (e) Wavelet transform (f) 2DST (g) Shearlet transform (h) Proposed method. Image courtesy: air-sar.jpl.nasa.gov

where, I and I_o are the SAR images before and after despeckling respectively.

Table 5.2 displays the results of the application of these measures on SAR images shown in Figure 5.4(a), 5.6(a), 5.8(a). It can be observed that the proposed method exhibits significantly improved ENL, ERI and EPI values. However, the evaluated TCR is not as high as observed in some other algorithms which have been used for comparison.

On analysing the images shown in Figure 5.4, 5.6, and 5.8, it is found that PPB over-smooths the regions under consideration, which causes loss of information. This is another reason for the low values of quality measures after applying PPB method as shown in Table 5.1. Due to the blurring caused by this method, the EPI values are also very low. These can be observed in Table 5.2.

It is observed in Table 5.1 that the MSE values for the method by Gao et al. (2016) are significantly high compared to the proposed method. This is due to the sharp cut-off in frequency. Thus, the image possess ringing effect on edges. The CPU time, as well as computational costs required, for implementation of this algorithm, is high even for small images. Hence, in order to compare the aforesaid method with the proposed method, we had to decompose the image into smaller blocks which are processed individually before their rearrangement.

The Mulog method performs better in terms of PSNR, as it smooths out the structure and details along with noise, which is not desired in many applications. One can observe in Figure 5.5(c) that the Mulog method is not capable of preserving some of the finer details of the image.

The shearlet transform performs comparatively well but high execution time limits its application in real-time scenarios. Wavelet-based shrinkage methods offer fast execution time. However, based on the type of wavelet used, the despeckled image possesses some artifacts. It is also observed in Table 5.1 that the PSNR, SSIM values are relatively low when compared with the other methods. The proposed algorithm, on the other hand, offers fairly good despeckling results with reduced execution time.

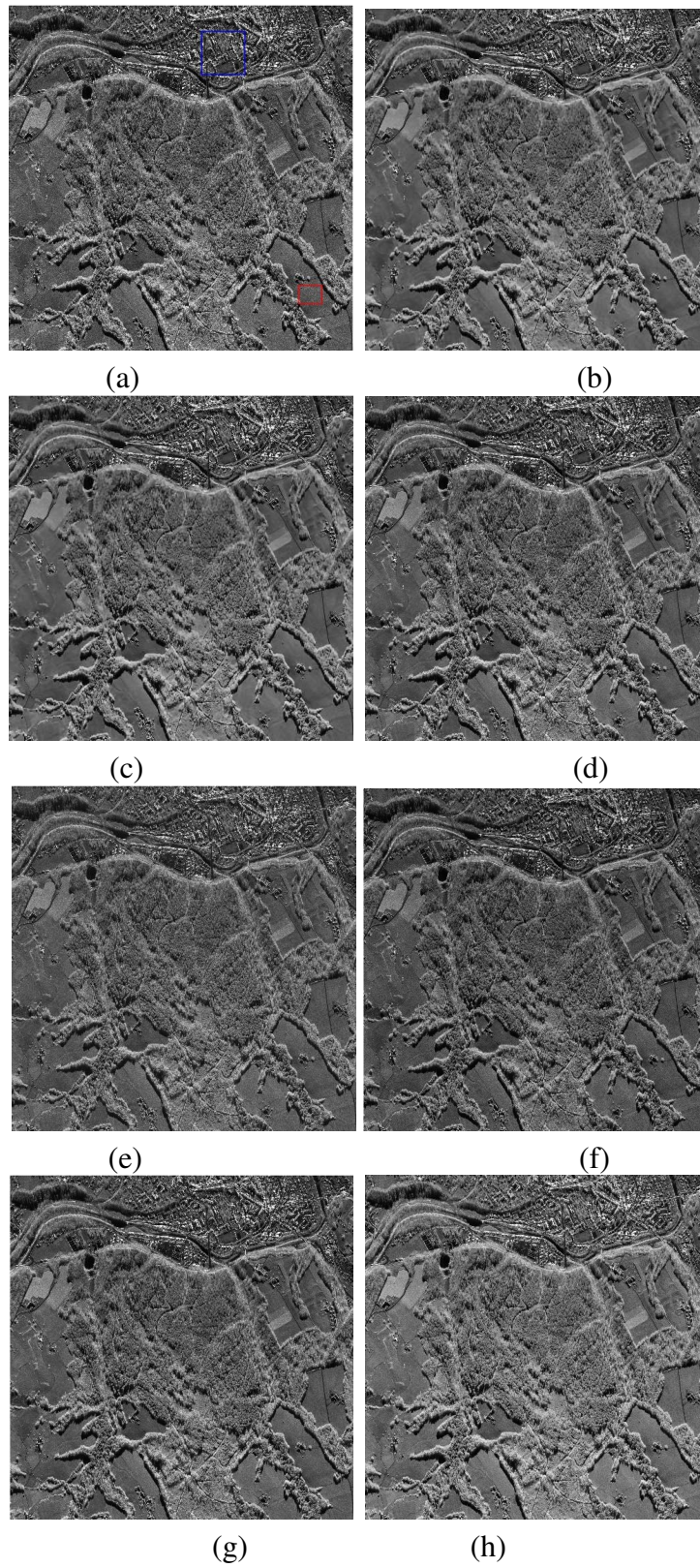


Figure 5.8 Despeckled images of SAR image using various algorithms (a) Original SAR image (b) PPB (c) MuLog (with BM3D) (d) SAR-BM3D (e) Wavelet transform (f) 2DST (g) Shearlet transform (h) Proposed method. Image courtesy: TerraSAR-X

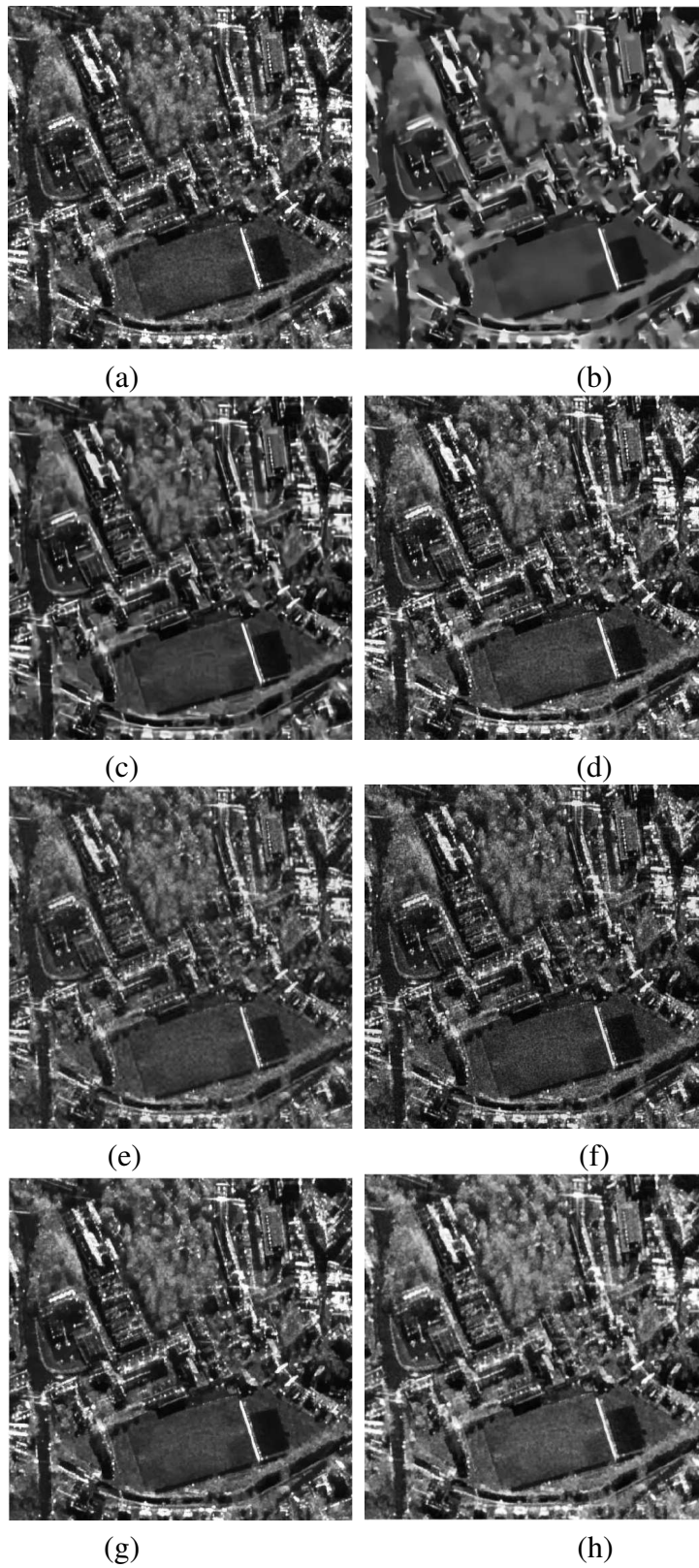


Figure 5.9 Zoomed-in view of the region under blue rectangle shown in Figure 5.8 using various algorithms (a) Original SAR image (b) PPB (c) MuLog (with BM3D) (d) SAR-BM3D (e) Wavelet transform (f) 2DST (g) Shearlet transform (h) Proposed method

Table 5.3 Execution time of SAR images shown in Figure (5.4,5.6 and 5.8) respectively

Methods	Time (in second)		
	Figure 5.4 (512 × 512)	Figure 5.6 (400 × 400)	Figure 5.8 (4096 × 4096)
PPB	26.74	16.21	1740.3
MuLog (BM3D)	17.55	10.43	117.8
SAR-BM3D	61.74	36.78	4207.4
Wavelet shrinkage	0.63	0.07	4.626
2DST	494.51	179.02	29114.5
Shearlet	7.44	4.45	470.2
Proposed	1.69	0.85	85.68

5.4.1 CPU Execution Time

The execution time of various algorithms is important while processing the data in real-time. Many of the algorithms perform well in terms of despeckling. However, the execution time is high for many methods as observed in Table 5.3. For example, Mulog uses gaussian denoisers like BM3D (Deledalle et al., 2017) for despeckling to achieve good results in terms of PSNR as seen in Table 5.1. But the computation time of Mulog (with BM3D) is very high.

SAR images of various sizes are considered for the analysis of execution time. It can be observed in Table 5.3 that despeckling using PPB, SAR-BM3D, Shearlet transform and 2DST are less suitable for real-time processing as their execution demands more time. The time required for the execution of the proposed method is not very high as compared to these methods. The methods like wavelets shrinkage offer a very good execution time compared to the proposed one. However, the proposed method is able to offer higher values of ENL than the wavelet based shrinkage in the homogeneous regions. The EPI values are also higher than the wavelet based shrinkage process.

The implementation of this work is carried out in MATLAB R2019a using a machine having 64-bit Intel Xeon E5-1650 v4 processor, with 3.6 GHz clock speed and 16 GB RAM.

5.5 CONCLUSION

In this chapter, we have proposed a multiresolution despeckling method for SAR images. This method involves shrinkage of 2D-DOST coefficients in the voice images. The proposed model has been compared with some state-of-the-art despeckling models. From the comparison, we can infer that the proposed method can offer a fair trade-off

between execution time and the quality of despeckled SAR images. This is done by preserving the edges and heterogenous regions of the image, and smooth the homogenous regions can be obtained. This has been achieved by using shock filter, DOST-based shrinkage and edge preserving algorithm. When compared to ST, fewer DOST coefficients are required to represent the image. Thus the proposed technique requires less memory compared to ST based technique.

CHAPTER 6

CONCLUSION

Some interesting behaviours of real-world signal can be observed by analysing its frequency. Fourier transform gives the frequency spectra of the signal but fails to provide the temporal information of the frequencies. Many transforms, including S-transform, have been developed to understand the signal behaviour with time.

There are numerous modifications of S-transform in literature. The kernel employed in the conventional S-transform varies with frequency to provide a multi-resolution structure. Many variations attempt to improve the time-frequency resolution of S-transform. One of the variations is discrete orthonormal S-transform, which makes use of orthonormal basis to represent the signal. The usage of orthonormal basis ensures that the transformed coefficients are non-redundant. This is in contrast to the conventional S-transform, where the transformed coefficients are highly redundant as it doubles the dimension of the signal.

Some work has been carried out towards the theoretical development of the S-transform in mathematical literature. S-transform has been explored in Quaternion space, Besov spaces, and Boehmians space. Also the multi-dimensional S-transform has been explored by some of the authors. However, the applications of S-transforms in various areas are still in budding stage, when compared to other time-frequency analysis tools such as wavelet transform.

We used S-transform and its variations in three different applications. In the first application, we used propagation delay based phase difference in conventional S-transform for determining the artifacts due to eye blink in EEG signal. For a signal originating from a particular region, a phase difference due to propagation delay exists between neighbouring electrodes. This phase information was used to determine the eye-blink artifacts in the signal.

This detection technique could be used to identify and remove the artifacts in EMG signals so that the health of muscles and nerve cells can be assessed. We also be-

lieve that this method can be explored further to locate the source of events like localised seizure using EEG. This method could also be instrumental in developing a Brain–Computer Interface (BCI).

We proposed CBST, a modified S-transform to decompose wind-speed data and obtain multiple subseries. Splitting the wind-speed using CBST ensured lower prediction errors. One-step prediction was performed for the subseries using ANN. In both ST and CBST based methods, lower prediction errors were observed in comparison to the methods which involved EMD and DWT and their variations. Also, we observed that CBST offered the least prediction error for short-term (hour-ahead) forecasting of wind speed. With an increase in the number of sub-series required for prediction, the computational cost increases. It is further noticed that low variations in the prediction error occurred when the number of frequency-based sub-series is more than 15. A suitable trade-off between computational cost and error in forecasting is required for determining the optimal number of sub-series. In this work, the number of input nodes and the size of hidden layer in the ANN model were kept constant for all sub-series. It will be interesting to explore the effects on prediction results, by having different node sizes in the hidden layer. We also feel that promising result, in terms of prediction error may be obtained if a deep neural network along with CBST is used.

We also proposed a multiresolution despeckling method for SAR images, based on the shrinkage of the 2D-DOST coefficients in the voice-images. The information contained in the 2D-DOST coefficients was exploited for providing an improved despeckling model. We analysed and compared the proposed model using some other state-of-the-art despeckling models. We infer that the proposed method can offer a fair trade-off between execution time and the quality of the despeckled SAR image. This method can preserve the edges and other details. At the same time, it can smooth out the fairly homogeneous regions of the SAR images. Owing to the orthonormal structure of the basis functions in DOST, and the fact that they are both localised in space and frequency, fewer DOST coefficients are required to represent an image. Therefore, the proposed technique required less memory compared to the ST based technique. Also, in the future, we would like to improve the performance measures associated with despeckling and carry out a hardware implementation of this proposed method.

BIBLIOGRAPHY

- Abed, M. and Belouchrani, A. (2018). Performance analysis and computational cost evaluation of high-resolution time-frequency distributions derived from compact support time-lag kernels. *Digital Signal Processing*, 78:1–19.
- Abed, M., Belouchrani, A., Cheriet, M., and Boashash, B. (2012). Time-frequency distributions based on compact support kernels: properties and performance evaluation. *IEEE Transactions on Signal Processing*, 60(6):2814–2827.
- Aghabalaei, A., Amerian, Y., Ebadi, H., and Maghsoudi, Y. (2018). Speckle noise reduction of time series SAR images based on wavelet transform and Kalman filter. In *IGARSS 2018-2018 IEEE International Geoscience and Remote Sensing Symposium*, pages 625–628. IEEE.
- Akhtar, M. T., Mitsuhashi, W., and James, C. J. (2012). Employing spatially constrained ICA and wavelet denoising, for automatic removal of artifacts from multichannel EEG data. *Signal processing*, 92(2):401–416.
- Alvarez, L. and Mazorra, L. (1994). Signal and image restoration using shock filters and anisotropic diffusion. *SIAM Journal on Numerical Analysis*, 31(2):590–605.
- Argenti, F., Lapini, A., Bianchi, T., and Alparone, L. (2013). A tutorial on speckle reduction in synthetic aperture radar images. *IEEE Geoscience and Remote Sensing Magazine*, 1(3):6–35.
- Assous, S. and Boashash, B. (2012). Evaluation of the modified s -transform for time-frequency synchrony analysis and source localisation. *EURASIP Journal on Advances in Signal Processing*, 2012(49):1.
- Assous, S. and Elkington, P. (2012). Modified S transform for time-frequency analysis of borehole flexural waves dispersion. *The Journal of the Acoustical Society of America*, 131(4):3349–3349.

- Baraniuk, R. G., Flandrin, P., Janssen, A. J., and Michel, O. J. (2001). Measuring time-frequency information content using the rényi entropies. *IEEE Transactions on Information theory*, 47(4):1391–1409.
- Bartlett, M. S. (1947). The use of transformations. *Biometrics*, 3(1):39–52.
- Bharani, R. and Sivaprakasam, A. (2019). A large volume wind data for renewable energy applications. *Data in Brief*, 25:104291.
- Birgé, L. and Massart, P. (1997). From model selection to adaptive estimation. In *Festschrift for lucien le cam*, pages 55–87. Springer.
- Blanchard, T. and Samanta, B. (2020). Wind speed forecasting using neural networks. *Wind Engineering*, 44(1):33–48.
- Boashash, B. (2015). *Time-frequency signal analysis and processing: a comprehensive reference*. Academic Press.
- Buades, A., Coll, B., and Morel, J.-M. (2005). A non-local algorithm for image denoising. In *IEEE Computer Society Conference on Computer Vision and Pattern Recognition, 2005. CVPR 2005.*, volume 2, pages 60–65. IEEE.
- Chang, S. G., Yu, B., and Vetterli, M. (2000). Adaptive wavelet thresholding for image denoising and compression. *IEEE transactions on image processing*, 9(9):1532–1546.
- Chierchia, G., El Gheche, M., Scarpa, G., and Verdoliva, L. (2017). Multitemporal SAR image despeckling based on block-matching and collaborative filtering. *IEEE Transactions on Geoscience and Remote Sensing*, 55(10):5467–5480.
- da Silva, F. H. L. (2006). Event-related neural activities: what about phase? *Progress in brain research*, 159:3–17.
- Dai, M., Peng, C., Chan, A. K., and Loguinov, D. (2004). Bayesian wavelet shrinkage with edge detection for SAR image despeckling. *IEEE Transactions on Geoscience and Remote Sensing*, 42(8):1642–1648.
- Dasari, K., Anjaneyulu, L., Jayasri, P., and Prasad, A. (2015). Importance of speckle filtering in image classification of SAR data. In *2015 International Conference on Microwave, Optical and Communication Engineering (ICMOCE)*, pages 349–352. IEEE.

- Deledalle, C.-A., Denis, L., Tabti, S., and Tupin, F. (2017). Mulog, or how to apply Gaussian denoisers to multi-channel SAR speckle reduction? *IEEE Transactions on Image Processing*, 26(9):4389–4403.
- Deledalle, C.-A., Denis, L., and Tupin, F. (2009). Iterative weighted maximum likelihood denoising with probabilistic patch-based weights. *IEEE Transactions on Image Processing*, 18(12):2661.
- Devuyst, S., Dutoit, T., Ravet, T., Stenuit, P., Kerkhofs, M., and Stanus, E. (2009). Automatic processing of EEG-EOG-EMG artifacts in sleep stage classification. In *13th International Conference on Biomedical Engineering*, pages 146–150. Springer.
- Donoho, D. L. and Johnstone, I. M. (1995). Adapting to unknown smoothness via wavelet shrinkage. *Journal of the american statistical association*, 90(432):1200–1224.
- Donoho, D. L. and Johnstone, J. M. (1994). Ideal spatial adaptation by wavelet shrinkage. *Biometrika*, 81(3):425–455.
- Doucoure, B., Agbossou, K., and Cardenas, A. (2016). Time series prediction using artificial wavelet neural network and multi-resolution analysis: Application to wind speed data. *Renewable Energy*, 92:202–211.
- Drabycz, S., Stockwell, R. G., and Mitchell, J. R. (2009). Image texture characterization using the discrete orthonormal S-transform. *Journal of digital imaging*, 22(6):696–708.
- Fard, A. K. and Akbari-Zadeh, M.-R. (2014). A hybrid method based on wavelet, ANN and ARIMA model for short-term load forecasting. *Journal of Experimental & Theoretical Artificial Intelligence*, 26(2):167–182.
- Frost, V. S., Stiles, J. A., Shanmugan, K. S., and Holtzman, J. C. (1982). A model for radar images and its application to adaptive digital filtering of multiplicative noise. *IEEE Transactions on Pattern Analysis & Machine Intelligence*, PAMI-4(2):157–166.
- Gao, F., Xue, X., Sun, J., Wang, J., and Zhang, Y. (2016). A SAR image despeckling method based on two-dimensional S transform shrinkage. *IEEE Transactions on Geoscience and Remote Sensing*, 54(5):3025–3034.
- George, N. V. (2009). S transform: time frequency analysis & filtering.

- George, N. V., Sahu, S. S., Mansinha, L., Tiampo, K., and Panda, G. (2009). Time localised band filtering using modified S-transform. In *2009 International Conference on Signal Processing Systems*, pages 42–46. IEEE.
- Gibson, P. C., Lamoureux, M. P., and Margrave, G. F. (2006). Letter to the editor: Stockwell and wavelet transforms. *Journal of Fourier Analysis and Applications*, 12(6):713–721.
- Han, Q., Wu, H., Hu, T., and Chu, F. (2018). Short-term wind speed forecasting based on signal decomposing algorithm and hybrid linear/nonlinear models. *Energies*, 11(11):2976.
- Hong, Y.-Y., Yu, T.-H., and Liu, C.-Y. (2013). Hour-ahead wind speed and power forecasting using empirical mode decomposition. *Energies*, 6(12):6137–6152.
- Hou, B., Zhang, X., Bu, X., and Feng, H. (2012). SAR image despeckling based on nonsubsampling shearlet transform. *IEEE Journal of selected topics in applied earth observations and remote sensing*, 5(3):809–823.
- Jidesh, P. and Balaji, B. (2018). Adaptive non-local level-set model for despeckling and deblurring of synthetic aperture radar imagery. *International Journal of Remote Sensing*, 39(20):6540–6556.
- Jung, T.-P., Makeig, S., Humphries, C., Lee, T.-W., Mckeown, M. J., Iragui, V., and Sejnowski, T. J. (2000). Removing electroencephalographic artifacts by blind source separation. *Psychophysiology*, 37(2):163–178.
- Kiplangat, D. C., Asokan, K., and Kumar, K. S. (2016). Improved week-ahead predictions of wind speed using simple linear models with wavelet decomposition. *Renewable Energy*, 93:38–44.
- Krishnaveni, V., Jayaraman, S., Aravind, S., Hariharasudhan, V., and Ramadoss, K. (2006). Automatic identification and removal of ocular artifacts from EEG using wavelet transform. *Measurement science review*, 6(4):45–57.
- Kuan, D. T., Sawchuk, A. A., Strand, T. C., and Chavel, P. (1985). Adaptive noise smoothing filter for images with signal-dependent noise. *IEEE transactions on pattern analysis and machine intelligence*, PAMI-7(2):165–177.
- Lee, J.-S. Digital image enhancement and noise filtering by use of local statistics. *IEEE Transactions on Pattern Analysis & Machine Intelligence*, PAMI-2.

- Lee, J.-S., Wen, J.-H., Ainsworth, T. L., Chen, K.-S., and Chen, A. J. (2009). Improved sigma filter for speckle filtering of SAR imagery. *IEEE Transactions on Geoscience and Remote Sensing*, 47(1):202–213.
- Li, F. and Liao, H.-y. (2018). An intelligent method for wind power forecasting based on integrated power slope events prediction and wind speed forecasting. *IEEE Transactions on Electrical and Electronic Engineering*, 13(8):1099–1105.
- Li, Y., Gong, H., Feng, D., and Zhang, Y. (2011). An adaptive method of speckle reduction and feature enhancement for SAR images based on curvelet transform and particle swarm optimization. *IEEE Transactions on Geoscience and Remote Sensing*, 49(8):3105.
- Liu, H., Chen, C., Tian, H.-q., and Li, Y.-f. (2012). A hybrid model for wind speed prediction using empirical mode decomposition and artificial neural networks. *Renewable Energy*, 48:545–556.
- Liu, H., Tian, H.-q., Pan, D.-f., and Li, Y.-f. (2013). Forecasting models for wind speed using wavelet, wavelet packet, time series and Artificial neural networks. *Applied Energy*, 107:191–208.
- Liu, S., Liu, M., Li, P., Zhao, J., Zhu, Z., and Wang, X. (2017). SAR image denoising via sparse representation in shearlet domain based on continuous cycle spinning. *IEEE Transactions on Geoscience and Remote Sensing*, 55(5):2985–2992.
- Liu, Z., Jiang, P., Zhang, L., and Niu, X. (2020). A combined forecasting model for time series: Application to short-term wind speed forecasting. *Applied Energy*, 259:114137.
- Marugán, A. P., Márquez, F. P. G., Perez, J. M. P., and Ruiz-Hernández, D. (2018). A survey of artificial neural network in wind energy systems. *Applied energy*, 228:1822–1836.
- Mi, X., Liu, H., and Li, Y. (2019). Wind speed prediction model using singular spectrum analysis, empirical mode decomposition and convolutional support vector machine. *Energy conversion and management*, 180:196–205.
- Moukadem, A., Bouguila, Z., Abdeslam, D. O., and Dieterlen, A. (2015). A new optimized Stockwell transform applied on synthetic and real non-stationary signals. *Digital Signal Processing*, 46:226–238.

- Murali, R. M., Vidya, P., Modi, P., and Kumar, S. J. (2014). Site selection for offshore wind farms along the Indian coast.
- Nazaré, G., Castro, R., and Gabriel Filho, L. R. (2019). Wind power forecast using neural networks: Tuning with optimization techniques and error analysis. *Wind Energy*, 23(3).
- Osher, S. and Rudin, L. I. (1990). Feature-oriented image enhancement using shock filters. *SIAM Journal on numerical analysis*, 27(4):919–940.
- Parrilli, S., Poderico, M., Angelino, C. V., and Verdoliva, L. (2012). A nonlocal SAR image denoising algorithm based on LLMMSE wavelet shrinkage. *IEEE Transactions on Geoscience and Remote Sensing*, 50(2):606–616.
- Pinnegar, C. R., Khosravani, H., and Federico, P. (2009). Time frequency phase analysis of ictal EEG recordings with the S-transform. *IEEE Transactions on Biomedical Engineering*, 56(11):2583–2593.
- Pinnegar, C. R. and Mansinha, L. (2003a). The bi-gaussian S-transform. *SIAM Journal on Scientific Computing*, 24(5):1678–1692.
- Pinnegar, C. R. and Mansinha, L. (2003b). The S-transform with windows of arbitrary and varying shape. *Geophysics*, 68(1):381–385.
- Qian, Z., Pei, Y., Zareipour, H., and Chen, N. (2019). A review and discussion of decomposition-based hybrid models for wind energy forecasting applications. *Applied Energy*, 235:939–953.
- Qu, Z., Mao, W., Zhang, K., Zhang, W., and Li, Z. (2019). Multi-step wind speed forecasting based on a hybrid decomposition technique and an improved back-propagation neural network. *Renewable energy*, 133:919–929.
- Radüntz, T., Scouten, J., Hochmuth, O., and Meffert, B. (2015). EEG artifact elimination by extraction of ICA-component features using image processing algorithms. *Journal of neuroscience methods*, 243:84–93.
- Ramasamy, P., Chandel, S., and Yadav, A. K. (2015). Wind speed prediction in the mountainous region of India using an artificial neural network model. *Renewable Energy*, 80:338–347.
- Ramesh Babu, N. and Arulmozhivarman, P. (2013). Improving forecast accuracy of wind speed using wavelet transform and neural networks. *Journal of Electrical Engineering and Technology*, 8(3):559–564.

- Ranjan, R., Singh, A., and Jindal, N. (2018). Formulation of some useful theorems for S-transform. *Optik*, 168:913–919.
- Ren, Y., Suganthan, P., and Srikanth, N. (2014). A comparative study of empirical mode decomposition-based short-term wind speed forecasting methods. *IEEE Transactions on Sustainable Energy*, 6(1):236–244.
- Rojas, G. M., Alvarez, C., Montoya, C. E., de la Iglesia-Vayá, M., Cisternas, J. E., and Gálvez, M. (2018). Study of resting-state functional connectivity networks using EEG electrodes position as seed. *Frontiers in neuroscience*, 12:235.
- Santhosh, M., Venkaiah, C., and Kumar, D. V. (2018). Ensemble empirical mode decomposition based adaptive wavelet neural network method for wind speed prediction. *Energy conversion and management*, 168:482–493.
- Sejdic, E., Djurovic, I., and Jiang, J. (2008). A window width optimized S-transform. *EURASIP Journal on Advances in Signal Processing*, 2008:59.
- Senapati, K. and Routray, A. (2011). Comparison of ICA and WT with S-transform based method for removal of ocular artifact from EEG signals. *Journal of Biomedical Science and Engineering*, 4(05):341.
- Shamshirband, S., Keivani, A., Mohammadi, K., Lee, M., Hamid, S. H. A., and Petkovic, D. (2016). Assessing the proficiency of adaptive neuro-fuzzy system to estimate wind power density: Case study of Aligoodarz, Iran. *Renewable and sustainable energy reviews*, 59:429–435.
- Sidhik, S. (2015). Comparative study of Birge–Massart strategy and unimodal thresholding for image compression using wavelet transform. *Optik-International Journal for Light and Electron Optics*, 126(24):5952–5955.
- Singh, N. and Pradhan, P. M. (2020). S-transform based on optimally concentrated time-limited and band-limited windows. *Journal of Pseudo-Differential Operators and Applications*, 11:565–592.
- Singh, P., Shree, R., and Diwakar, M. (2018). A new SAR image despeckling using correlation based fusion and method noise thresholding. *Journal of King Saud University-Computer and Information Sciences*, 32(10):1216.
- Singh, S., Mohapatra, A., et al. (2019). Repeated wavelet transform based ARIMA model for very short-term wind speed forecasting. *Renewable energy*, 136:758–768.

- Stanković, L. (2001). A measure of some time–frequency distributions concentration. *Signal Processing*, 81(3):621–631.
- Stockwell, R. G. (2007). A basis for efficient representation of the S-transform. *Digital Signal Processing*, 17(1):371–393.
- Stockwell, R. G., Mansinha, L., and Lowe, R. (1996). Localization of the complex spectrum: the S transform. *IEEE transactions on signal processing*, 44(4):998–1001.
- Sun, F.-r., Babyn, P., Luan, Y.-h., Song, S.-l., and Yao, G.-h. (2014). Image denoising using discrete orthonormal S-transform. In *Proceedings of International Conference on Soft Computing Techniques and Engineering Application*, pages 435–442. Springer.
- Swamy, P. S. and Vani, K. (2016). A novel thresholding technique in the curvelet domain for improved speckle removal in SAR images. *Optik-International Journal for Light and Electron Optics*, 127(2):634–637.
- Tascikaraoglu, A. and Uzunoglu, M. (2014). A review of combined approaches for prediction of short-term wind speed and power. *Renewable and Sustainable Energy Reviews*, 34:243–254.
- Touzi, R., Lopes, A., and Bousquet, P. (1988). A statistical and geometrical edge detector for SAR images. *IEEE Transactions on geoscience and remote sensing*, 26(6):764–773.
- Upadhyay, R., Padhy, P., and Kankar, P. (2015). Ocular artifact removal from EEG signals using discrete orthonormal Stockwell transform. In *India Conference (INDICON), 2015 Annual IEEE*, pages 1–5. IEEE.
- Ventosa, S., Simon, C., Schimmel, M., Dañobeitia, J. J., and M̀nuel, A. (2008). The S-transform from a wavelet point of view. *IEEE Transactions on Signal Processing*, 56(7):2771–2780.
- Wang, Y. and Orchard, J. (2009). The discrete orthonormal Stockwell transform for image restoration. In *2009 16th IEEE International Conference on Image Processing (ICIP)*, pages 2761–2764. IEEE.
- Weickert, J. (2003). Coherence-enhancing shock filters. In *Joint Pattern Recognition Symposium*, pages 1–8. Springer.

- Yu, C., Li, Y., and Zhang, M. (2017a). Comparative study on three new hybrid models using Elman Neural Network and Empirical Mode Decomposition based technologies improved by Singular Spectrum Analysis for hour-ahead wind speed forecasting. *Energy Conversion and Management*, 147:75–85.
- Yu, C., Li, Y., and Zhang, M. (2017b). An improved wavelet transform using singular spectrum analysis for wind speed forecasting based on elman neural network. *Energy Conversion and Management*, 148:895–904.
- Zhang, Y., Zhao, Y., Kong, C., and Chen, B. (2020a). A new prediction method based on VMD-PRBF-ARMA-E model considering wind speed characteristic. *Energy Conversion and Management*, 203:112254.
- Zhang, Y., Zhao, Y., Pan, G., and Zhang, J. (2020b). Wind speed interval prediction based on Lorenz disturbance distribution. *IEEE Transactions on Sustainable Energy*, 11(2):807–816.
- Zhong, H., Zhang, J., and Liu, G. (2013). Robust polarimetric SAR despeckling based on nonlocal means and distributed lee filter. *IEEE Transactions on Geoscience and Remote Sensing*, 52(7):4198–4210.
- Zidelmal, Z., Hamil, H., Moukadem, A., Amirou, A., and Ould-Abdeslam, D. (2017). S-transform based on compact support kernel. *Digital Signal Processing*, 62:137–149.
- Zikov, T., Bibian, S., Dumont, G. A., Huzmezan, M., and Ries, C. R. (2002). A wavelet based de-noising technique for ocular artifact correction of the electroencephalogram. In *Proceedings of the Second Joint 24th Annual Conference and the Annual Fall Meeting of the Biomedical Engineering Society*[[Engineering in Medicine and Biology, volume 1, pages 98–105. IEEE.

PUBLICATIONS

Journal publication:

1. Kamath, P. R., Senapati, K. (2021). "Short-term wind speed forecasting using S-transform with compactly supported kernel." *Wind Energy*, 24(3), 260-274. (SCIE)
2. Kamath, Priya R., Kedarnath Senapati, and P. Jidesh. (2020) "Despeckling of Sar Images Using Shrinkage of Two-Dimensional Discrete Orthonormal S-Transform." *International Journal of Image and Graphics* 21(02), 2150023. (Scopus)

International Conferences:

1. Senapati, K., & Kamath, P. R. (2019). Time–Frequency–Phase Analysis for Automatic Detection of Ocular Artifact in EEG Signal using S-Transform. In *Machine Intelligence and Signal Analysis*. (IIT-Indore), 49–58, Springer, Singapore.

BIODATA

Name : Priya R. Kamath
Email : priyarkamath@gmail.com
Date of Birth : 26th February 1987.
Permanent address : Priya R. Kamath,
405, Preethi Towers,
Urwa Market,
Mangalore,-575 006.

Educational Qualifications :

Degree	Year	Institution / University
B.E. Telecommunication Engineering	2008	BNMIT VTU
M.Tech. Computer Science & Engineering	2012	MIT, Manipal Manipal University.